MINISTRY OF EDUCATION AND TRAINING

QUY NHON UNIVERSITY

TRUONG DUY HUONG

SYNTHESIS OF MS_2 (M = Mo, W) AND THEIR MODIFICATION WITH g-C_3N_4 AS PHOTOCATALYSTS

MAJOR: PHYSICAL AND THEORETICAL CHEMISTRY

CODE No.: 9440119

DOCTORAL THESIS IN CHEMISTRY

BINH DINH - 2021

MINISTRY OF EDUCATION AND TRAINING

QUY NHON UNIVERSITY

TRUONG DUY HUONG

SYNTHESIS OF MS_2 (M = Mo, W) AND THEIR MODIFICATION WITH g-C_3N_4 AS PHOTOCATALYSTS

MAJOR: PHYSICAL AND THEORETICAL CHEMISTRY

CODE NO.: 9440119

Reviewer 1: **Dr. Nguyen Van Thang**

Reviewer 2: **Assoc. Prof. Nguyen Duc Cuong**

Reviewer 3: **Assoc. Prof. Tran Thi Van Thi**

Supervisor:

Assoc.Prof. VO VIEN – Quy Nhon University

BINH DINH – 2021

DECLARATION

This thesis has been completed at the Quy Nhon University, in cooperation with KU Leuven, under the supervisor of Assoc.Prof. Vo Vien. I hereby assure that this research project is mine. All the results are honest, have been approved by co-authors and have not been released by anyone else before.

Supervisor	Author
Assoc.Prof. **VO VIEN**	**TRUONG DUY HUONG**

ACKNOWLEDGEMENTS

Firstly, from my heart, I would like to express my gratitude to both of my promoters, Prof. Vo Vien and Prof. M. Enis Leblebici not only for your enthusiastic guidance, expertise and invaluable time, but also for your encouragement when I encountered difficulties during the time of doing the research. Furthermore, from the beginning to the very end of my study time in KU Leuven, Belgium, I could say that without the constant support from Prof. M. Enis Leblebici my study would haven't accomplished any progress as I have today. Meanwhile, the belief that I have ability to do the research from Prof. Vo Vien made me more energetic to overcome the tough time on my scientific pathway.

Another professor who inspired me a lot and that also the one always is in my heart, Prof. Tom Van Gerven. You always gave me a warm welcome and a lovely smile that made me feel more confident and relax when we had unforgetable group meetings together along with Prof. M. Enis Leblebici. I am not exaggerated when say that the meeting time with both of you has been the most beautiful moments that I have experienced in my life. Even in the time of writing this acknowledgement, I still feel that happy time in my mind. So, it is not easy to express that feeling in words, especially in English, I just try to say how kind of you are.

Having the opportunity to study in Belgium, a heart of Europe how can I forget the financial support from TEAM project, VLIR-UOS. Without this project, without the effort from all the project maker members, including Prof. Do Ngoc My (Rector of QNU), Prof. Nguyen Tien Trung, Prof. Vu Thi Ngan, Prof. Vo Vien, especially from Prof. Minh Tho Nguyen, my dream could not come true.

I also would like to thank my friends who stood with me in any circumstances. Those from Vietnam like Mis. Vu Thi Lien Huong, rector of Le Khiet High School for the Gifted, Mr. Le Van Trung chemistry group leader of the school and all lovely colleagues. To Pham Hoang Quan, one of my closest friends who taught me some basic experimental skills from the beginning, the fact that you suddenly passed away made me could not believe, I promise to take care of your little daughter as much as I can within my ability, Mr. Tran Duc Trung for your help in heating my samples at Dung Quat Technology and Engineering and encouraging me in time when I had troubles, my students Quoc Nhat and Quang Tan for your effort to do the experiments in the school laboratory in the early days for the first Vsef that we achieved the best prize, the second group with Tuan Anh and Nguyen Khang, the third group with Vu Quan and Anh Kiet, Mr. Dinh Trong Nghia and Le Van Phuong for your time in coffee shops whenever I need someone to talk and those who I worked and met in KU Leuven such as Lief in the Admission Office, Alena in the Secretary Office, Christine for your instructions in the lab and characterizing my samples, Michelle for your ordering chemicals, Ruijun for some wonderful parties, watching a football match of OH Leuven and XPS analysis, Thomas and Glen for your support in the lab, Mohammed for your nice conversation, Joris in MTM for your acceptance and instruction of using inert atmosphere furnace, the CIT football team which gave me a chance to be a goalkeeper for the first season and a defender for the second, Tri who being with me all the time from Camelo Tores to Home Vesalius, the two nice family of Mr. Thanh Hai & Mis. Mien Trung, Hung & Hang with a lot of support from the early days, Tan Hung (little Hung) for your unforgettable Martini wine party and Hung, Linh, Tuyet Anh, brother Giang for the last but beautiful visit. My lovely group, Mis. Lan, Thanh Tam, To Nu, Zoan An, Huu Ha, all of you are also still in my mind today and future.

Last but not least, I would like to give all of my loving heart to my wife and two daughters Ha Khanh and Cao Nguyen, who always give me an unlimited energy source and the strongest motivation to overcome the difficulties during the time of studying. To my beloved wife, you know, your sacrifice and hard working to take care our angels during the time I was away from home is the most valuable thing that I have ever had, that reminded me of the responsibility not only to our little family but also to myself to keep my spirit on track without giving up regardless the inevitable obstacles. To my father, you have always been beside me on my way in spite of the fact that you have let us alone on this planet for six years, I miss you so much. Mama, how can I show how much important you are to me when now you are become unique for my life, you don't have direct contribution to my work, but the way you have overcome the big loss made me feel that you have been hiding your broken heart to help me to focus more on my work. I also would like to give my sincere gratitude to my mother- and father-in-law for your uncountable support in terms of finance and emotion. My siblings Thuy, Tai, Mis. Tram and my brother-in-law Binh, all of you also in my mind for your sentimental value that you gave me.

CONTENTS

DECLARATION

ACKNOWLEDGEMENTS

CONTENTS

LIST OF TABLES

LIST OF FIGURES

APPENDIXES

LIST OF ABBREVIATIONS AND SYMBOLS

1. Abbreviations

AOPs	:	Advanced oxidation processes
BET	:	Brunauer – Emmett – Teller
BQ	:	p-Benzoquinone
CB	:	Conduction band
COD	:	Chemical oxygen demand
CVD	:	Chemical vapour deposition
DMSO	:	Dimethyl sulfoxide
DRS	:	Diffuse reflectance spectroscopy
EDX	:	Energy-dispersive X-ray spectroscopy
FTIR	:	Fourier transform infrared
IR	:	Infrared
LC-MS	:	Liquid chromatography – Mass spectrometry
LED	:	Light-emitting diode
LP	:	Standardized lamp power
MB	:	Methylene blue
MCN	:	$MoS_2/g\text{-}C_3N_4$
PL	:	Photoluminesence
PSTY	:	Photochemical space-time yield
pzc	:	Point of zero charge
RhB	:	Rhodamine B
SEM	:	Scanning electron microscopy
STY	:	Space-time yield
TBA	:	Tert-butyl alcohol

TEM : Transmission electron microscopy

TEOA : Triethanolamine

TGA : Thermalgravimetric analysis

UV : Ultraviolet

WCN : WS_2/g-C_3N_4

VB : Valence band

XPS : X-ray photoelectron spectroscopy

XRD : X-ray diffraction

2. Symbols

C : Concentration

D : Inner diameter

E_g : Bandgap

h : Planck constant

k : Rate constant

m : Mass

P : Power

Q : Flow rate

q : Adsorption capacity

R_e : Reynold number

r : reaction rate

S : Surface area

t : Time

V : Volume

ρ : Density of flowing fluid

π : Pi number

μ : Dynamic viscosity

v : Frequency

θ : Fraction of reactant absorbed

LIST OF TABLES

LIST OF FIGURES

INTRODUCTION

1. Problem statement

Along with the development of many areas of industries the arising of environmental pollution has become more and more serious. A lot of hazardous chemicals have been released into water and air, resulting in severe consequences for human health, such as dyes from textile industry, antibiotics from aquaculture, pesticides and herbicides from agriculture, etc., that urgently requires effective methods to solve the problem. Heterogeneous photocatalyst, which is one of advanced oxidation processes, has attracted attention of many scientists due to its ability to treat wastewater containing organic pollutants just using light with suitable wavelength and air oxygen as oxidant source. One of the most photocatalysts that has been used widely is TiO_2 owing to its low-cost, chemical stability and nontoxicity. However, the big drawback of this catalyst comes from its UV light absorption. In order to be a prospective method in wastewater treatment, the catalyst should be able to be active in the visible light which makes up approximate 8 times higher than that of UV light in the whole sunlight spectrum. To find a solution for this, a variety of techniques can be applied, including modifying TiO_2 and the other oxide photocatalysts by doping with metal and non-metal elements, decorating with photosentitizers, etc., to make them become activated in the visible range of light. Another way has also been studied broadly is fabrication of photocatalysts which themselves working in the region of wavelength ranging from 400-600 nm. MoS_2 and WS_2, two members of the transition metal dichalcogenide family, possess the corresponding bandgaps of 1.3 eV and 1.35 eV, indicating that both of them can be excited by the visible light. As similar to the other photocatalysts, using separately could lead to an unavoidable phenomenon, namely high rate of recombination of photoinduced electron and hole. Thus, apart from searching an effective method of synthesis, the finding of way of slowing down the recombination rate is also an important task. From this high demand of production of such photocatalysts to meet the practical amount the following topic was chosen as my PhD thesis, "*Synthesis of MS_2 (M = Mo, W) and their modification with g-C_3N_4 as photocatalysts*"

2. Objective of the thesis

This thesis aims to find a facile method of synthesis and evaluation of MS_2 (M = Mo, W) and the composites MS_2/g-C_3N_4 as visible-light-driven photocatalysts and building a system that can transfer them from lab scale into practical application.

3. Scope of the thesis

The scope of the thesis: The method used for the synthesis involving the solid state reaction and the modification of MS_2 (M = Mo, W) carried out by combining them with g-C_3N_4. The evaluation of photocatalytic activity mainly based on the degradation of dyes, including rhodamine B and methylen blue, the photodecomposition of an antibiotic enrofloxacin also explored using the better catalyst. The building of photocatalytic pilot for using the prepared materials just focused on a simple method of recovering the used catalyst involving the natural sedimentation and automating the system.

4. Significanes

This thesis not only has significance in science, but also in practical is as follows:

Scientific significance: Building synthesis processes of both MS_2 (M = Mo, W) and the composite $MS_2/g\text{-}C_3N_4$ using solid state reaction, the investigating the photocatalytic activity the obtained materials indicated the importance of adsorption in the whole photocatalysis process, the more the amount of organic pollutant adsorbs onto the photocatalyst, the larger the efficiency of photodegradation of that target molecule the catalyst exhibits. Nevertheless, the so high adsorption could lead to a negative effect on the whole process. Apart from low power, the monochromatic light emitted from light emitted diode could result in a high photochemical space-time yield compared to the others such as incandescent and xenon lamps.

Practical significance: Simplifying the photocatalyst synthesis process of the visible-light driven materials, this resulted in a large amount of the catalysts that meets the real requirements. Designing the pilot, which can be a flexible and practical approach, in other word, that design could be a part of a complete wastewater treatment system or used separately and the light could be changed from an artificial source of low power to sunlight depending on the situation.

5. Thesis contributions

This thesis provides 04 main contributions as follows:

Successful synthesis of both MS_2 (M = Mo, W) and the composite $MS_2/g\text{-}C_3N_4$ from sodium molybdate dihydrate and tungstic acid as molybdenum and tungsten sources, respectively and thiourea as a source of sulfur. The prepared processes were not only facile but also resulted in a large amount of the materials that would meet the demand of using photocatalyst in practical application.

The adsorption-photocatalysis relation to the whole photocatalytic process was clarified through the study of pH effect on the photocatalytic activity of the prepared materials. This might be meaningful for the choosing of suitable photocatalyst for a particular target to reach the highest efficiency.

Light emitted diode (LED) became the best option lamp compared to the others in terms of the efficiency of using electricity, a crucial element in real application using a new benchmark, namely photochemical space-time yield (PSTY).

A simple design for a photocatalytic pilot that meets the basic requirements of using photocatalyst for water treatment polluted by organic substances such as maximizing the contact between the catalyst and the wastewater, continuously mixing with air to ensure the dissolved oxygen enough for the photodegradation, using LED of low power, etc. Furthermore, in order to be practically feasible the designed pilot can be operated automatically and easily connected to the complete system in which the pilot is just one of the modules.

6. Thesis structure

This PhD thesis contains: Introduction (05 pages), three chapters, including Chapter 1 – Literature review (22 pages), Chapter 2 – Experimental section (19 pages), Chapter 3 – Results and Discussions (47 pages), Conclusion (02 pages), References (19 pages) and List of Publications (01 page).

The numbers of Tables and Figures in this thesis are 05, 66 respectively. Involving the thesis, there have been 218 references were cited and 04 publications, in which 02 belong to ISI journals, namely Bulletin of the Korean

Chemical Society and Chemical Engineering and Technology and 02 from QNU Journal of Science.

Chapter 1. LITERATURE REVIEW

1.1. OVERVIEW OF CURRENT PHOTOCATALYSTS

The first photocatalyst studied in 1972 by Fujishima and Honda [59] is TiO_2 acting as an anode for water splitting in a photochemical cell . Four years later, in 1977, it was first used by Frank and Bard for the reduction of CN^- in water widening its application to photodegradation of pollutants in the environment [55]. So far, TiO_2 has become the most widely investigated photocatalyst due to its unique photocatalytic efficiency, photo-stability, low cost, nontoxicity, availability, thermal and chemical stability. Besides TiO_2 and the other photocatalyst ZnO have exhibited their advanced photocatalytic activity for wastewater treatment as well [99]. However, they all possess the same disadvantage that they do not work under the visible light because of their large band gap, *e.g.* anatase TiO_2 has the band gap of 3.2 eV, which significantly prevent them from using solar energy for activation. This is due to the fact that in the solar spectrum ultraviolet light accounts for only 4-5%, meanwhile the visible light makes up to nearly 40% of the solar energy [132]. To dealt with this vital deficiency many modifications have been employed to make them become active in the visible light region with good efficiency such as doping [39], [52], [99], [127], [169], dye sensitization [9], [108], [110], [199] heterogeneous coupling [86], [100], [185], [191], [199], *etc*. In addition to that, a lot of effort has been made to develop the novel materials which themselves active under the visible light without any modification. The materials which fall into this category have been widely investigated include Bi_2WO_6 [40], $BiVO_4$ [49], $Bi_{24}O_{31}Br_{10}$ [146], Ag_3PO_4 [80], $CaIn_2O_4$ [45], g-C_3N_4 [196], *etc*. However, in order to improve the photocatalytic performance they have been usually combined with other components, for instance, $BiVO_4$/rGO [155], $ZnSnO_3$/rGO [64], Ag_3PO_4/g-C_3N_4 [73], Ag/AgBr/g-C_3N_4 [26],

$Ag/AgVO_3/rGO$ [213]. Doping has also been a technique for enhancing the photocatalytic activity, such as O-g-C_3N_4 [56], Bi-Ag_3PO_4 [209], Co-$BiVO_4$ [217], Mo-$BiVO_4$ [30], B-Bi_2WO_6 [58]. Among these visible-light-driven photocatalysts, transition-metal-dichalcogenides-based such as MoS_2-based and WS_2-based have attracted attention of many scientists due to their appropriate bandgap for visible-light harvesting and the other unique properties as you will see in the next section, leading to a variety of applications such as hydrogen production, pollution reduction, and photosynthesis [74], [111], [119], [142].

1.2. MS_2-BASED (M = Mo, W) PHOTOCATALYSTS

1.2.1. Structures of MS_2 (M = Mo, W)

MoS_2 and WS_2 are materials that belong to a family of transition metal chalcogenides (TMDs) with layered structure in which each unit (MS_2) comprises a transition metal (M = Mo, W) layer sandwiched between two sulfur atomic layers with MoS_2 structure representative showing in Figure 1.1.

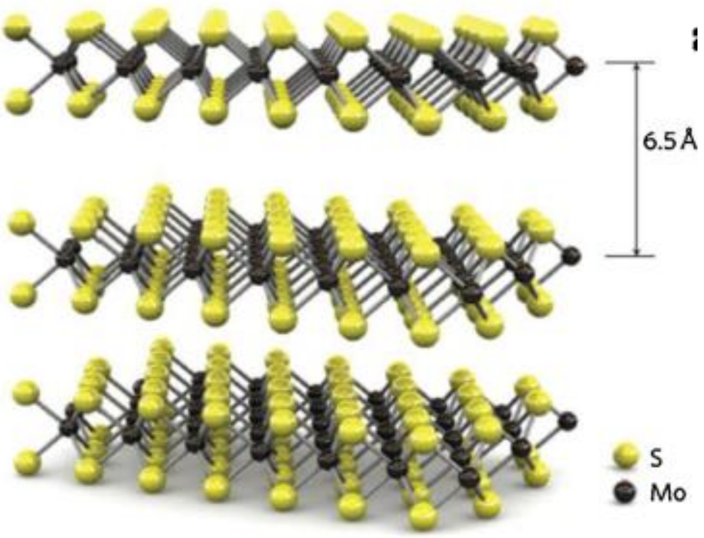

Figure 1.1. MoS_2 structure in three dimensions with the distance between the two adjacent layers of 6.5 Å [138].

There are three types of structures of TMDs depending on the arrangement of the atoms, namely, hexagonal (H), tetragonal (T) and their distorted phase (T') [34]. Taking MoS_2 as a representative of the two materials, it has four following polytypes 1H, 1T 2H and 3R as with the drawings shown in Figure 1.2.

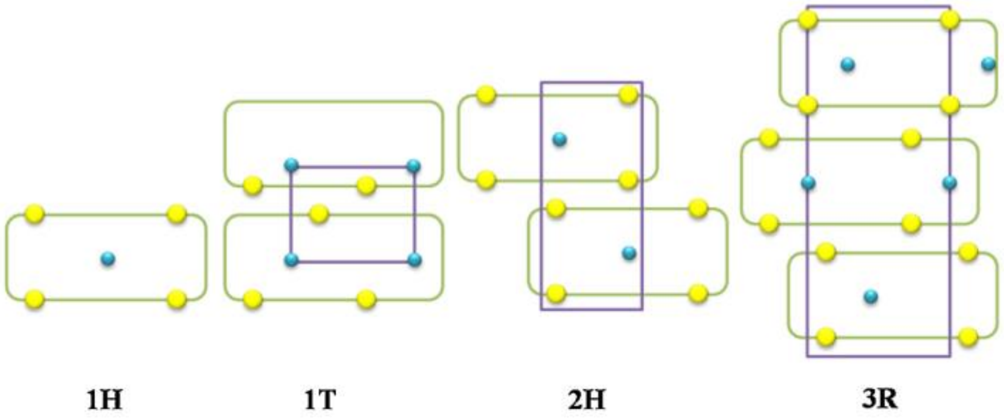

Figure 1.2. Four common MoS_2 poly-types [12].

More specifically, in the 1H phase, the basic unit of MoS_2 monolayer, the sulfur atoms are organized into two layers creating a sandwich structure having a layer of molybdenum atoms in the middle, and the S atoms in the upper layer are located directly above those on the lower layers. Meanwhile, for 1T-MoS_2 the Mo atoms locate at the center positions of the octahedral interstices of the S layers and the S atoms in the upper and lower planes are offset from each other to form a unit cell [74]. The next polytype of MoS_2 is 2H with two MoS_2 units in the unit cell. Each layer has the structure of 1H with a monatomic Mo plane between two monatomic S planes in a manner that described above. Two layers, which weakly coupled by van der Waals interaction, in the unit cell are arranged so that Mo atoms of one layer are located on top of S atoms in two adjacent layers [10]. The 3R MoS_2 also has the same trigonal prismatic coordination as the 2H MoS_2, however, there are three MoS_2 units per unit cell. Of four polytypes, 1H is the most stable, it is also the stable phase of 2D MoS_2

[198]. In bulk MoS_2, both 1T and 2H exist with the latter phase is usually more stable, having different properties, 1T is a metal, meanwhile, 2H is a semiconductor [189]. As bulk form MoS_2 (2H) is an indirect bandgap semiconductor with a bandgap value of 1.3 eV, when reducing the sample thickness down to a few atomic layers or even to a 2H monolayer the bandgap is widened to 2.1 eV [61], however, still as an indirect form. As mentioned above, a 2H monolayer is composed of two layers of 1H linked together just by weak interaction of van der Waals force, this allows that monolayer could be further divided, leading to a three atomic layer sheet [11]. The transformation also converts the for a single 1H layer from indirect to direct bandgap with the calculated value increasing to 2.3 eV [38]. Similarly, the bandgap of WS_2 has the value of 1.35 eV for bulk material as indirect [93] and approximate 2.0 eV for monolayer as direct one [206]. This optical property suggests that such materials can strongly absorb in the visible region of the solar spectrum, and it is more appropriate when using as a cocatalyst.

1.2.2. MS_2-based composites

Similar to the other photocatalysts such as TiO_2, MS_2 (M = Mo, W) has been widely used in the form of composites to improve the photocatalytic activities of the individual components, especially in the field of photocatalytic degradation of organic contaminants. The composites in which MS_2 (M = Mo, W) used as a cocatalyst have been recently developed such as MoS_2/graphene oxide [47], [95], [104], [215], [220]; MoS_2/g-C_3N_4 [103], [114], [125], [133]; MoS_2/TiO_2 [79], [162], [210]; MoS_2/BiOBr [43], [151], [192]; WS_2/WO_3 [44], WS_2/TiO_2 [190], WS_2/BiOBr [57]. Among various partners that MS_2 (M = Mo, W) combine with, g-C_3N_4 has been considered as a promising candidate due to its electronic structure with band gap of 2.7 eV, in addition to low-cost, abundance of source, non-toxicity and chemical stability [83], [112], [207]. The combination of MoS_2 and g-C_3N_4 to create a composite is favourable due to the two facts, firstly, both of them are layered materials could result in intimate contacts facilitating for the charge transfer between the two phases, and another comes from the proper band edges of the two components [178] to produce type II of semiconductor heterojunctions [181]. Regarding the proper band edges, g-C_3N_4 has the conduction band (CB) and valence band (VB) edges at -1.13 eV and +1.57 eV, respectively, meanwhile, the corresponding values of MoS_2 as nanosheets are -0.1 and + 2.0 eV [61]. This difference in band edges allows the electrons transfer from the CB of g-C_3N_4 to that of MoS_2 and the holes transfer from the VB of MoS_2 to that of g-C_3N_4. As a result, in the formed composite MoS_2/g-C_3N_4 both electrons and holes are more mobile compared to the individual components. This leads to the reduction in recombination rate of photoinduced charge carriers, therefore increase the photocatalytic activity.

1.2.3. Synthesis methods

1.2.3.1. MS_2 (M = Mo, W) synthesis

In order to obtain MS_2 as mono or few layers the following two strategies, namely, "top-down" exfoliation and "bottom-up" synthesis method have been widely used [211]. The two representatives for the former strategy are mechanical exfoliation, exfoliation method, meanwhile, hydrothermal method, solvothermal method and chemical vapor deposition representing for the latter one [189]. Like graphene sheets synthesis, MoS_2 single-layer can be exfoliated from SiO_2/Si with Scotch-tape method [101]. Regarding the exfoliation method, that could be chemical exfoliation [65], liquid-phase exfoliation [69] and electrochemical exfoliation [115]. Lithium ion intercalation is the most common chemical method for fabrication of 1T metallic MoS_2 using n-butyllithium in hexane reacting with MoS_2 powder under argon atmosphere, at 65°C overnight to form Li_xMoS_2. After removal of unreacted n-butyllithium and its organic residue, the embedded MoS_2 was dispersed in deionized water, then, centrifuged to get the stable MoS_2 nanosheets [65]. Sonication, a liquid-phase exfoliation is also an effective method for preparation of MoS_2 nanosheets [37]. The exfoliation method can be used to fabricate WS_2 nanosheets as well. Among the mentioned methods, hydrothermal method is the most common regarding economical aspect. In this method, an amount of sulfur source, commonly used such as thiourea and thioacetamide, and a molybdenum salt, such as Na_2MoO_4, $(NH_4)_6Mo_7O_{24}$ are mixed together in deionized water, then the resultant solution was heated in an oven at 200°C for 24h after being transferred to a Teflon-lined stainless steel autoclave [36], [218]. If an organic solvent is used instead of water, the other conditions keep the same then the method called solvothermal method. Some widely used organic solvent for this task include N-N-dimethylformamide, 1-methyl-2-pyrrolidinone and polyethylene glycol-600. In order to create a high-quality atomic thin MoS_2, chemical vapor deposition (CVD) has been broadly employed. For example, MoS_2 could be synthesized by sulfurization of MoO_3 using this method [102]. WS_2 nanosheets were also synthesized using those methods applied for MoS_2 as mentioned above, such as mechanical exfoliation [131], [135], chemical exfoliation [35], [113], liquid-phase exfoliation [214], hydrothermal method [21], [46] and CVD method [168], [200].

1.2.3.2. MS_2/g-C_3N_4 synthesis

In contrast to the synthesis of MoS_2 as discussed in the previous section, the synthesis of the MoS_2/g-C_3N_4 composite has been reported in just only a few studies [107], [150], [167]. Generally, the reported methods consist of three steps in which, the two individual materials g-C_3N_4 and MoS_2 are produced separately, by heating precursors such as urea, melamine, cyanamide for the former, and a hydrothermal method for the latter. Then, the mixture of g-C_3N_4 and MoS_2 is treated by ultrasound. However, both of the hydrothermal and ultrasound steps require high energy and the former occurs at hydrothermal conditions. Similarly, few reports on WS_2/g-C_3N_4 as photocatalysts have been published [4], [78]. For example, WS_2/mpg-C_3N_4 catalysts were prepared using $(NH_4)_2WS_4$ as WS_2 precursor in the presence of mpg-C_3N_4 under the atmosphere of the gas mixture of H_2S and H_2 [78]. In another study, g-C_3N_4/WS_2 samples were prepared by heating mixture thiourea and WO_3 at 550 ^oC under CS_2 gas [4]. Therefore, a facile method to synthesize a large amount of the materials without compromising photocatalytic activity is still in need.

1.3. PHOTOCATALYTIC PROCESS, LIGHT SOURCES AND ASSESSMENT BENCHMARKS

1.3.1. Photocatalytic degradation mechanism

In general, the system of heterogeneous photocatalysis using semiconductor material to absorb the suitable light to produce charge carriers, then these species will take part in the redox reactions occurring on the surface of the material but the semiconductor is still unchanged after the process. This kind of material is called a photocatalyst. The suitable light as mentioned above is the electromagnetic irradiation which has photon energy, $h\nu$, equal to or greater than the band gap (E_g) of the employed photocatalyst. The excitation of an electron (e^-) from the valence band (VB) to the conduction band (CB) will happen once the light absorbed, leaving behind a photogenerated hole (h^+) at the VB as illustrated in Figure 1.3.

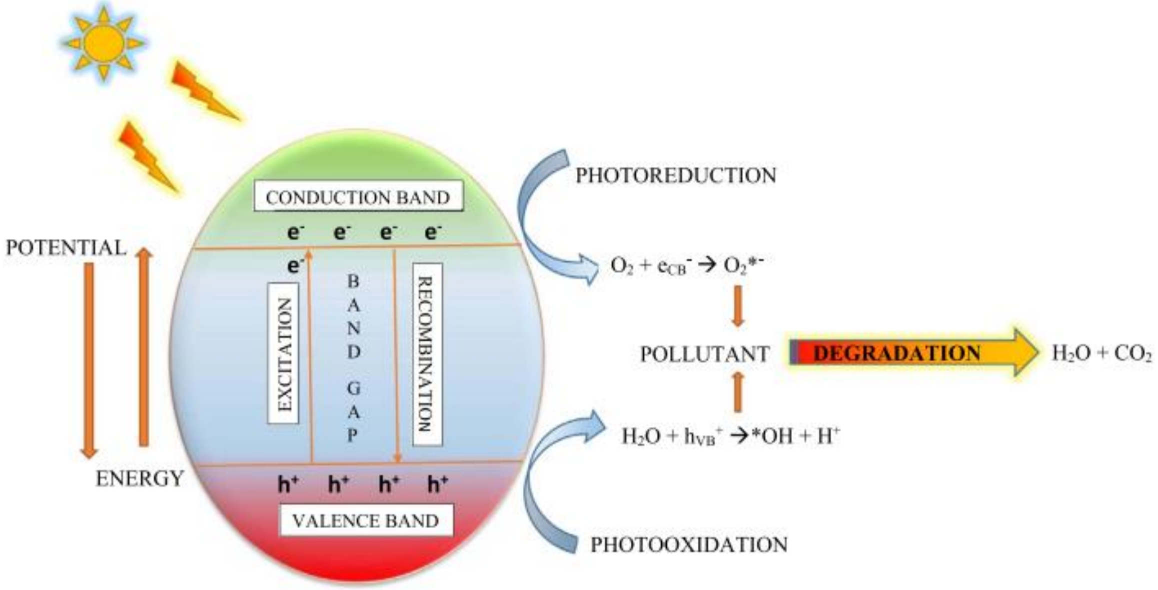

Figure 1.3. Photocatalysis principle [17]

These photoinduced electron and hole can recombine and give off the absorbed energy as heat form (Equation 1.2) or migrate to the surface of the catalyst to react with the available molecules in the system such as oxygen and water to form reactive radicals including $HO^{\cdot}$ and $O_2^{\cdot-}$ (Equations 1.3 and 1.4), respectively. Subsequently, these powerful species along with hole could completely photodegrade the organic pollutants presenting in the system to simple molecules such as carbon dioxide and water through a number of intermediate species (Eq.1.5). These reactions were broadly proposed as follows [17]:

$$\text{Photocatalyst} + h\nu \rightarrow h^+ + e^- \qquad (1.1)$$

$$h^+ + e^- \rightarrow \text{energy (heat)} \qquad (1.2)$$

$$h^+ + H_2O \rightarrow HO^{\cdot} + H^+ \qquad (1.3)$$

$$O_2 + e^- \rightarrow O_2^{\cdot-} \qquad (1.4)$$

$$\text{pollutant} + (h^+, HO^{\cdot}, O_2^{\cdot-}) \rightarrow \text{intermediates} \rightarrow CO_2 + H_2O \qquad (1.5)$$

The recombination phenomenon of e^- and h^+ occurs just within picoseconds after photogeneration if there is no scavenger in the system [17]. However, even in the presence of scavengers, the recombination of the photoinduced charges is not completely avoidable due to its high rate. This leads to the dissipation of energy and therefore reducing the quantum efficiency [32]. The causes for this phenomenon could be ascribed to imperfections in the crystal and it may happen both on the surface and in the bulk of the semiconductor. Thus, the techniques that use in prolonging the lifetime of the photogenerated electron and hole play a crucial role in improving the photocatalytic activity of the photocatalyst. The normal methods which have been applied for this purpose are doping, co-catalyst addition, heterogeneous coupling, *etc*. This will be discussed more detail in the below sub-sections of this chapter.

1.3.2. Reaction kinetics

In the photocatalytic process for photodegradation of organic contaminant, a series of five consecutive steps includes the transportation of reactant from bulk of the solution to adsorb onto surface of the catalyst, then the interfacial photoreaction and finally the desorption of the product to the bulk from the surface. This five-step process is illustrated by a flowchart as shown below.

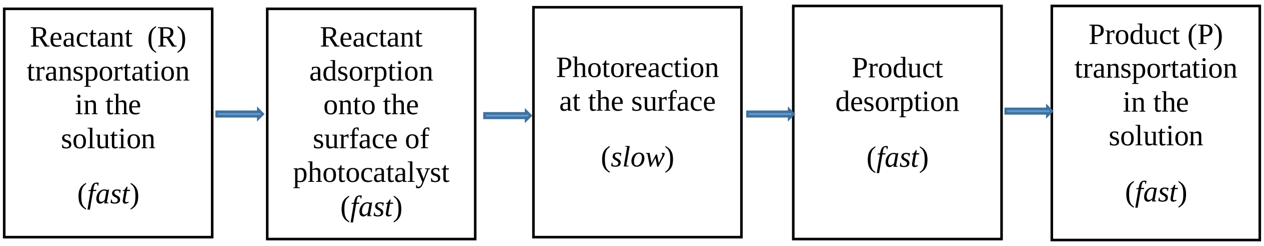

Figure 1.4. Five-step flowchart of heterogeneous photocatalysis [17].

For consecutive reactions as shown in Figure 1.4, the overall photocatalytic reaction rate is controlled by the slowest stage. This rate determining step in the photocatalysis process would be the photoreaction taking place on the catalyst's surface if the reactor is under continuously stirred condition, then the rate of the reaction (r) converting (R) into (P) can be defined as,

$$r = -\mathrm{d}C/\mathrm{dt} = k.\theta \qquad (1.6)$$

where θ is the fraction of reactant absorbed, k is the reaction rate and if the adsorption process obeys the Langmuir model then this quantity can be found as follows,

$$\theta = KC/(1+KC) \qquad (1.7)$$

where C is the concentration of reactant at adsorption-desorption equilibrium, and K is the adsorption coefficient of the reactant. From Eq.(1.6) and (1.7), the reaction rate becomes,

$$r = -dC/dt = kKC/(1+KC) \qquad (1.8)$$

Equation 1.8 expresses the kinetics of photocatalytic degradation of organic compounds which follows the Langmuir-Hinshelwood model [60]. In the case of low concentration of reactant, $C << 1$ the rate can be simplified to that of the apparent first-order reaction with rate constant $k_{apparent} = kK$:

$$r = -dC/dt = kKC \qquad (1.9)$$

or

$$\ln(C_o/C_t) = kKt = k_{apparent}.t \qquad (1.10)$$

where C_o, C_t are the concentrations of reactant before illumination and after an illumination time t. It is worth to note that these concentrations are also at equilibrium of adsorption and desorption due to the assumption that both of these processes are fast steps.

1.3.3. Adsorption role in photocatalytic process

In the previous section, adsorption of the organic target onto the photocatalyst is a step in the photocatalytic process. The importance of this step in the whole process has been reported in some researches [28], [117], [118], [126], [149]. In which the work of Y. Luo *et al.* indicated that the photodegradation rate of Reactive Red 120 on the surface of g-C_3N_4 was much faster than that in the solution [117], that means the photodegradation mainly occurs to the target molecules adsorbed on the catalyst's surface. As a result, the factors that affect the target adsorption onto the catalyst, therefore the photodegradation rate include the nature of the target, initial target concentration, solution pH and photocatalyst's surface area [94]. For a specific target onto a photocatalyst, a change of solution pH might result in a significant effect on the photodegradation rate of that molecule. This is due to the fact that pH can determine both the surface charge of the photocatalyst and the target molecule's charge, thus they can attract or repel each other, leading to an increase or decrease the extent of adsorption of that molecule onto the surface. The surface charge of the catalyst will be negative or positive depending on the solution pH is greater or smaller than the material's point of zero charge (pH_{pzc}), respectively. Meanwhile, if the target molecule contains any functional group that can be protonated or deprotonated, the ionization of that molecule will occur to form ion when changing the solution pH. For instance, methylene blue a cationic dye having no such a functional group would be photodegraded better in solution with a high pH at which the used catalyst having negative charge on the surface, such as at pH 11 over CeO_2 [136], pH 10 over Ag-TiO_2 [144], pH 8 over Ta-ZnO [92]. In contrast, an anionic dye such as reactive red 120 has the tendency of being degraded in a solution of low pH enough to make the employed material surface become positive such as at pH 7 over Pd-TiO_2-SO_4^{2-}

[172], pH 5 over AgBr/TiO_2 [173], pH 5 over TiO_2 [33]. Actually, a high pH solution can produce more hydroxyl radical for the photodegradation therefore making a contribution to the process. However, even the photodegradation caused by hydroxyl radical, this also happens on the photocatalyst surface. As a result, the adsorption of the target molecule onto the surface always plays an important role in the photocatalytic process, especially cases that the photodegradation is responsible for the direct oxidation by hole or reduction by electron from the conduction band or valence band, respectively [33]. Due to this importance, a study of this factor should be taken into account during the investigation of photocatalytic activity of a photocatalyst.

1.3.4. Light sources for photocatalysis – Light emitting diodes (LEDs)

In the photocatalytic process, the choice of light source is also one of the important aspects in the experimental setup. The light sources which have been widely applied in the photocatalysis such as Xe lamp as simulated solar light [24], [156], [182], mercury arc lamp as UV light [160], [163], [175], UV-LED [27], [29], [85], visible LED [159], [179], [180]. Both the first two lamps are relatively high energy consumption due to the high applied voltages, and a large amount of consumed energy releases as heat [84], [202]. In addition, the conventional ultraviolet light sources have other drawbacks such as containing hazardous mercury, having a relatively short lifespan, and being difficult to operate [3], [165]. Meanwhile, LEDs have shown its advantages, including the compact, lower cost, and environmentally friendly light source. Besides this, the LED light output is directly proportional to the current within its active region along with their small size and relatively longer life span (more than 50,000 h) compared to conventional ultraviolet sources [84]. An LED is a semiconductor device which can emit light of different wavelength from infrared, visible to ultraviolet depending on the composition and type of semiconductors. As a result, the using of both ultraviolet and visible LEDs of various powers for photocatalytic removal of organic pollutants has been increased significantly. For example, using 120 mW UV-LEDs with a peak wavelength of 395 nm to decompose o-cresol over TiO_2 [29], 12 W high intensity visible LED (436 nm) to degrade 4-chlorophenol over coumarin dye sensitized TiO_2 photocatalyst [63], this study also indicated that the photodegradation using LED is more suitable than Hg lamp under the same conditions. The other LEDs as flexible 2-meter strip (30 pcs/m, 7.5 W/m) which emit light of longer wavelength such as white, blue (465 nm), green (523 nm), and yellow (589 nm) also used for photocatalytic degradation of bisphenol A over carbon and nitrogen codoped TiO_2 [179]. Apart from these applications, the photodegradation of dyes using both ultraviolet and visible LEDs as irradiation sources over various photocatalysts has been studied, for instance, methylene blue over P-25 Degussa [164], rhodamine B over TiO_2 [130], *etc*.

The advantages of using LED over the others types of lamps make it become a promise light source for photocatalytic process, especially regarding the aspect of energy efficiency of the light source and low-heat that produced during the operation.

1.3.5. Photocatalytic reactor assessment

In order to compare the efficiency of different photocatalytic reactor designs the following two quantities have been widely applied in the literature. Apparent first-order reaction rate constant, *k*, which usually is expressed in min^{-1}, as mentioned in the previous sub-section, is the first one. This is a useful benchmark for comparing different reactors in terms of conversion rate. However, the reaction rate is dependent on the three following factors, including volume, light intensity and catalyst loading. The second quantity is quantum yield (ε), which can be defined as the percentage of photons which causes charge carriers to become active and expressed as,

$$\varepsilon = z\frac{RV_r}{\left(\Phi_{in} - \Phi_{out}\right)A}100 \tag{1.11}$$

where z is the amount of electrons transferred per molecule to be degraded, R (mol.L^{-1}.s^{-1}) is the reaction rate, A (m^2) is the illuminated area, V_r (L) is the reactor volume and Φ (mol.m^{-2}.s^{-1}) is the photon flux.

The quantum yield, ε, shows the efficiency of using light of the reaction system. Nevertheless, none of the mentioned benchmarks gives information on the electrical consumption of the reactor. This could lead to the case that the two reactors might have the same value of ε and/or the same reaction rate; however, the used lamp powers may be not similar [97].

A new, simple and useful benchmark has been developed by Leblebici *et al.*, is photochemical space time yield (*PSTY*) [98], with the expression is as follows:

$$PSTY = \frac{STY}{LP} \tag{1.12}$$

where *STY* (day^{-1}) is space time yield and *LP* is the standardized lamp power (kW). The *STY* is direct proportional the reaction rate constant with a particular expression depending on the type of used reactor. Meanwhile, *LP* term relates to not only lamp power, but also reaction medium volume. As an example, for a batch reactor, the *PSTY* can be calculated by the following expression:

$$PSTY = k.V/999.P \tag{1.13}$$

where k is the reaction rate constant (day^{-1}), P is the lamp power (kW) and V is the used volume of treating solution (m^3).

The Equation 1.13 indicates that this benchmark is more general than *k* itself because it not only contains the rate constant, but also includes both *V* and *P*, thus it gives a representative of the whole reaction system rather than only the reaction occurred in that system. The presence of lamp power makes the benchmark more practical in terms of expenditure of the electricity consumed. It is worth to notice that the PSTY benchmark does not include one of factors that also affect the reaction rate of the photodegradation of organic pollutant over photocatalyst, namely catalyst loading. This is excluded from the benchmark due to the fact that its consumption by the reactor is very low, then the expenditure for that is negligible compared to the cost of electricity.

1.4. PHOTODEGRADATION OF ANTIBIOTICS AND DYES IN AQUEOUS SOLUTION

1.4.1. Antibiotics photodegradation

The presence of antibiotics in waste water even at low concentrations could cause many adverse effects on human health and aquatic life, however, they have not been removed effectively by conventional treatment methods. Therefore, more effective methods like ozonation, Fenton/photo-Fenton and semiconductor photocatalysis have been employed widely [76]. Among the mentioned methods, using photocatalysts has been proven as a promise one, especially the heterojunction photocatalysts rather than the individual ones [88]. The two antibiotics, which belong to the class of fluoroquinolone antibiotics causing particular environmental relevance due to their extensive use in both human and veterinary medicine are enrofloxacin and ciprofloxacin [51]. Nevertheless, both of these antibiotics are not readily biodegradable [5], [143], thus a requirement of a treatment method is necessary. The photodegradation of ciprofloxacin has been reported over some heterogeneous photocatalysts such as $BiVO_4/Bi_2WO_6$ [158], ZnO/SnS_2 [121], $Bi_2O_3/(BiO)_2CO_3$ [31]. Meanwhile, enrofloxacin also can be photodecomposed by this type of photocatalyst, for example, Fe_3O_4/TiO_2-GO [205], Ag_2O/CeO_2 [188]. As a representative, enrofloxacin was chosen in this thesis with the molecular structure and its corresponding UV-Vis spectrum is shown in Figure 1.5.

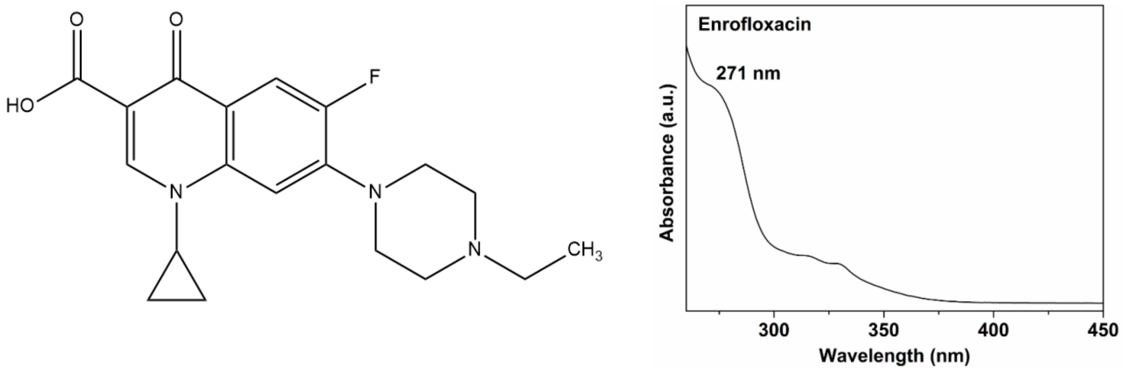

Figure 1.5. Molecular structure of enrofloxacin (left) and its UV-Vis spectrum (right).

1.4.2. Dyes photodegradation

Dyes are the substances used for creating or changing colour in many industrial areas such as textile, printing, paper, rubber, paint, plastic, etc. The discharging of a portion of these dyes leads to the streams and waterways become contaminated, dyes are thus one of the prominent pollutants in the environment [153]. Due to the complex structure the synthetic dyes, conventional methods, including precipitation, adsorption, aerobic, and biological treatment cannot be used as effective ones. Therefore, a stronger and also green method is still in need to solve the problem, heterostructure photocatalyst is one of such methods. The dyes could be classified into two categories, namely anionic and cationic dyes. The first type is also known as acid dyes because the negative charge comes from the deprotonated forms of acidic functional groups such as –COOH, phenol, -SO_3H. The second type of dyes or basic dyes contain cationic functional groups like $–NH_3^+$ or $=NR_2^+$, this type of dyes is highly stable, therefore it is quite difficult to decompose them from effluent. Rhodamine B (RhB) and methylene blue (MB) are the typical cationic dyes which are pollutants produced from textile, plastic and dye industries [72]. Their structures and the corresponding UV-Vis spectra are shown in Figure 1.6.

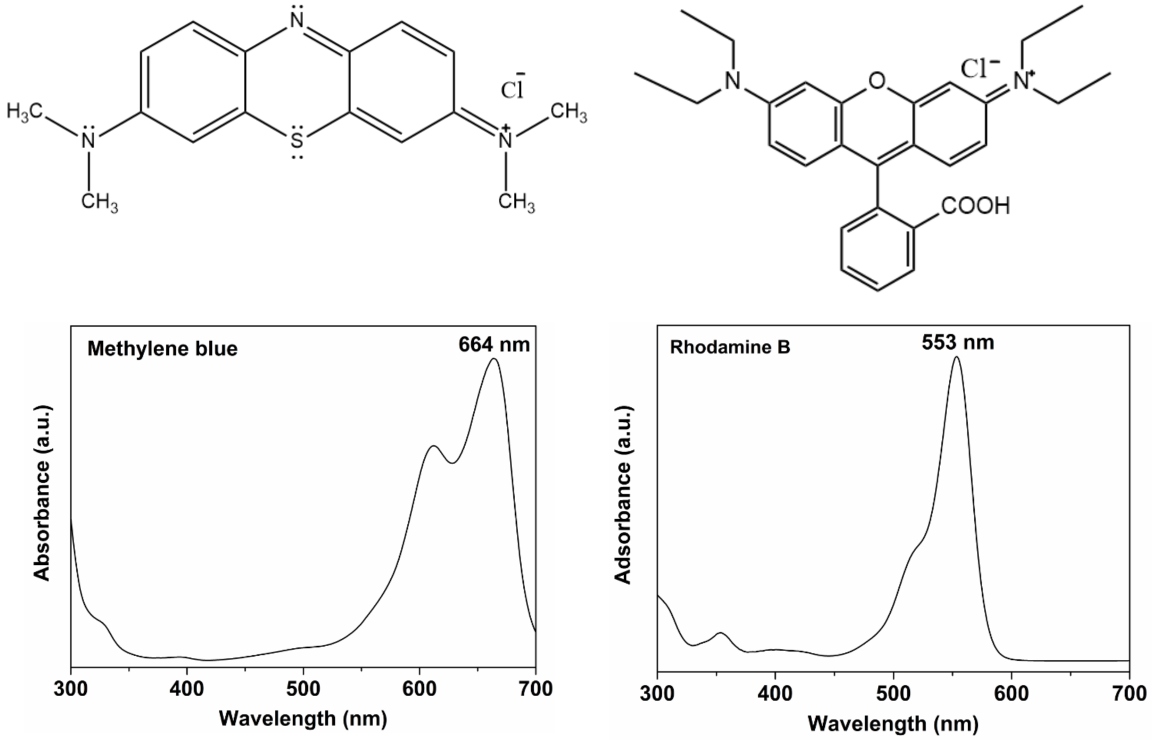

(a) (b)

Figure 1.6. Methylene blue (a) and rhodamine B (b) structures and their corresponding UV-Vis spectra

As seen in Figure 1.6, the two cationic dyes differ from each other the form they could exist in aqueous solution with different pHs. The MB molecule only adopts a cationic form, meanwhile, the RhB can form both cationic and zwitterionic species depending on pH solution. The corresponding maximum absorption wavelengths of MB and RhB are 664 nm, 553 nm observed from their UV-Vis spectra (recorded by LAMDA 365 UV/Vis Spectrophotometer) as shown in Figure 1.6 as well. The photodegradation of RhB to the different extents has been reported by many researchers over photocatalysts such as ZnO/Ag_2CrO_4 [134], $Bi_2O_2CO_3/BiOCl$ [116], $BiVO_4/InVO_4$ [66]. The first two heterojunction materials entirely decomposed the RhB dye, meanwhile the last one degraded 98% of the dye. The heterogeneous photocatalysts also used to degrade the MB dye including MoS_2/ZnO [89], NiO/SnO_2 [6] with the degradations of 97% and 99%, respectively. These results suggest that the heterojunction photocatalysts are highly appropriate to use as an effective method to treat wastewater polluted by the stable cationic dyes like RhB and MB.

1.5. PHOTOCATALYTIC PILOT DESIGN OVERVIEW

The effectiveness of utilizing photocatalysts for waste water treatment has been demonstrated through the complete degradation of a wide range of toxic organic pollutants. However, the treatment has just been successful at a laboratory scale, meanwhile at a pilot scale some of the technical problems still need to solve to meet the practical application requirements. These major factors that have to be considered to design an effective photocatalytic pilot are the illumination of the catalyst in terms of both scientific and economic aspects, the reuse of photocatalyst, and the operation of the system [140]. Normally, there are two types of reactor regarding the catalyst installation, including slurry reactor in which the catalyst is uniformly dispersed in the solution and another type, in contrast, is the immobilization of the catalyst [98]. Each of them has its own disadvantages, while the separation of the catalyst is a barrier for the employment of the former installation, the latter faces the difficulty of how to immobilize the catalyst without decreasing its photocatalytic activity due to an unavoidable drop in the surface area contacting to the contaminated water and mass transfer problem. If the separable step could be improved, the slurry reactor would be a better choice, especially in the case of using a photocatalyst that differs from TiO_2. Although the photocatalytic system at pilot scale for photodegradation of organic contaminants has been widely studied around the world, however, to our knowledge this field of research in Vietnam is still limited. Therefore, the building of a photocatalytic pilot using visible-light-driven photocatalyst with a simple structure, but automatic controlled could provide one more option for the treatment of wastewater besides the conventional methods as mentioned above.

1.5.1. Slurry reactors versus immobilized catalyst reactors

Photocatalytic reactors can be classified into two types, called slurry reactors and immobilized reactors based on the way of catalyst distributing in the system as dispersion particles and fixing on a particular surface, respectively [96]. In the former type of reactors the mass transfer limitations are minimized due to the even distribution throughout the system of high surface area catalyst. The geometry of the slurry reactors has been designed to focus on how to utilize the light for illumination as efficient as possible or dealing with the photon transfer limitations. This based on the fact that there is a threshold irradiance for a specific photocatalyst, that means when reaching the threshold an increase in irradiance leads to a decrease in overall photonic efficiency and the observed linear relationship between light intensity and reaction rate only occurs in the range of irradiance having values lower than that of threshold point. According to the Carp reports, the threshold irradiance for TiO_2 is 25 $mW.cm^{-2}$ [23]. Some typical reactors belong to this category are multi-lamp reactor [18], rotating annular reactor [157], fountain reactor [105]. However, a high barrier that prevents those slurry reactors from practical applications is the difficult catalyst recovery step coming from the nanosize of catalyst particles. This tough issue can be solved by immobilizing the catalyst on a surface, thus creating another type of reactor as mentioned above the immobilized catalyst reactors which make photocatalysis becomes more industrialized integrated. This catalyst coating also results in an increase in mass and photon transfer limitations due to the transport of the pollutant to the catalyst surface being governed by diffusion. Therefore, maximizing the illuminated surface has been the main objective in designing this type of reactors. Some of the typical immobilized catalyst reactors are parallel plate reactor [174], microreactor [176], optical fibre reactor [42], foam reactor [50], spinning disc reactor [201].

1.5.2. Photocatalyst separation

A serious problem that arises from using photocatalyst for photodegradation of organic pollutants is how to separate the employed photocatalyst from slurry reactor. This separation step can be removed if the catalyst in the system is immobilized.

1.5.2.1. Catalyst immobilization

Practically, the immobilization of photocatalyst, usually TiO_2 has been carried out on a support which satisfies several criteria [145] such as strong adherence between catalyst and support, unchanging the catalyst reactivity during the combining process, possessing a highly specific area and adsorbing pollutants easily. The widely used supports that meet the mentioned requirements, including glass [16], [62], activated carbon [48], [122], silica gel [145], [152], *etc*. The common glass is used as a substrate is borosilicate due to its highly transparent property and high calcination temperature [145]. One of the common methods for coating TiO_2 on the glass support is dip coating [54], with an example described as follows. Firstly, glass was carefully cleaned by sonication in acetone. Then, it was immersed in a solution of titanium tetraisopropoxide in dry i-PrOH. Finally, the sheet was removed from the solution at a constant rate of 20.32 cm/min to obtain the sample after the drying process. A wide range of other techniques have been developed such as modified thermal treatment [19], sol-gel [8], electrochemical anodisation and spray coating [20], *etc*. The development of immobilization techniques along with the immobilized catalyst reactors as presented in the previous section that makes photocatalysts become more practical. It is obvious that this type of reactor brings us the benefit from the fact that the catalyst is not to be separated for the next cycle, however, it can make other problems including the lower efficiency compared to those using suspended particles [71] and the situation become even worse if the wastewater containing iron which could deposit onto the catalyst resulting in the catalyst fouling, therefore, decrease the treatment efficiency [129].

1.5.2.2. Catalyst separation

There have been various methods to recover the photocatalysts which used as suspended particles in slurry reactors such as microfiltration [109], [186], ultrasound [161], foam flotation [148], coagulation [87], hydrocyclone [15], and sedimentation [128]. Among the mentioned ways of catalyst separation the sedimentation is simple method due to its operational simplicity. This method is based on the fact that at the point of zero charge (pH_{pzc}) the dispersed particles tend to be aggregated, then the sedimentation process could be faster [53]. In order to achieve the pH_{pzc} of the used material the change of suspension pH can be applied. Take TiO_2 as an example, at pH 7 which is close to its pH_{pzc} the sedimentation rate was much improved compared to the other pHs [53]. Another way of making the settlement of catalyst faster is creating a higher specific gravity material as in study of MS Nahar *et al.* by doping TiO_2 with iron, the obtained sample Fe-doped TiO_2 with higher content of iron exhibited a higher rate of catalyst sedimentation [128]. This simple way of recovery of photocatalyst could also be useful for practical application of this type of material in the wastewater treatment process if we can build a pilot that can be operated automatically.

Chapter 2. EXPERIMENTAL SECTION

2.1. CHEMICALS AND EQUIPMENTS

The chemicals used in this thesis are listed in Table 2.1. All chemicals were used without further purification.

Table 2.1. Main features of the used chemicals

Name	Formula	Purity	Supplier
Tungstic acid	H_2WO_4	98%	Merck
Sodium molybdate dihydrate	$Na_2MoO_4.2H_2O$	99.5%	Sigma-Aldrich
Thiourea	CN_2H_4S	99%	Sigma-Aldrich
Rhodamine B	$C_{28}H_{31}ClN_2O_3$	95%	Sigma-Aldrich
Methylene blue	$C_{16}H_{18}N_3SCl.3H_2O$	98.5%	Sigma-Aldrich
Enrofloxacin	$C_{19}H_{22}FN_3O_3$	98%	Sigma-Aldrich
Triethanolamine	$C_6H_{15}NO_3$	99+%	Acros Organics
Tert-butyl alcohol	$C_4H_{10}O$	99.5%	Merck
p-Benzoquinone	$C_6H_4O_2$	98%	Sigma-Aldrich
Dimethylsulfoxide	C_2H_6OS	99.9%	Sigma-Aldrich
Hydro peroxide	H_2O_2	35%	Merck
Hydrochloric acid	HCl	0.1 M	Reagecon
Sodium hydroxide	NaOH	0.1 M	Reagecon

Distilled water was used to prepare all of the aqueous solutions in this study. The equipments that used to set up pilot are listed in Table 2.2.

Table 2.2. Equipments for pilot building

Equipment	Description	No.
Feed tank with stirrer	50 L, inox 304	1
Pump	180 W, 24 V DC	1
Autovalve	24 V,d = 21 mm	3
DC-DC converter circuit	V-A controller and display	1
Flow meter	Flow sensor, DN 15	1
Light source	Blue LED, 50 LEDs/board	2

2.2. MATERIALS FABRICATION

2.2.1. Fabrication of WS_2/g-C_3N_4

The WS_2/g-C_3N_4 composites were synthesized via a facile solid-state calcination from precursors of tungstic acid and thiourea [2]. In a typical procedure, mixtures of tungstic acid and thiourea with different weight ratios were ground well, transferred into a ceramic cup covered closely by aluminum foil, and then treated at 500^oC for 3h under inert medium in an oven. The obtained products were denoted as nWCN, in which n equals to 5, 7 and 10 corresponding to the weight ratios of tungstic acid and thiourea being 1:5, 1:7 and 1:10. For comparison, WS_2 was prepared by heating a mixture of tungstic acid and thiourea with a weight ratio of 1:10 at 650 ^oC for 3h in N_2 gas, denoted as WS_2; g-C_3N_4 was synthesized with the same procedure for nWCN except absence of tungstic acid in the reaction mixture and referred as g-C_3N_4. The images of prepared samples were attached in Appendix 1.

2.2.2. Fabrication of MoS_2/g-C_3N_4

The layered MoS_2 was synthesized by calcination of Na_2MoO_4 and thiourea [1]. Specifically, 1.0 g of sodium molybdate (VI) dihydrate and 3.0 g of thiourea were well ground in a mortar before transferring into a ceramic crucible (30 mL). This crucible was covered by its lid to prevent the loss of product from sublimation. The mixture was then heated to 550 ℃ at a heating rate of 10°C/min under N_2 gas atmosphere and then was kept at 550°C for 2 h. The composites MoS_2/g-C_3N_4 were fabricated by heating the mixture of prepared MoS_2 and thiourea with different weight ratios. Typically, m_o gram of MoS_2 was well-mixed with 24.0 g of thiourea by a shaker (IKA Vortex 3) before grinding thoroughly by pestle and mortar, then the mixture powder was transferred to four separate 30-mL ceramic crucibles and were heated as per the conditions described for synthesis of MoS_2 above (heating rate 10°C/min, 550°C under N_2 gas for 2h) to produce MoS_2/g-C_3N_4 samples denoted as MCN1, MCN2, MCN3 and MCN5 corresponding to the m_o values of 0.06, 0.12, 0.18 and 0.30.

For comparison, g-C_3N_4 was also prepared by heating thiourea in the same conditions, the final mass yield of the preparation was 15%. All the obtained samples were washed with distilled water and ethanol before being heated at 60°C for 10h. The MoS_2 contents in the MCN1, MCN2, MCN3, and MCN5 were calculated to be 1.6, 3.2, 4.8 and 8.0 w.t. %, respectively. The images of prepared samples were attached in Appendix 1.

2.3. CHARACTERIZATIONS

2.3.1. Material characterizations

For characterization of the samples, Powder X-ray diffraction (XRD) was conducted on an X-ray diffractometer (Brucker D8 Advance) using CuKα irradiation (λ = 0.1540 nm), accelerating voltage 30kV and applied current 0.01A. Transmission electron microscope (TEM) was collected using Jeol Jem 2100F and scanning electron microscope (SEM) images were recorded by JEOL JSM-600F equipped with an energy dispersion X-ray spectrum (EDS). Infrared and Raman spectra were recorded using IRAffinity-IS (Shimadzu) spectrometer and Raman spectra used T64000 Raman with a 647.1 nm laser as an excitation source and detector CCD was cooled by liquid nitrogen, respectively. The thermogravimetric-differential scanning calorimetry analysis was carried out on the SETRAM LABSYS TG system under air or argon flow with heating rate of 10 ^{o}C/min. The optical properties were examined on a Jasco V-650 Spectrophotometer (No. UV-1800) using $BaSO_4$ as reference. The surface area of samples was determined with TriStar 3000 V6.07 A. X-ray photoelectron spectroscopy (XPS) measurements were made on an Escalab 250Xi system.

2.3.2. Determining point of zero charge

The point of zero charge (pH_{pzc}) of the materials was determined by following procedure. Typically, for each of samples, four 25-mL solutions with different pHs were prepared from distilled water, 0.1 M HCl and 0.1 NaOH solution. Then, 146 mg of NaCl was added to each of them to make the same ionic strength (0.1 M) for all solutions. Next, the pHs of the obtained solutions was recorded by pH meter as initial values (pH_i). Following this, the catalyst was added (50 mg to each container) and the containers were shaken for 24h, after which the final pHs (pH_f) were measured. A plot of $\Delta pH = pH_f - pH_i$ against the initial pH was drawn, and the pH_{pzc} was the point at which the resulting curve and horizontal axis intersected.

2.3.3. Light spectra and intensity

The spectra of light from an incandescent lamp and blue light were recorded by Ocean Optics QE 65 Pro spectrophotometer. The intensity of the blue light was also measured using the same spectrophotometer. This experiment was carried out at ProCESS, Chemical Engineering and Technology, KU Leuven.

2.4. PHOTOCATALYSIS EXPERIMENTS

2.4.1. Reaction system

In order to investigate the photodegradation test on target molecules, a suitable reactor was designed to have a jacket for controlling the temperature using a thermostat bath (Julabo) of the observing solution as shown in Figure 3.1. The used blue light was emitted by 20 LEDs (Winger) from the top with the voltage and current can be changed and stabilized manually using RND 320-KA3005P DC power supply. The other light source was 100 W incandescent lamp. The solution in the reactor can be stirred magnetically using an IKA lab disk.

Figure 2.1. Photocatalytic reactor

The reactor was put in the black box as shown in Figure 2.2.

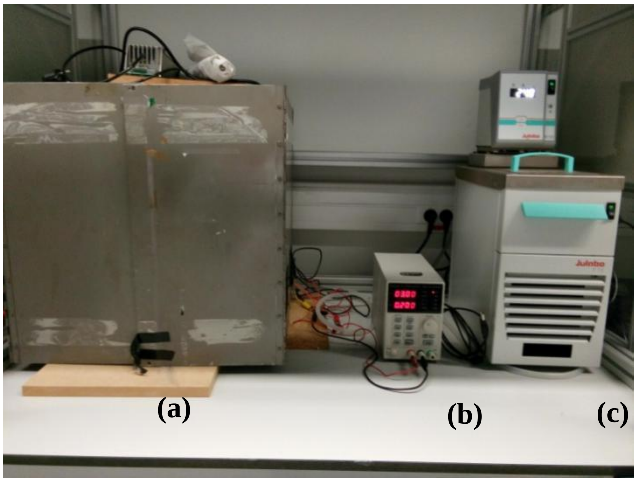

Figure 2.2. Reaction system: (a) black box, (b) DC power supply and (c) thermostat bath.

2.4.2. Photocatalytic activity evaluation

The photocatalytic activity of the prepared materials was conducted by photodegradation of methylene blue (MB), rhodamine B (RhB) and enrofloxacin (ENR) in aqueous solution. The procedures employed for the two types of photocatalysts are as follows.

For WS_2/g-C_3N_4 samples, the optimal catalyst dosage was investigated by adding an amount of catalyst into a volume of 90 mL of dye solution with the initial concentrations of 30 mg/L for both MB and RhB to achieve the catalyst concentration in the range from 0.5 g/L to 1.3 g/L, the optimum then applied for other experiments including the degradation of RhB. Before illumination, the reaction mixture was stirred continuously for certain time in dark to reach adsorption-desorption equilibrium. The reaction mixtures were then irradiated by a 100 W incandescent lamp which has the light spectrum shown in Figure 2.3 using a filter cutting off UV rays. Meanwhile, the photocatalytic activity of the as-prepared MoS_2/g-C_3N_4 samples were evaluated using RhB as a pollutant molecule. Into a 25 mL of dye solution at initial concentrations of 5.0 and 10.0 mg.L^{-1} for RhB and MB, respectively, the catalyst is dispersed at concentrations varying from 0.3 g.L^{-1} to 1.1 g.L^{-1} under stirring and the solution was kept in dark to achieve adsorption equilibrium.

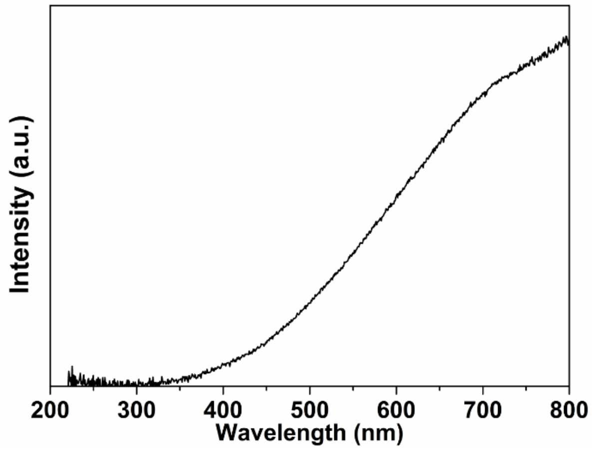

Figure 2.3. Spectrum of light emitted from the incandescent lamp

Then, the obtained optimal catalyst loading was used for other investigations. The LED blue with the emission wavelength of 450-495 nm (Figure 2.4) was used as a light source for evaluation of $MoS_2/g\text{-}C_3N_4$ photocatalytic activity, the applied voltage and current values for this LED were 3V and 0.1 A, respectively.

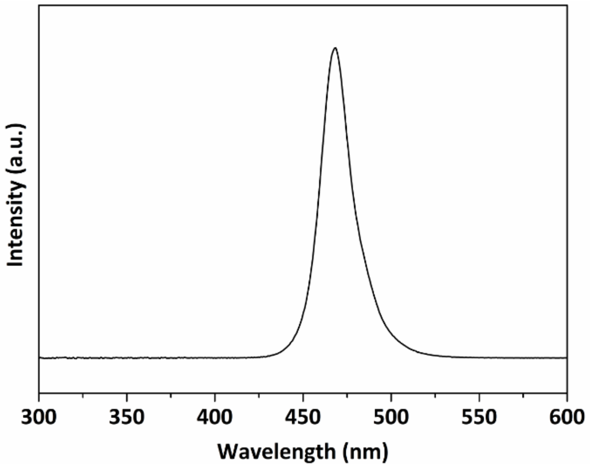

Figure 2.4. Spectrum of the blue LED light.

At a given time interval, for both kinds of catalyst, the remaining concentration of target molecules in the collected solution was determined by measuring the absorbance at their maximum wavelengths (see next sub-section) after removing the catalyst by centrifuge. In order to explore the pH effect, prior to the photocatalytic activity experiments, solution pH was adjusted by using 0.1 M HCl or 0.1 M NaOH solution.

The photodegradation of antibiotic ENR was also carried out over the best material in terms of PSTY benchmark with similar steps as described above.

2.4.3. Calibration curves

The concentration of the target molecules MB, RhB and ENR were determined by constructing the calibration curves (Figure 2.5) at their corresponding maximum absorbance wavelengths of 664 nm, 553 nm and 271 nm. The used spectrophotometer was Lambda 365, Perkin Elmer.

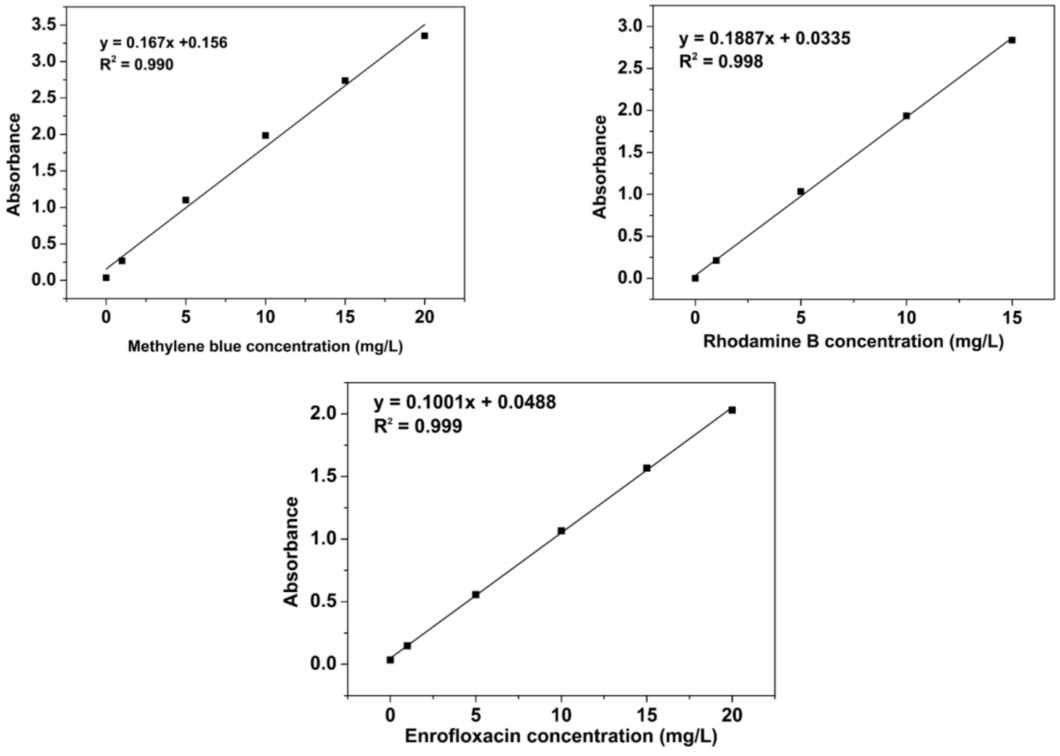

Figure 2.5. Calibration curves for quantitative determination of target molecules.

2.4.4. Measurement of emitted irradiance using spectrophotometer probe

In order to measure the irradiance which emitted from the reactor containing the different solution volume with various catalyst loading, the following procedure was applied.

Firstly, finding the relation between the height (mm) of the solution from the solution surface to the bottom corresponds to the containing solution volume (cm^3) in the cylindrical reactor by measuring the inner diameter of the reactor, which was 44.50 mm, then, the radius was 22.25 mm. Surface area of the reactor can be calculated by the formula,

$$S = \pi . r^2 \qquad (2.1)$$

Therefore S = 1555.28 mm^2, and the volume of the solution containing in the reactor could be estimated by,

$$V = Sxh = 1555.28xh\ mm^3 = 1.56xh\ cm^3 \qquad (2.2)$$

where h is the height of the solution containing in that reactor.

Secondly, the probe of the spectrophotometer was placed under the reactor containing a known solution volume, then the height of the solution was calculated using Equation 2.2, at a constant distance. Recording the irradiance and plot that quantity as a function of the calculated height of the solution in the reactor.

2.4.5. COD measurement

In order to evaluate the extent of mineralization of the target molecule, chemical oxygen demand (COD) was used. The COD expresses the amount of oxygen originating from potassium dichromate that reacts with oxidizable substances contained in 1L of water under the working conditions of the specified procedure. Results are expressed as mg/L COD (= mg/L O_2).

The spectrophotometer (HACH DR 5000) was used for the measurement and the COD value can be read directly on the screen.

2.4.6. High performance liquid chromatography (HPLC) and mass spectrometry (MS)

Determination of the photodegradation intermediates of ENR was carried out on an LC–MS system equipped with a 6460 HPLC (Agilent, USA) and an API 3000 mass analyzer. The HPLC column was a Kromasil C18 column (4.6 × 100 mm) from Angilent. 0.1% of formic acid aqueous solution and acetonitrile were used as mobile phases A and B, respectively. The effluent flow rate keeps 0.2 mL/min. An injection volume of 10 μL was used in analysis and column temperature at 302 K (30 ℃). Linear gradient elution as follows: the initial 93% A was reduced to 50% A over 25 min. Then mobile phase A returned to 93% in 30 min. A positive ionization mode electro-spray interface was used. The other parameters were set as the following: the ESI was done at 4 kV at temperature of 350 ℃; the gas (N_2) flow rate was 12 L min^{-1}, and nebulizer was 35 psi.

2.4.7. Active species determination

In order to investigate the active species for the photodegradation of RhB over MoS_2/g-C_3N_4 material, the different quenchers were used. In this work, the used trapper reagents are triethanolamine (TEOA, h^+ scavenger), t-BuOH (TBA, $^{\bullet}OH$ scavenger), p-benzoquinone (BQ, $O_2^{\bullet -}$ scavenger) and dimethylsulfoxide (DMSO, *e* scavenger), each of which had the concentration was kept 100 times higher than that of used RhB.

2.4.8. Oxidizing agent

The effect of oxidant concentration on photodegradation rate of RhB over MoS_2/g-C_3N_4 was also studied with the molar ratio H_2O_2-pollutant in the range of 50 to 400. The molarity of RhB 5 mg/L was 0.01 mM, therefore the concentrations of H_2O_2 could be determined. A 1.0 M stock solution of H_2O_2 which was prepared from H_2O_2 35%. Typically, a volume of H_2O_2 stock solution (V_{H2O2}) was added into 25.0 mL of 5 ppm RhB solution to get the calculated concentration. For comparison, the effect of hydro peroxide itself on the dye degradation was carried out as well. The details of the experiment were summarized in the Table 2.3.

Table 2.3. Added volumes of H_2O_2 0.1 M solution corresponding to the molar ratios

Molar ratio	0	50	100	200	400
V_{H2O2} (ml)	0	0.125	0.25	0.5	1.0

2.5. PILOT DESIGN

2.5.1. Pilot description and operating principles

The pilot consists of three main parts as shown in Figure 2.6 including control box (1), feed tank (2) and collector (3).

Figure 2.6. Photocatalytic pilot

The details can be illustrated in Figure 3.2.

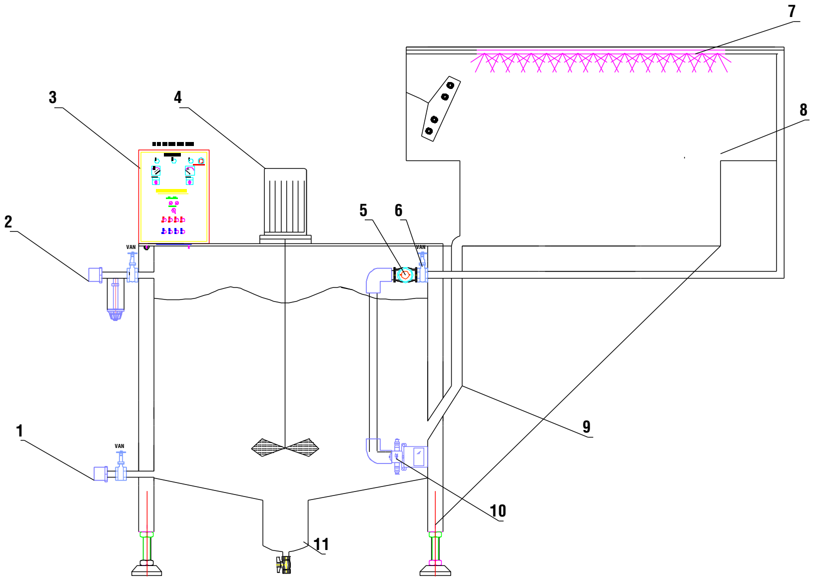

Figure 2.7. Schematic representation of the pilot:discharging valve (1), charging valve with filter (2), control box (3), stirrer (4), pumping valve (5), flow sensor (6), delivery tube (7), blue LEDs (8), recharging tube (9), pump (10) and settling column (11).

When working, the wastewater goes through the filter (2) to the feed tank where it is mixed with the catalyst by a stirrer (4), then the suspension is pumped to the delivery tube (7) to fall to the collector, in this stage the mixture is irradiated to photodegrade the organic pollutant and finally the solution with catalyst particles comes back to the feed tank via the recharging tube (9). The rate of the flow goes through the pumping valve (5) can be measured by a flow sensor (6). This process is repeated until the contaminant being treated completely. At the end of the process the stirrer, pump, lamp source will be switched off automatically, the catalyst then settles down to the settling column (11) for recovery and the draining of post-treated water taking place *via* discharging valve (1). A new treatment cycle will begin in an automatic manner through a control box (3).

2.5.2. Detailed instructions

All the activities of the pilot could be governed by the control box (Figure 2.8) using the following functional buttons:

(1) Stop button: for switching off the device in an emergency situation.

(2) Automatic button: for operating the system automatically through an Arduino circuit using timing program with four particular interval times (t_1, t_2, t_3 and t_4) to turn on/off the electric valve, stirrer, pump and lamp source, these times are determined as follows:

Time for charging the feed tank, t_1: this is the required time for filling the tank with wastewater need to be treated to a certain mark corresponding to a particular volume for one cycle of treatment.

Time for complete treatment, t_2: this is the time for the organic pollutants in a particular volume of wastewater being photodegraded completely.

Settlement time, t_3: time for sedimentation process of photocatalyst to the settling column.

Draining time, t_4: time for discharging the post-treated water under gravity.

(3) Pump

This regime allows the pilot working immediately so does it in the interval time t_2 as mentioned above until being stopped.

(4) Volt-ampere display and controller.

(5) Flow meter

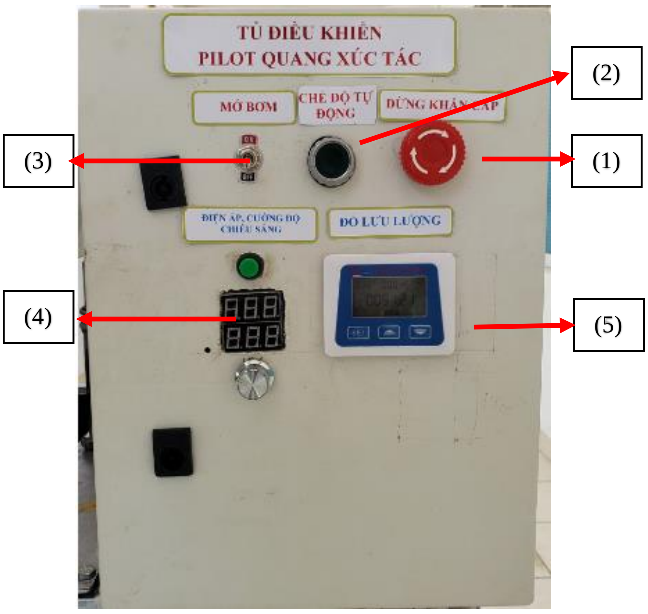

Figure 2.8. Control box

The feed tank (Figure 2.9) was designed to consist of additional parts, namely (1) stirrer, for even distribution of the catalyst particles throughout the solution; (2) pump, for delivery the wastewater from the tank to the collector; (3) settling column; (4) discharging valve.

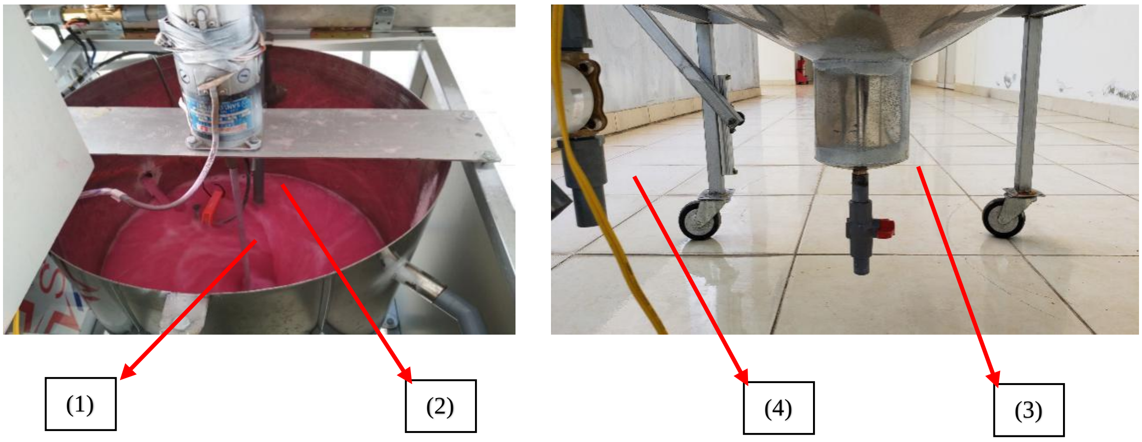

Figure 2.9. Feed tank

The treating area (Figure 2.10) has the following parts: (1) collector, (2) delivery tube, (3) lamps.

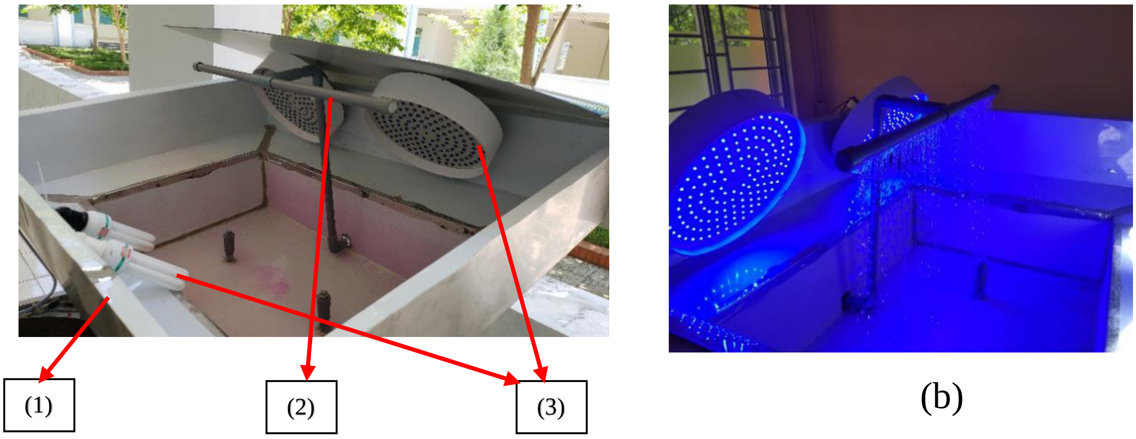

(b)

(a)

Figure 2.10. Collector: (a) not working, (b) working

2.5.3. Timing program for Arduino circuit

In principal, this pilot works as a batch reactor, however, the automatic system can allow it to operate continuously. In order to control the system for a particular case, the interval times from t_1 to t_4 as described previously for that are required. These parameters allow the Arduino circuit controlling the system, and they are coded in a program as shown in Figure 2.11. The interval times could be changed easily from this program.

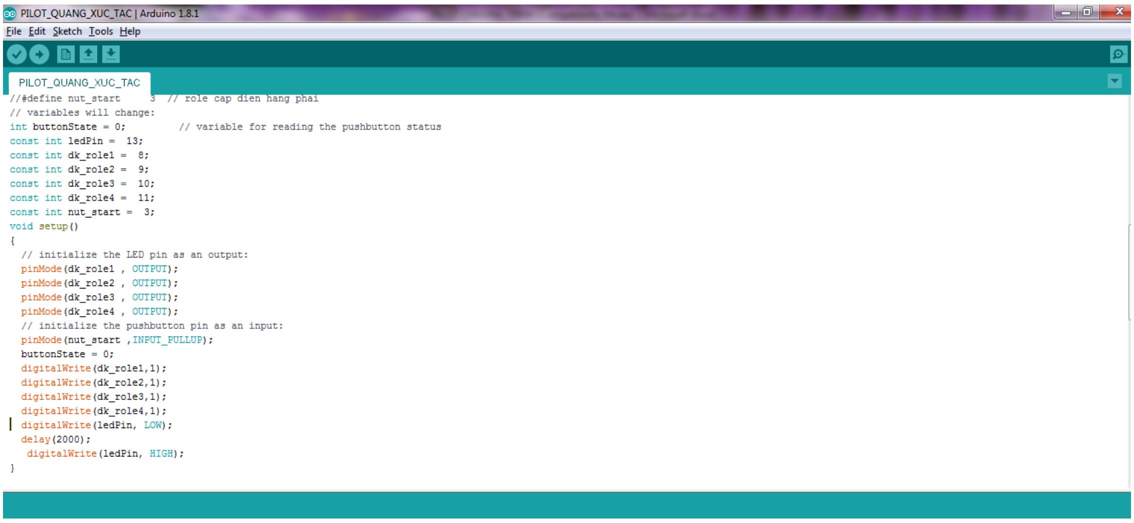

```
//#define nut_start     3  // role cap dien hang phai
// variables will change:
int buttonState = 0;         // variable for reading the pushbutton status
const int ledPin =  13;
const int dk_role1 =  8;
const int dk_role2 =  9;
const int dk_role3 =  10;
const int dk_role4 =  11;
const int nut_start =  3;
void setup()
{
  // initialize the LED pin as an output:
  pinMode(dk_role1 , OUTPUT);
  pinMode(dk_role2 , OUTPUT);
  pinMode(dk_role3 , OUTPUT);
  pinMode(dk_role4 , OUTPUT);
  // initialize the pushbutton pin as an input:
  pinMode(nut_start ,INPUT_PULLUP);
  buttonState = 0;
  digitalWrite(dk_role1,1);
  digitalWrite(dk_role2,1);
  digitalWrite(dk_role3,1);
  digitalWrite(dk_role4,1);
  digitalWrite(ledPin, LOW);
  delay(2000);
   digitalWrite(ledPin, HIGH);
}
```

Figure 2.11. Timing program

2.5.4. Sedimentation procedure and catalyst recovery percentage

The sedimentation rate was determined from the measurement of transmitted light at a wavelength of 800 nm through a cuvette containing photocatalyst suspension with the loading of 0.7 g.L^{-1}. The suspension was adjusted to the desired pH, then stirred magnetically for 60 min before the transmittance recorded.

The catalyst recovery percentage was calculated as follows, weighing an accurate mass of used catalyst to disperse into the 30 L of 5 ppm RhB solution, stirring for 60 min, keeping the system still for 1, 2, or 3 h for catalyst settlement, and finally draining the water to get the material at the bottom of the settling collumn. The solid was washed and separated from the condensed suspension through a vacuum filter, then dried at 60 ^{o}C overnight before weighing for the calculation.

2.6. CALCULATIONS

2.6.1. Reaction rate constant and photochemical space-time yield (PSTY)

At low concentration pollutants, the Langmuir-Hinshelwood model would become the pseudo-first-order one, as expressed in Equation (2.3):

$$\ln(C_o/C) = kt$$

where C is the concentration of target molecule (mg.L^{-1}), C_o is the adsorption equilibrium concentration of contaminant before irradiation (mg.L^{-1}), t is the reaction time (min or h), and k is the reaction rate constant (min^{-1} or h^{-1}). This constant is the slope of the straight line of $\ln(C_o/C)$ versus time, t. Practically, this rate constant was found by the linear fit using OriginLab. Accounting for the lamp power and the treated solution volume, a new benchmark could be used to compare the photocatalytic activity of different reactor and catalyst combinations. This benchmark measure is the photochemical space-time yield (*PSTY*), which mentioned in Chapter 1 with the Equations 1.12 and 1.13.

2.6.2. Adsorption capacity

The adsorption capacity of the materials was performed towards target molecules. Typically, *m* gram of material was dispersed in *V* litre of contaminant aqueous solution with known initial concentration, C_i (mg/L). Then, the mixture was magnetically stirred in the dark at room temperature to reach the equilibrium. The equilibrium concentration, C_e (mg/L), of the contaminant after removing the solid phase by centrifuging was measured by a UV-vis spectrophotometer at its maximum wavelength. Note that this concentration was denoted as C_o in the photocatalytic activity evaluation. The amount of target molecule adsorbed on the material or adsorption capacity (q_e, mg/g) of that material towards the contaminant was calculated by the following expression:

$$q_e = (C_i - C_e)V/m \qquad (3.3)$$

2.6.3. Flow rate for turbulent regime

In order to ensure that the flow regime in the circular pipe is turbulent, the Reynold number (R_e) must exceed 10,000. From this number and its expression which is as follows:

$$R_e = 4\rho Q/\pi\mu D \qquad (3.4)$$

where ρ (kg/m^3) is the density of flowing fluid, μ (Pa.s) is the dynamic viscosity and D (m) is the inner diameter of the pipe, and Q (m^3/s) is the flow rate.

Substituting the first three quantities in the equation (3.4) by the corresponding values of 1000 kg/m^3, 0.798.10^{-3} Pa.s, and 27.10^{-3} m results in the following expression of R_e

$$R_e = 5.9 \text{ x } 10^7 Q \qquad (3.5)$$

Therefore, the minimum flow rate that requires for the turbulent regime would be 1.7 x 10^{-4} m^3/s or 10 L/min and this rate could be displayed by the flowmeter screen.

2.6.4. Throughput for pilot plant

The treatment capacity or throughput of a pilot working as a batch reactor to a particular pollutant for a given degradation efficiency is expressed as volume treated/total treatment time/reactor area, usually in L/h/m^2. The reactor area in this study could be defined as the area of the collector being illuminated.

Chapter 3. RESULTS AND DISCUSSION

3.1. MATERIAL CHARACTERIZATIONS

3.1.1. WS_2/g-C_3N_4 characterizations

3.1.1.1. X-ray diffraction patterns

Figure 3.1 shows the XRD patterns of 5WCN, 7WCN, 10WCN composites, WS_2, and g-C_3N_4. It can be observed from this figure that a high intensity diffraction peak at 27.4^o and a weak one at 13.2^o are characteristic of (002) and (100) planes of g-C_3N_4 respectively [212], [216]. For WS_2 sample, peaks at 13.6, 33.2 and 59.0^o correspond to (002), (100) and (110) planes indexed to hexagonal phase of WS_2 (JPCDS card number 084–1398). The XRD patterns of the composites exhibit two peak systems corresponding to g-C_3N_4 and WS_2 phases. However, intensity ratios of the peaks for the two phases are different from 5WCN to 7WCN and 10WCN. The Figure 3.1 also shows the relative intensity of peak at 27.4^o corresponding to g-C_3N_4 to the one at 33.2^o for WS_2 phase increased from 5WCN to 7WCN and 10WCN, which means that the relative amount of g-C_3N_4 compared to WS_2 in the composites increased with the same order mentioned above of the composites. This can be attributed to increasing relative amount of the source for g-C_3N_4 compared to that of WS_2 in the reaction mixture, which implies that an increase of n ($n = m_{thiourea}/m_{H2WO4}$) led to an increase of the content ratio of g-C_3N_4 to WS_2. For 5WCN sample, it may contain lower g-C_3N_4 content compared to 7WCN and 10WCN because it was prepared from the lower ratio of thiourea to tungstic acid, which results in its low XRD intensity. This may be attributed to that there are no significant diffraction peaks assignable to g-C_3N_4. Besides, the decrease in intensity of the diffraction corresponding to (002) plane of WS_2 in 5WCN, 7WCN and 10WCN may come from a more intimate integration of WS_2 with g-C_3N_4 resulting in a poorly stacked structure and the formation of a few-layer WS_2 structure [25].

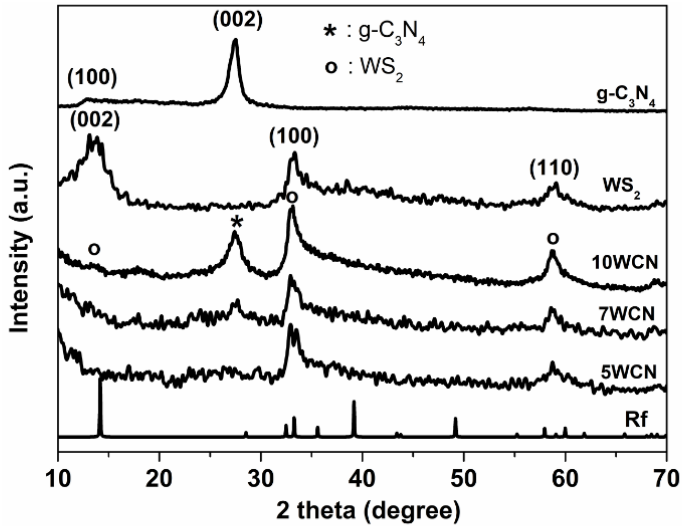

Figure 3.1. XRD patterns of 5WCN, 7WCN, 10WCN, WS_2, g-C_3N_4, and the reference for WS_2 (Rf).

3.1.1.2. Scanning electron microscopy images

Morphology of the composites and single components was characterized by SEM means and the results are shown in Figure 3.2. Figure 3.2(a) presents uniform folded nanosheets with thickness of ~20 nm for 5WCN, which may belong to WS_2. The appearance of WS_2 morphology on the surface of this material matches the above XRD results that a relative small amount of g-C_3N_4 presents in 5WCN. Figure 3.2(b), (c) and (e) show layers in flakes for 7WCN, 10WCN and g-C_3N_4, respectively. This morphology is characteristic of g-C_3N_4, which was reported elsewhere [208]. This indicates that in 7WCN and 10WCN composites, WS_2 may be covered by the layers of g-C_3N_4. For WS_2 sample, it can be seen that nanosheets of WS_2 appear again, indicating that the g-C_3N_4 was removed at the treated temperature (650 ^{o}C) for the preparation of this material.

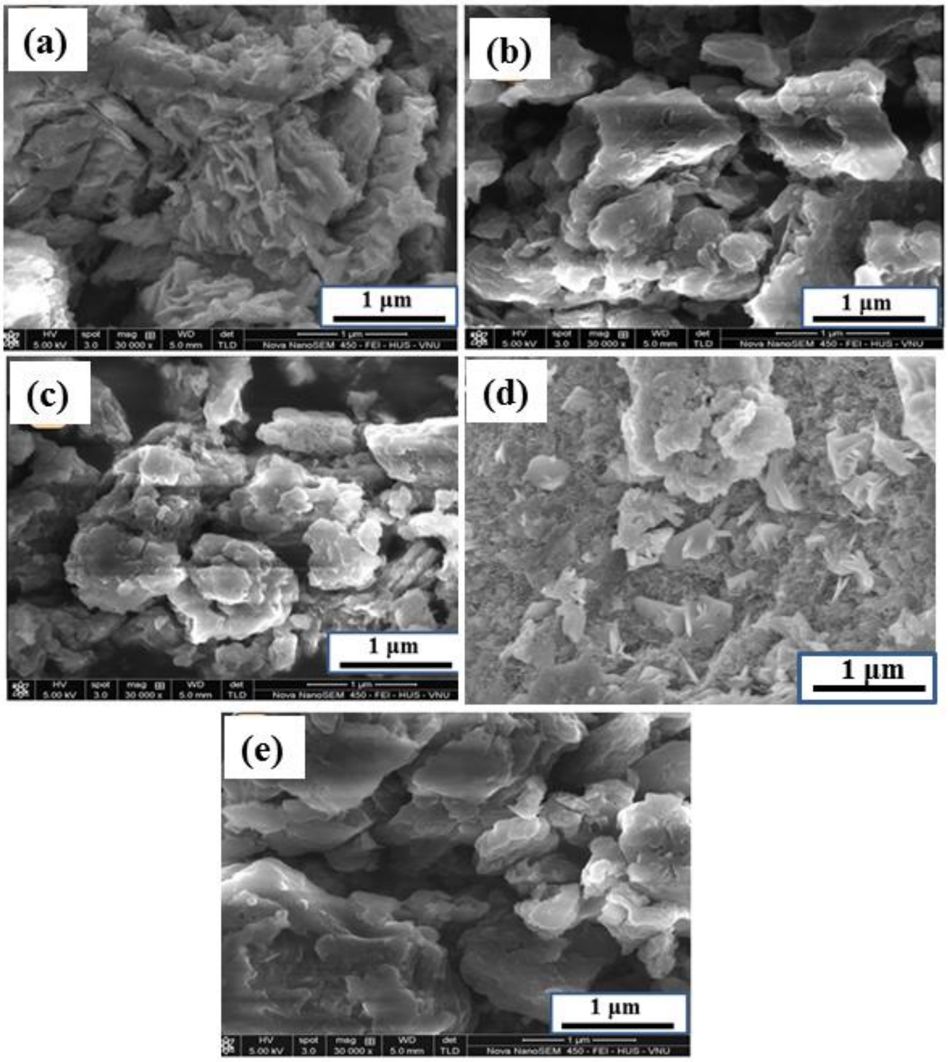

Figure 3.2. SEM images of 5WCN (a), 7WCN (b), 10WCN (c), WS_2 (d), and $g\text{-}C_3N_4$ (e).

3.1.1.3. Elemental mapping

In order to confirm the distribution and uniformity of WS_2 and $g\text{-}C_3N_4$ in the composites, EDS elemental mapping was applied for a representative material, 10WCN. Figure 3.3 shows that the presence of C, N, S and W elements in uniform distribution can be clearly observed as expected. Obviously, this also indicates that WS_2 and $g\text{-}C_3N_4$ are combined uniformly throughout the composite. The low signal from W may be attributed to the low W content compared to that of S in WS_2 compound. Moreover, the EDS quantitative analysis demonstrates the atomic ratios of C:N and W:S of 3:4.6 and 1:2.1, respectively, which are very close to the composition of the composite, $WS_2/g\text{-}C_3N_4$. This illustrates that the composite possesses heterostructures and close contact between the components, $g\text{-}C_3N_4$ and WS_2, which could facilitate the transfer of photogenerated charge carriers, therefore enhancing the charge separation and the photocatalytic activity of the composites [4].

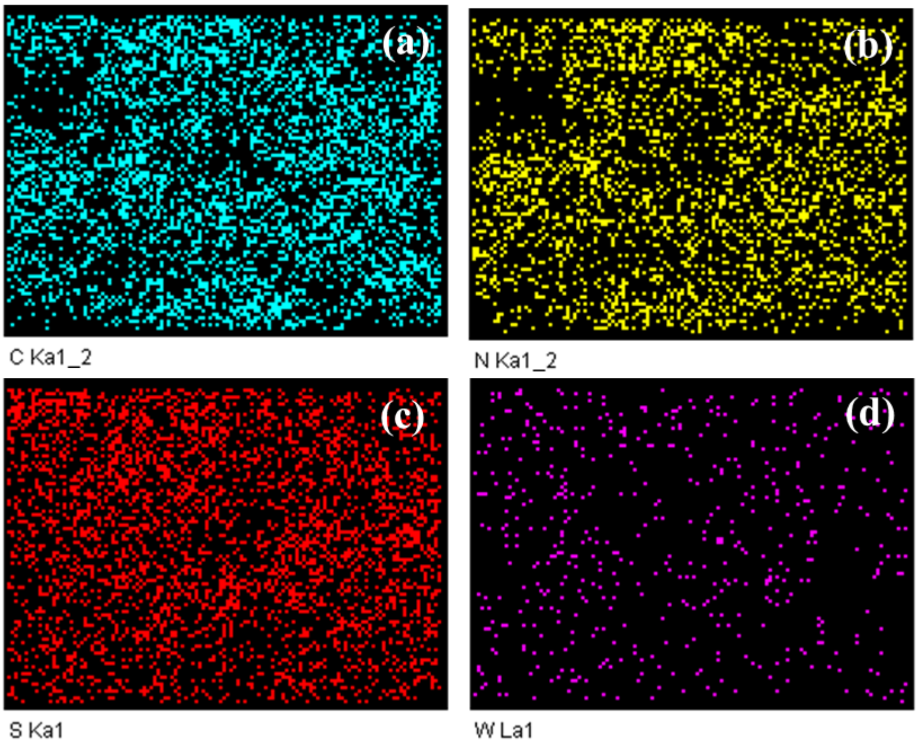

Figure 3.3. EDX elemental mapping of C (a), N (b), S (c) and W (d) elements for 10WCN.

3.1.1.4. Transmission electron microscopy images

For more information about the morphology, a representative sample, 10WCN was analyzed by TEM (Figure 3.4). For comparison, TEM image of $g\text{-}C_3N_4$ is also presented. Figure 3.4(b) indicates that morphology of $g\text{-}C_3N_4$ is in the stack of sheets. The TEM image of 10WCN (Figure 3.4(a)) shows that the formation of the closed interfaces between dark nanosheets of WS_2 coated by g-C_3N_4 with the lighter array. This further supports that the formation of heterostructure for the composite, leading to a benefit in further charge transfer between the semiconductors.

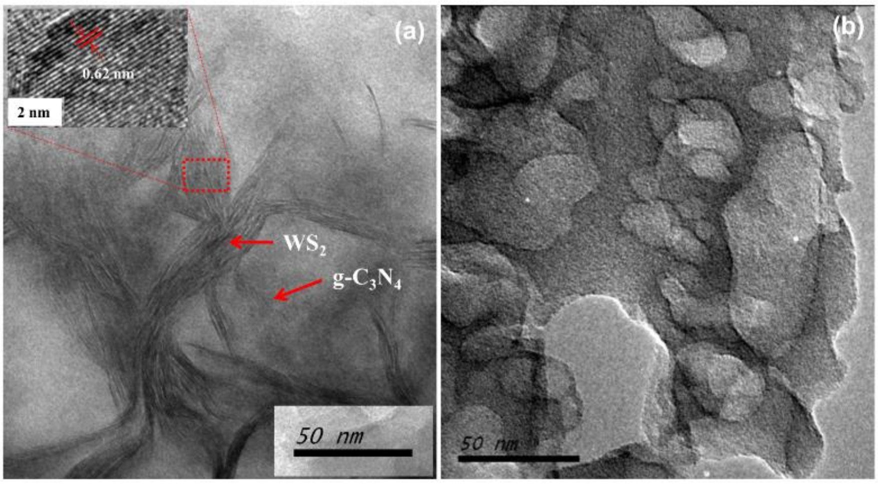

Figure 3.4. TEM images of 10WCN (a) and g-C_3N_4 (b).

3.1.1.5. Infrared spectra

Figure 3.5 and 3.6 shows the IR spectra of 5WCN, 7WCN, 10WCN, WS_2, and g-C_3N_4. It can be observed in Figure 3.5 that absorption bands at 1650-1240 cm^{-1} are attributed to the characteristic vibration of C=N and C-N bonds in heterocycles of g-C_3N_4 [4], [216]. The peak at 806 cm^{-1} may come from the vibration of the tri-s-triazine units [107], [203]. Besides, the weak peak at 884 cm^{-1} can be assigned to the N-H deformation mode [4]. These results further support that composition of g-C_3N_4 is carbon nitride with graphite-like structure. Figure 3.5 also shows the weak peak at 963 cm^{-1} which can be ascribed to the S-S vibration mode [171].

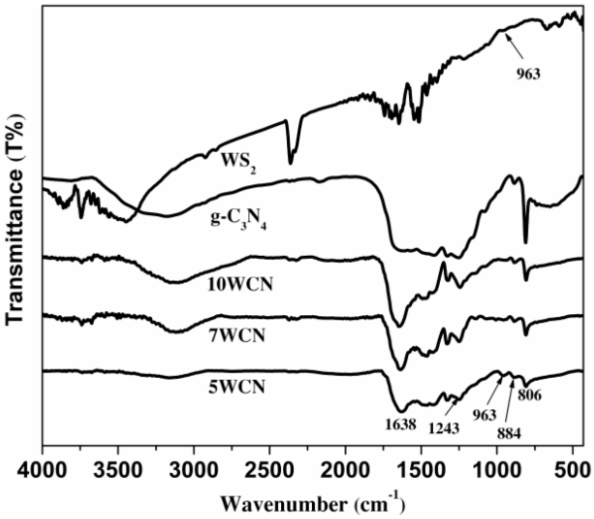

Figure 3.5. IR spectra of 5WCN, 7WCN, 10WCN, WS_2, and g-C_3N_4 in the wavenumber region of 400-4000 cm^{-1}.

Furthermore, Figure 3.6 presents the peaks at 422 and 448 cm^{-1} corresponding to the vibration mode of W-S in WS_2 [7], [171]. For 5WCN, 7WCN, 10WCN composites, Figure 3.5 show that all the spectra possess the peaks corresponding to g-C_3N_4 and WS_2. It is worth to know from Figure 3.6 that the peak at 448 cm^{-1} for WS_2 may shift to 458 cm^{-1} for 5WCN, 7WCN, 10WCN. This may be explained by existing an interaction between WS_2 and g-C_3N_4 in the composites.

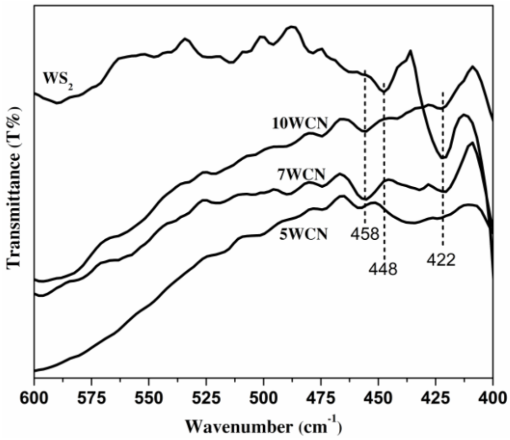

Figure 3.6. IR spectra of 5WCN, 7WCN, 10WCN, WS_2 in the wavenumber region of 400 – 600 cm^{-1}.

3.1.1.6. Raman spectrum

In order to explore more about the chemical bonds in the composites, Raman spectrum of a representative sample, 10WCN, was conducted (Figure 3.7). It is evident that there are two strong peaks at 352 cm^{-1} and 413 cm^{-1} assigned to the E^1_{2g} and A_{1g} vibration modes, which is characteristic of the layered structure of WS_2 [13], [166], [206]. In addition, the peaks at 701.0 and 1233.5 cm^{-1} are attributed to the existence of s-triazine unit and bending vibration mode of sp^2 hybridized =C, respectively [70], [82]. The spectrum also presents the other peaks at 473.0, 581.0, 981.0, 1105.5, 1155.4, 1492.0 and 1613.7 cm^{-1} corresponding to the graphitic structure of g-C_3N_4 [70], [82], [90], [91]. This further confirms that the composite contains two phases, WS_2 and g-C_3N_4.

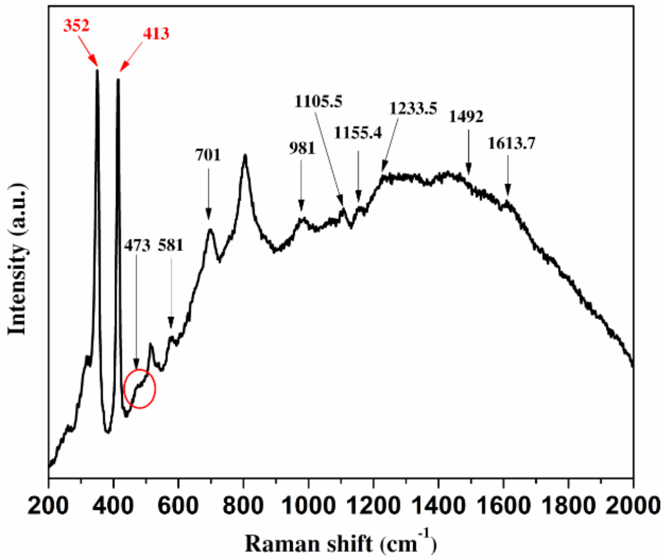

Figure 3.7. Raman spectrum of 10WCN.

3.1.1.7. X-ray photoelectron spectroscopy spectra

For the purpose of investigation the composition and chemical state of elements on surface of the composites, 10WCN was also analyzed by XPS spectra as shown in Figure 3.8. Figure 3.8(f) demonstrates the XPS spectrum for 10WCN with the peaks corresponding to the expected elements of the material. Figure 3.8(a) shows the high-resolution spectrum of C1s with the two peaks at binding energy of 284.5 eV and 288 eV, which are attributed to C-C and C-N-C bonding [90], [203], [216]. The first peak may come from the reference C of the XPS instrument itself and the defect-containing sp^2 hybridized carbon atoms presenting in graphitic domains. The second one may be ascribed to the C sp^2 of graphitic carbon nitride [90]. As presented in Figure 3.8(b), XPS spectrum of N1s was decomposed into two characteristic peaks at 398.6 eV and 400.2 eV ascribing to the N sp^2 in the s-triazine rings and pyridinic-liked N bonded to C as $N\text{-}(C)_3$ or $H\text{-}N\text{-}(C)_2$, respectively [90], [203], [216]. Figure 3.8(c) describes the S2p XPS spectrum with two peaks at binding energy of 161.7 eV ($S2p_{3/2}$) and 163 eV ($S2p_{1/2}$), confirming the S^{2-} species [4], [171]. For the W element in the composite, Figure 3.8(d) and (e) present the XPS spectra of W4d and W4f with binding energy of 31.76 eV ($W4f_{7/2}$) and 33.8 eV ($W4f_{5/2}$) as well as two XPS peaks of W4d at 245.6 eV and 258 eV, indicating the chemical valence state of W^{+4} [75], [171], [216]. Besides, Figure 3.8(e) also shows the peaks at 34.7 eV and 36.9 eV, which demonstrate the existence of W^{+6} due to the partial oxidation of WS_2 during calcination process [78], [216].

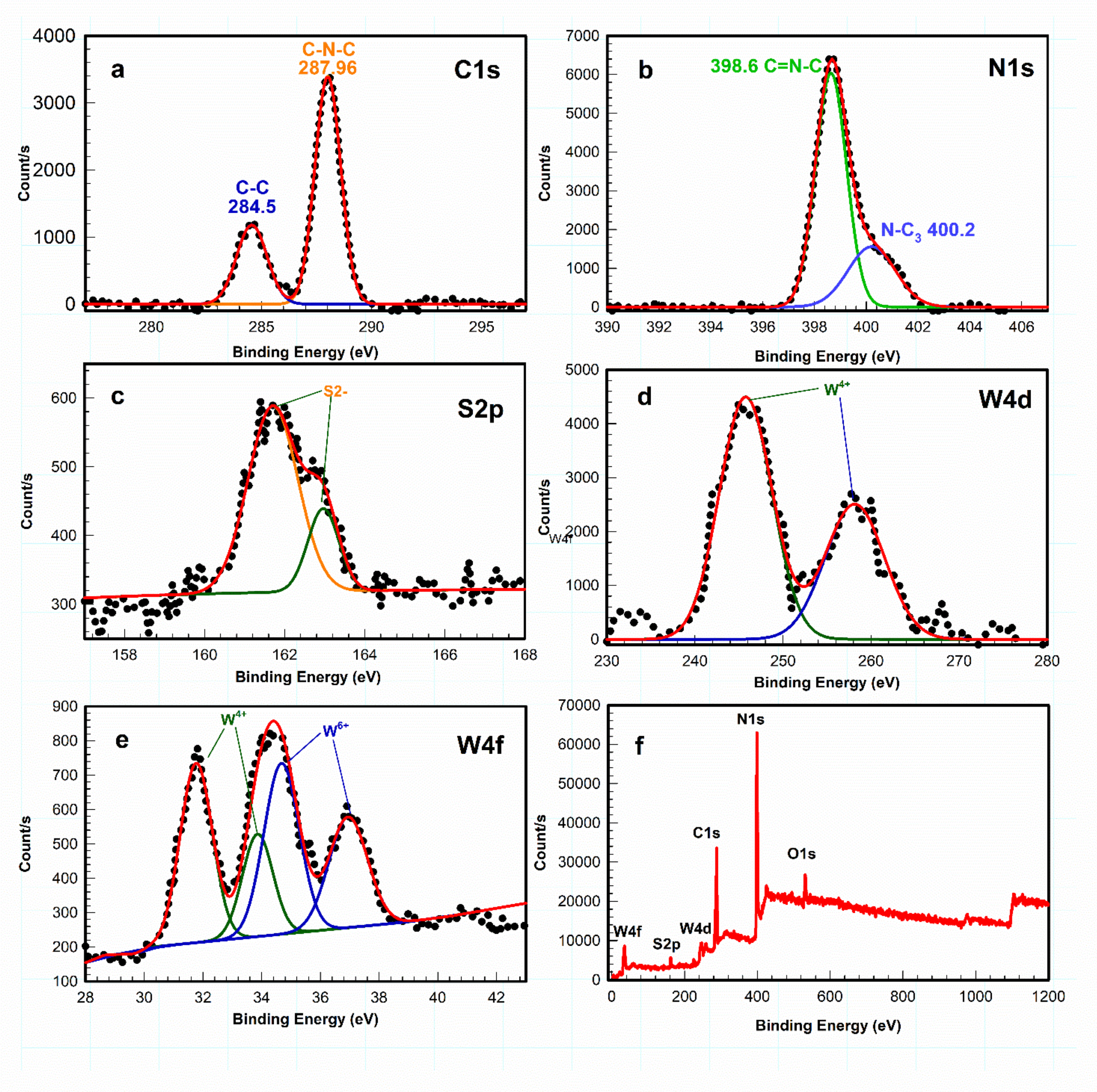

Figure 3.8. High-resolution XPS of C1s (a), N1s (b), S2p (c), W4d (d), W4f (e) and XPS of 10WCN (f).

3.1.1.8. Thermogravimetric analysis

The thermal properties of materials were also characterized by thermogravimetric analysis (TGA) in air. It can be observed in Figure 3.9 that there are two steps of weight loss for all the samples: (i) from room temperature to ~150 ^{o}C and (ii) from ~350 to 600 ^{o}C. The former step may be attributed to evaporation of physically adsorbed water. The latter one may come from the WS_2 to WO_3 oxidation (in the temperature range of 350-500 ^oC [14], [194]) combined with the decomposition of g-C_3N_4 (around 550 ^oC [77]). Figure 3.9 also shows that the decomposition of g-C_3N_4 occurred in the region of 500 – 600 ^oC which was reported for the pure material [77]. Interestingly, the decomposition of g-C_3N_4 in the composites came at the lower temperatures compared to pure g-C_3N_4. This phenomenon was observed in some reports [147], [204] and it can be explained by the catalytic role of WS_2 or the disturbing effect of WS_2 to the interlayer stacking structure of g-C_3N_4. For WS_2 and 5WCN, 7WCN, 10WCN composites, there was no further weight loss over 550 ^oC, suggesting a complete WO_3 conversion from WS_2. Based on the observed TGA data in Figure 3.9, the weight percentages of WS_2 in 5WCN, 7WCN and 10WCN composites can be calculated to be 65.6, 48.0 and 38.2%, respectively. This is accordant with the above obtained results that in the composites, relative amounts of WS_2 decreased while g-C_3N_4 amount increased in the order from 5WCN to 7WCN and 10WCN.

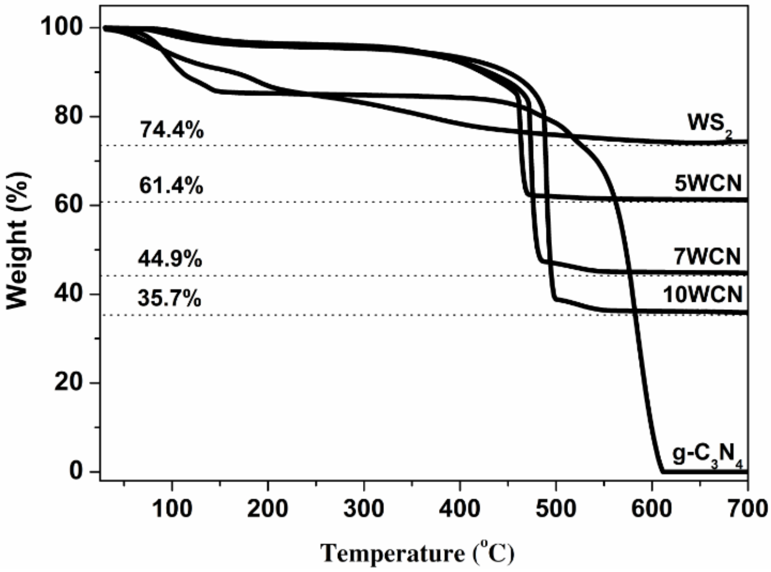

Figure 3.9. TGA curves of samples 5WCN, 7WCN, 10WCN, WS_2 and g-C_3N_4.

3.1.1.9. UV-Vis diffuse reflectance spectra

In order to evaluate the light-harvesting ability of the obtained samples, the UV-Vis diffuse reflectance spectra were conducted. As shown in Figure 3.10, g-C_3N_4 has an absorption edge at ~450 nm, which demonstrates the typical band gap of 2.7 eV for pure g-C_3N_4 [4], [147], [204]. WS_2 displays an extended absorption up to 800 nm due to the narrow band gap (~1.35 eV). For the composites, the absorption intensities strongly improved and extended to 800 nm, which can be explained by the contribution of optical absorption of WS_2 [4]. This extended optical absorption of the composites may result in an enhancement in photocatalytic activity under visible light.

In general, from the observed results prove that the synthesis of WS_2/g-C_3N_4 composite was successful using a facile method via heating the mixtures of tungstic acid and thiourea, in which thiourea was not only the source of S for forming WS_2 but also for the formation of g-C_3N_4 coating on the WS_2 nanosheets. It is expected that this structure could enhance their photocatalytic activity in comparison with the separated components.

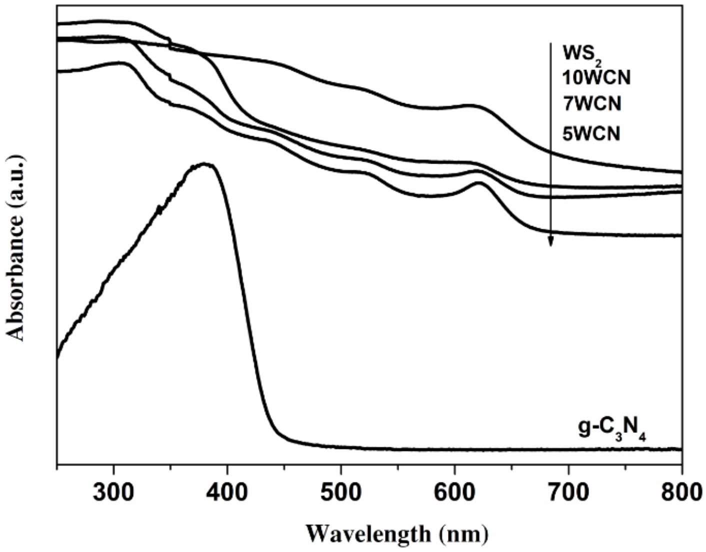

Figure 3.10. UV-Vis diffuse reflectance spectra of 5WCN, 7WCN, 10WCN composites, WS_2, and g-C_3N_4.

3.1.2. MoS_2/g-C_3N_4 characterizations

3.1.2.1. X-ray diffraction patterns

As indicated in Figure 3.11, the XRD patterns of g-C_3N_4 are observed as expected (JCPDS 87-1526). The two peaks located at 27.4^o and 13^o corresponds to the (002) stacking layered structure and the (100) in-plane repeated units, respectively [107], [150], this is also consistent that of g-C_3N_4 in the previous section. The XRD pattern of MoS_2 could be ascribed to hexagonal phase (JCPDS 37-1492) with two peaks located at 32.6 ° and 58.3 ° corresponding to the (100) and (110), these planes are similar to that of WS_2 as mentioned above due to the same crystalline structure. The disappearance of interlayer (002) peak of MoS_2 indicates the formation of MoS_2 nanosheet [107]. The XRD patterns for MCNx (x = 1, 2, 3, 5) are nearly the same as that for g-C_3N_4 and there is no recognizable diffraction peaks corresponding to MoS_2. This may be attributed to the low content of MoS_2 and its high dispersion in g-C_3N_4 [167].

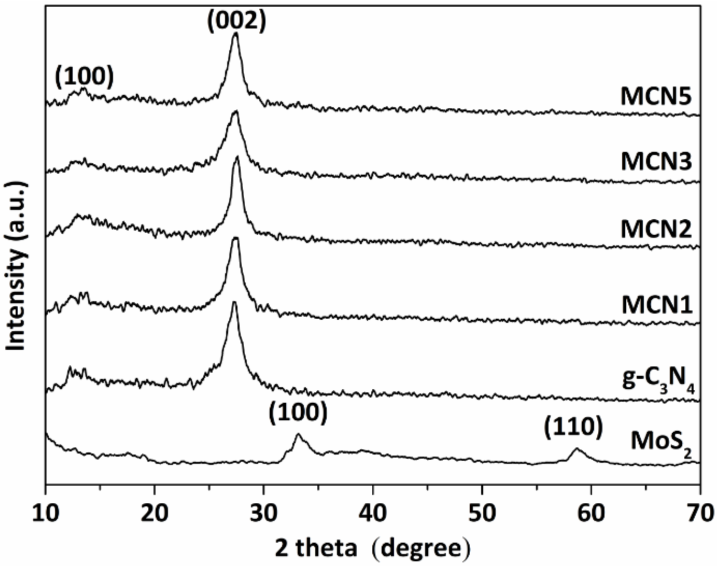

Figure 3.11. XRD patterns of MoS_2, g-C_3N_4, and MCNx (x = 1, 2, 3, 5).

3.1.2.2. Infrared spectra

As shown in Figure 3.12, the absorption bands of g-C_3N_4 from 1650 to 1240 cm^{-1} are attributed to the typical C=N stretching mode and out-of-plane bending vibrations of the C–N bonds in heterocycles of g-C_3N_4 [167], while the sharp absorption peak centered at 807 cm^{-1} is assigned to the characteristic breathing mode of tri-s-triazine cycles. Moreover, the weak peak at 883 cm^{-1} can be assigned to the deformation mode of N-H in amino groups. Meanwhile, the broad peaks between 3000 and 3500 cm^{-1} are ascribed to the stretching vibration of residual free N–H in the bridging C-NH-C units and O–H from the physically adsorbed water on the surface of samples [196], [219]. As expected, the above observation is in agreement with that of g-C_3N_4 in the WS_2/g-C_3N_4 section. Similar to the case of XRD, due to the small amount of MoS_2 contents in the composites there is no difference between the IR spectra of composite samples MCNx and g-C_3N_4. The absence of MoS_2 characteristic peaks in XRD patterns and FT-IR spectra of the composites are consistent with the previous reports [61], [107], [150]. For MoS_2 sample, the disappearance of characteristic bands of g-C_3N_4 implies that this material contains MoS_2 only.

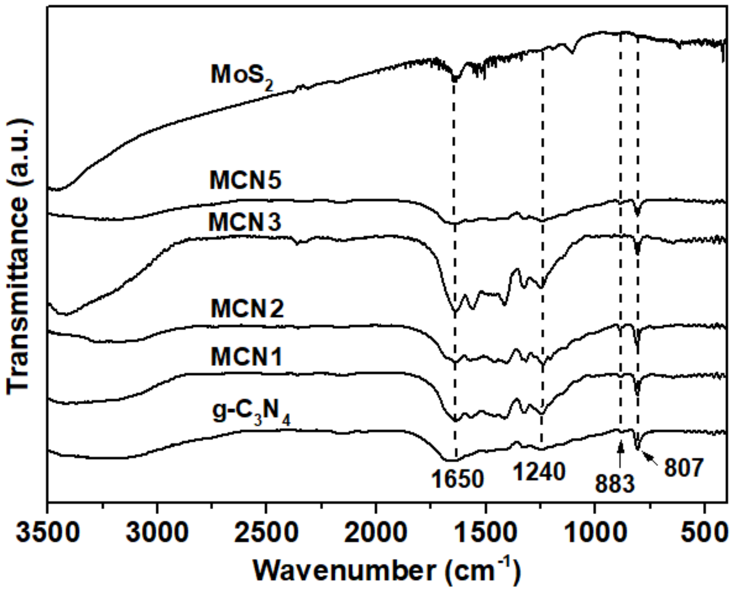

Figure 3.12. FTIR spectra of MoS_2, g-C_3N_4 and MCNx (x = 1, 2, 3, 5) samples.

3.1.2.3. X-ray photoelectron spectroscopy

The presence of MoS_2 in the composite samples can be confirmed by XPS, and MCN5 sample was chosen as a representative. As shown in Figure 3.13(a), the Mo 3d spectrum exhibits two peaks at 228.0 eV (Mo $3d_{5/2}$) and 231.3 eV (Mo $3d_{3/2}$), and in Figure 3.13(b) the two peaks at 160.9 eV and 162.1 eV, correspond to the S $2p_{3/2}$ and S $2p_{1/2}$, respectively. This indicates the existence of Mo^{4+} and S^{2-} in the composite [184]. The appearance of two more weak peaks at 225.3 eV and 234.6 eV in Figure 3.13(a) can be assigned to S 2s and Mo^{6+}, respectively. The latter species may come from the formation of a small amount of MoO_3 on the surface of the composite [67]. The XPS survey spectrum of MCN5 sample was also shown in Figure 3.13(c). The presence of C1s and N1s indicates that existence of g-C_3N_4 in MCN5 sample which are similar to that of g-C_3N_4 in 10WCN as discussed above.

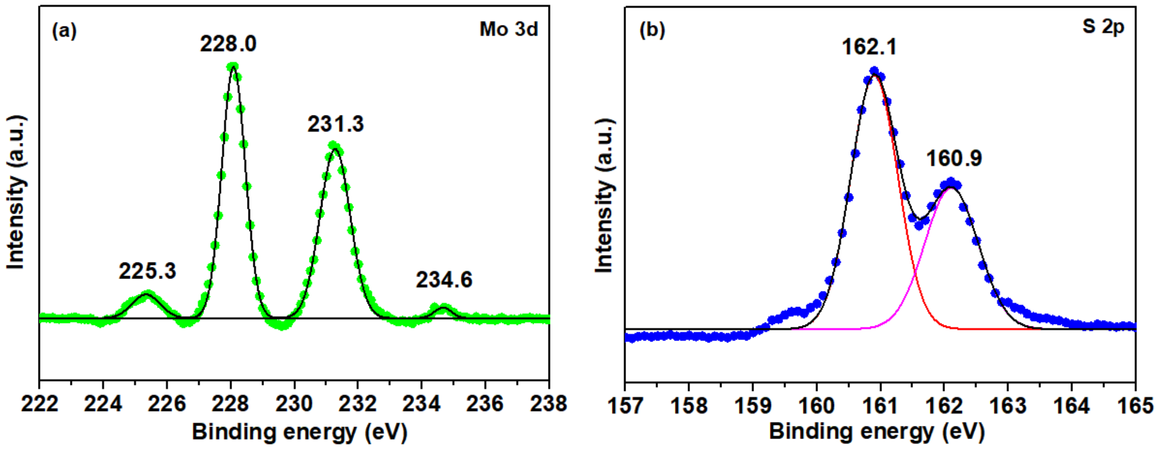

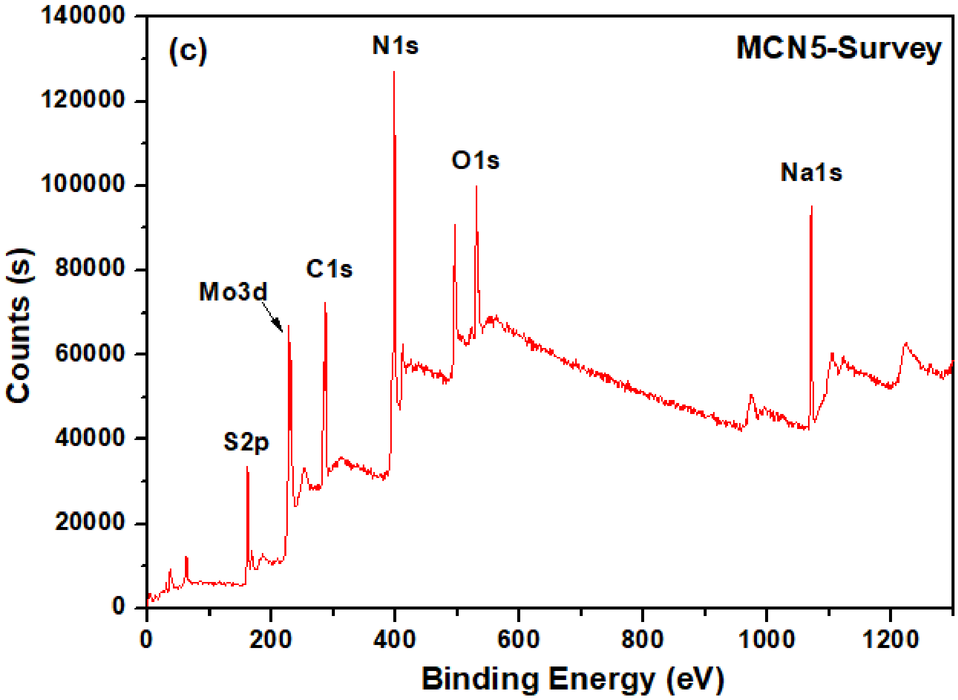

Figure 3.13. XPS spectra of Mo 3d (a), S 2p (b) and (c) XPS survey spectrum of MCN5 sample.

3.1.2.4. Surface area

The BET surface area and pore volume of pure MoS_2, g-C_3N_4 and MoS_2/g-C_3N_4 composites were determined by nitrogen adsorption-desorption isotherms (see Figure 3.14).

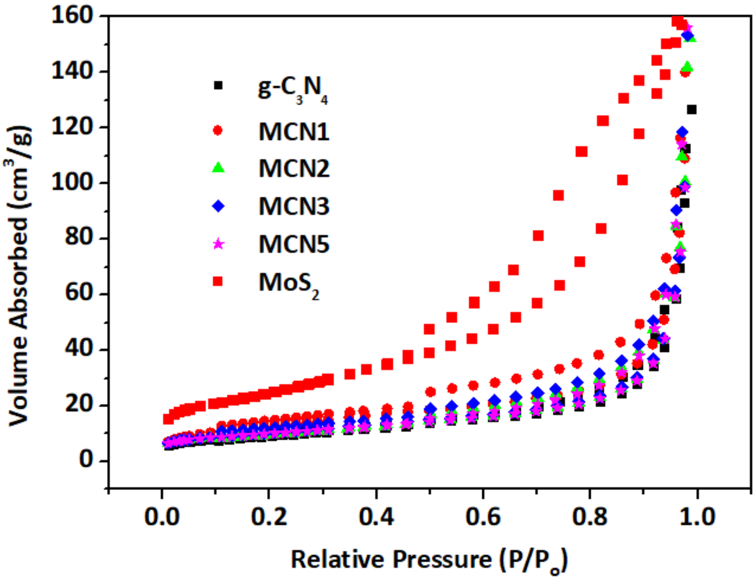

Figure 3.14. N_2 adsorption isotherms of MoS_2, g-C_3N_4 and MCNx (x = 1, 2, 3, 5) samples

The MoS_2 and g-C_3N_4 sample have surface areas of 90.0 $m^2.g^{-1}$ and 34.5 $m^2.g^{-1}$ and a pore volume of 0.276 $cm^3.g^{-1}$ and 0.176 $cm^3.g^{-1}$, respectively. Meanwhile, the corresponding values of MCNx samples are similar to that of pure g-C_3N_4 as shown in Table 3.1. In general, the variation in surface area of the materials is not significant.

Table 3.1. BET specific surface area and pore volume of the g-C_3N_4 and MCNx samples

Samples	g-C_3N_4	MCN1	MCN2	MCN3	MCN5	MoS_2
BET ($m^2.g^{-1}$)	34.5	46.7	36.2	36.8	35.4	90.0
Pore volume ($cm^3.g^{-1}$)	0.176	0.215	0.220	0.235	0.241	0.276

3.1.2.5. Thermogravimetric analysis

The thermal properties of materials were characterized by thermogravimetric analysis (TGA) in Ar atmosphere. Figure 3.15 shows that there are two steps of weight loss for all of the samples as observed for WS_2/g-C_3N_4 samples in the previous section: (1) from room temperature to ~150 °C and (2) from ~400 to 625 °C. The former step may be attributed to evaporation of physically adsorbed water and the latter was the decomposition of the materials, in which the g-C_3N_4's decomposition temperature meets the literature [77]. Interestingly, the decomposition of the composites comes at the lower temperature compared to g-C_3N_4, and this trend of decreasing the decomposition temperature when increasing the MoS_2 content of the composites can be observed in all the samples. This phenomenon was observed in some reports [77], [170] and it is explained by the catalytic role of MoS_2 or the disturbing effect of MoS_2 to the interlayer stacking structure of g-C_3N_4. The TGA data shown in Figure 3.15 also confirmed the small amount of MoS_2 in the composites, this agrees with XRD data as indicated previously. For MoS_2 sample, a decrease by 10% could be attributed to the physically adsorbed water as discussed above.

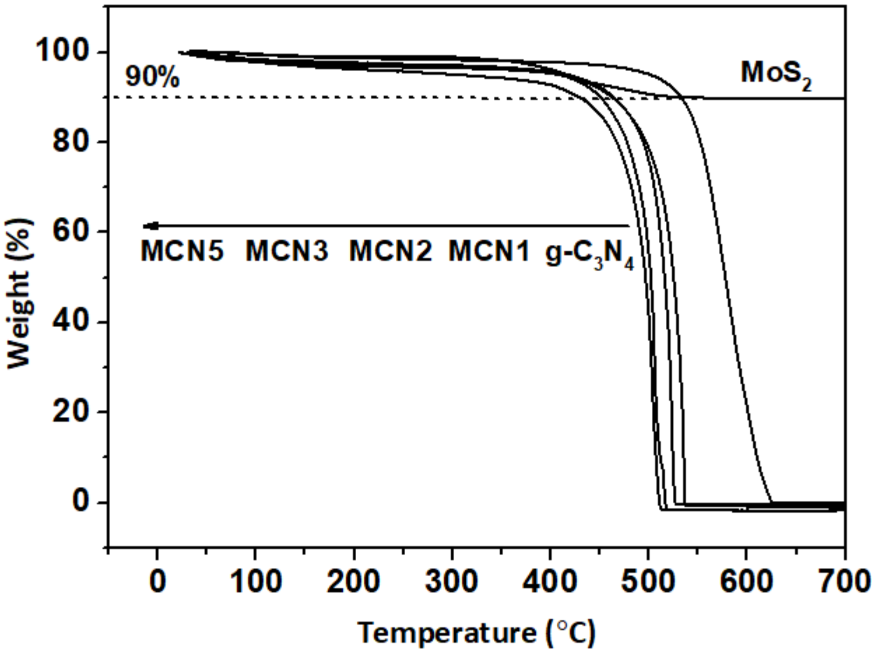

Figure 3.15. TGA curves of samples MoS_2, g-C_3N_4, and MCNx (x = 1, 2, 3, 5) in Ar atmosphere.

3.1.2.6. UV–vis diffuse reflectance spectroscopy

To investigate the light harvesting properties of the samples, UV–vis diffuse reflectance spectroscopy (DRS) was performed and the spectra are shown in Figure 3.16. The g-C_3N_4 sample shows absorption from UV through the visible range up to 450 nm which can be assigned to the intrinsic band gap of g-C_3N_4 (2.78 eV). For the composites, although there are not significant changes in the band gap values (see detailed calculation in Figure 3.16b), the absorption intensity increases from MCN1 to MCN5 in the visible light region as compared to g-C_3N_4, which can be attributed to the presence of MoS_2 in the composite, resulting in high visible light photocatalytic performance. For MoS_2 sample, it could absorb light with the wavelength from 700 nm. The bandgap of MoS_2 nanosheet was 2.1 eV which calculated using Tauc plot method, this value is consistent with previous study [133], [120].

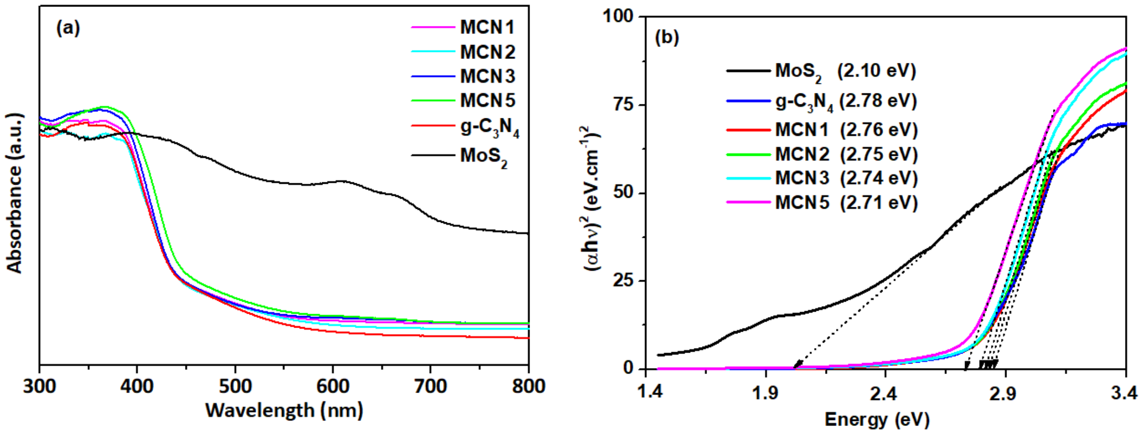

Figure 3.16. UV-Vis absorption spectra (a) and corresponding Tauc plots (b) of MoS_2, g-C_3N_4, and MCNx (x = 1, 2, 3, 5).

3.1.2.7. Elemental mapping

In order to confirm the distribution and uniformity of MoS_2 and g-C_3N_4 in the composites, EDS elemental mapping was applied, and MCN2 was chosen as a representative. Figure 3.17 shows that expected presence of C, N, S and Mo elements in uniform distribution can be observed.

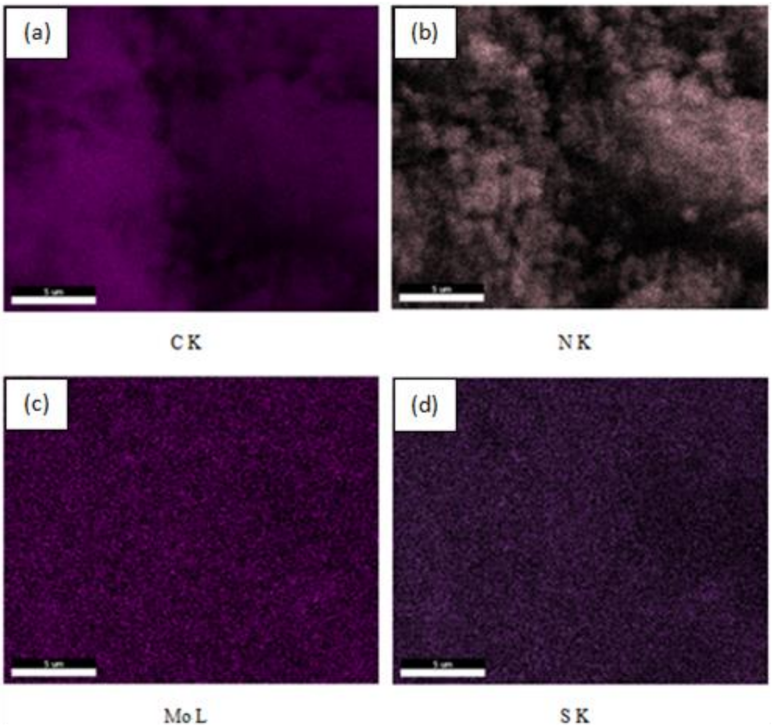

Figure 3.17. EDX elemental mapping of C (a), N (b), Mo (c) and S (d) elements for MCN2 sample.

This result indicates that MoS_2 and g-C_3N_4 are combined uniformly throughout the composite. This shows that the composite possesses heterostructures and close contact between the components, g-C_3N_4 and MoS_2, which could favour the transfer of photogenerated charge carriers, therefore enhancing the charge separation and the photocatalytic activity of the composites as you will see details in the next section.

3.2. MATERIAL PHOTOCATALYTIC ACTIVITY

3.2.1. Adsorption-desorption equilibrium time

The needed time for reaching adsorption-desorption equilibrium of the material toward the target molecule is vital for the subsequent photocatalytic activity investigation. For xWCN samples, that time required for the equilibrium towards methylene blue was shown in Figure 3.18.

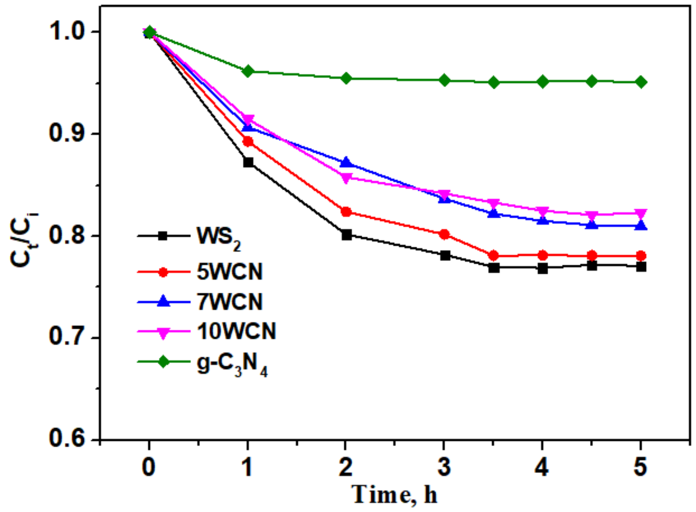

Figure 3.18. Adsorption-desorption equilibrium of MB over WS_2, 5WCN, 7WCN, 10WCN and g-C_3N_4 in the dark. Conditions: initial MB concentration 30 mg.L^{-1}, pH 6.4, catalyst loading 1.1 g.L^{-1}.

This figure showed that after 4 hours of magnetic stirring in the dark the equilibrium was established. Then, for this type of materials towards MB, 4 hours was the required time before illuminating. The study of equilibrium was also conducted for the MCNx samples with the result shown in Figure 3.19, the time needed for reaching equilibrium towards RhB of the materials was 45 minutes. In the experiments related to these samples of the following sections, 1 hour was the time for the dark experiment.

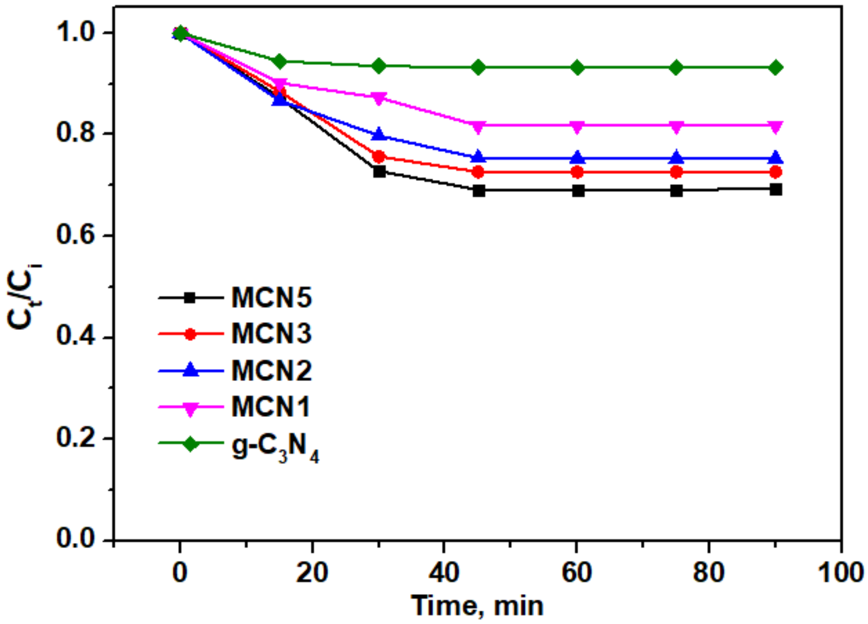

Figure 3.19. Adsorption-desorption equilibrium of RhB over MCN5, MCN3, MCN2, MCN1 and g-C_3N_4 in the dark. Conditions: initial MB concentration 5 mg.L^{-1}, pH 3, catalyst loading 0.7 g.L^{-1}.

A big difference in adsorption capacity of MoS_2 towards RhB was indicated in Figure 3.20. For the 25-ppm initial-concentration of RhB, 85% of that dye was adsorbed onto the surface to reach the equilibrium after 4 hours under magnetic stirrer in the dark. This time was used for this material to get the equilibrium.

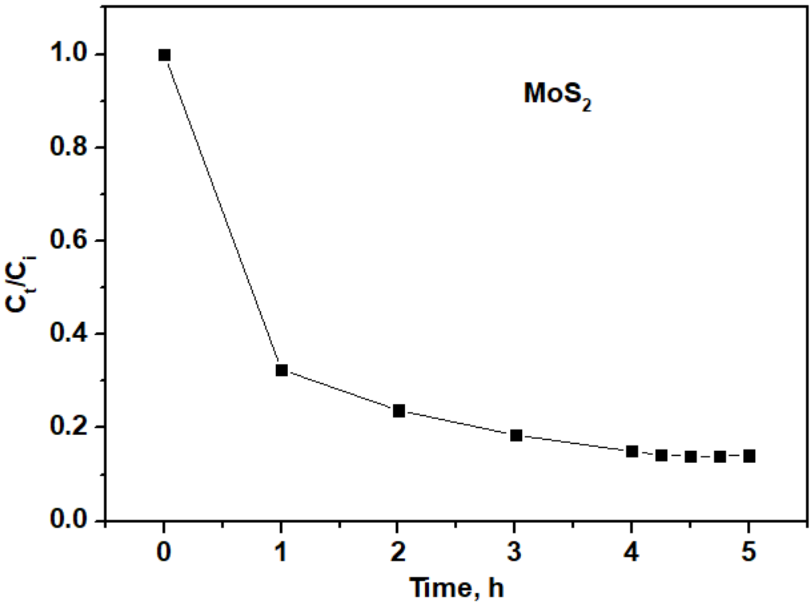

Figure 3.20. Adsorption-desorption equilibrium of RhB over MoS$_2$ in the dark. Conditions: initial MB concentration 25 mg.L^{-1}, pH 3, catalyst loading 0.7 g.L^{-1}.

In other cases, when pH solution changes the needed time for the equilibrium was also investigated before starting the evaluation of the photocatalytic activity.

3.2.2. Photocatalytic activity comparisons

The photocatalytic activity of all the WS$_2$/g-C$_3$N$_4$ samples was evaluated by methylene blue (MB) photodegradation in aqueous solution as shown in Figure 3.21. For comparison, the photocatalytic activity of WS$_2$ and g-C$_3$N$_4$ are also presented. Figure 3.21 shows that WS$_2$ and g-C$_3$N$_4$ exhibited a low activity which may be due to high recombination rate of photogenerated electron-hole pairs in the pure semiconductors [187]. For the composites, a strong improvement in activity can be observed from Figure 3.21 as well. However, their activities are different and can be graded in the order 10WCN < 5WCN < 7WCN, which indicates that among the as-prepared composites, the best photocatalyst is 7WCN with a MB degradation of 85.3% after 6 h under visible light irradiation. In order to clarify self-degradation of MB under visible light, a control experiment without photocatalyst was conducted. The result shows that the photolysis of MB can be ignored.

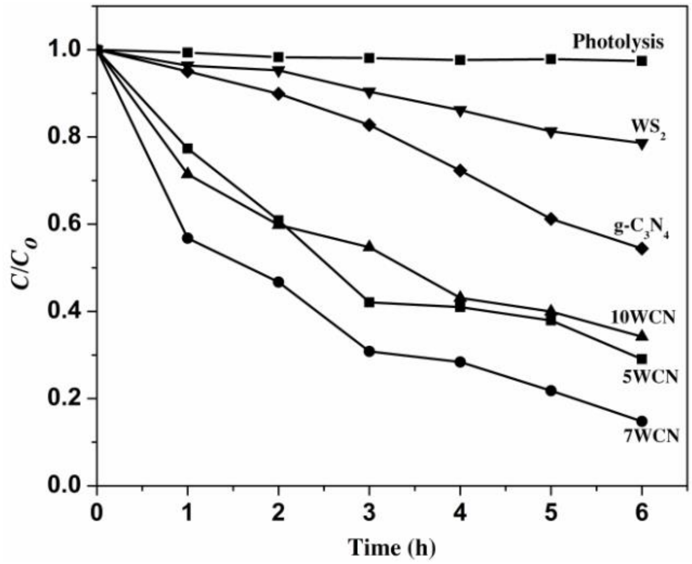

Figure 3.21. Photocatalytic degradation of MB on 5WCN, 7WCN, 10WCN, WS$_2$ and g-C$_3$N$_4$, and without photocatalyst. Conditions of process:irradiated volume: 90 mL, initial MB concentration: 30.0 mg.L^{-1}, pH 6.4, catalyst loading: 1.1 g.L^{-1}, 25^{o}C, under 100 W incandescent lamp.

Based on application of Langmuir-Hinshelwood model, it can be seen in Figure 3.22 that the photodegradation of MB fits well with the pseudo-first-order kinetic model.

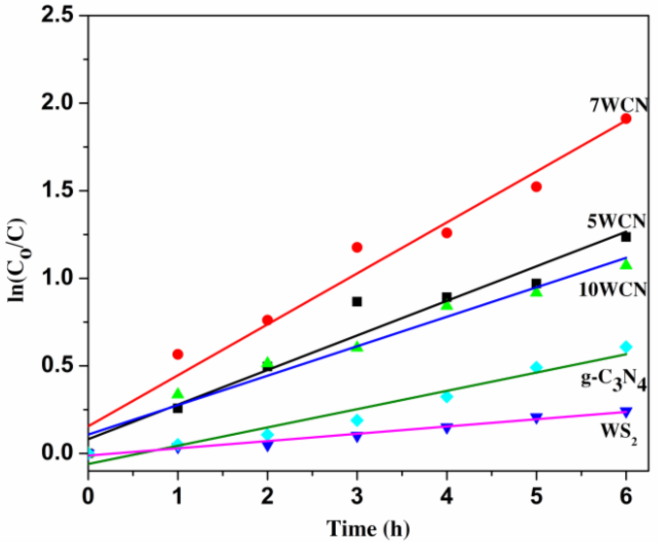

Figure 3.22. First-order kinetic plots for the photodegradation of MB over 5WCN, 7WCN, 10WCN, WS_2 and g-C_3N_4 under specified conditions.

Accordingly, the rate constants of 5WCN, 7WCN, 10WCN, WS_2 and g-C_3N_4 are $3.28x10^{-3}$, $4.85x10^{-3}$, $2.80x10^{-3}$, $6.83x10^{-4}$ and $1.73x10^{-3}$ min^{-1}, respectively. This reflects again that 7WCN is the best material in photocatalytic degradation of MB under the specified conditions. All the composites exhibited the much higher photocatalytic performance than that of the individual materials. This synergistic effect for the composites has been suggested by a reduction of recombination rate of photogenerated electron-hole pairs, leading to enhancing the charge separation and therefore the photocatalytic activity of the composites. Among the composites, 7WCN exhibited the best performance, which can be proposed by an appropriate weight ratio of WS_2 to g-C_3N_4. Indeed, a larger relative content of WS_2 in the composite can result in its property closing to pure WS_2. In contrast, a larger relative content of g-C_3N_4 can receive a performance closing to pure g-C_3N_4.

In order to investigate the best material of the MoS_2/g-C_3N_4 (MCNx) samples, their photocatalytic activities were evaluated by photodegradation of RhB, g-C_3N_4 also included for comparison. As shown in Figure 3.23, there was an improvement in the photocatalytic activity of MCNx samples compared to the individual g-C_3N_4, except for MCN5 and this also indicates that the kinetic of the photodegradation processes were the pseudo-first-order, followed the Langmuir-Hinshelwood model. The composite MCN1 exhibited the best activity with the rate constant of 0.070 min^{-1}. In contrast to the other cases, MoS_2 almost exhibited no photocatalytic activity towards RhB in this particular conditions. This might be due to its high adsoprtion capacity towards the dye, this phenomenon will be explored details in the next sections.

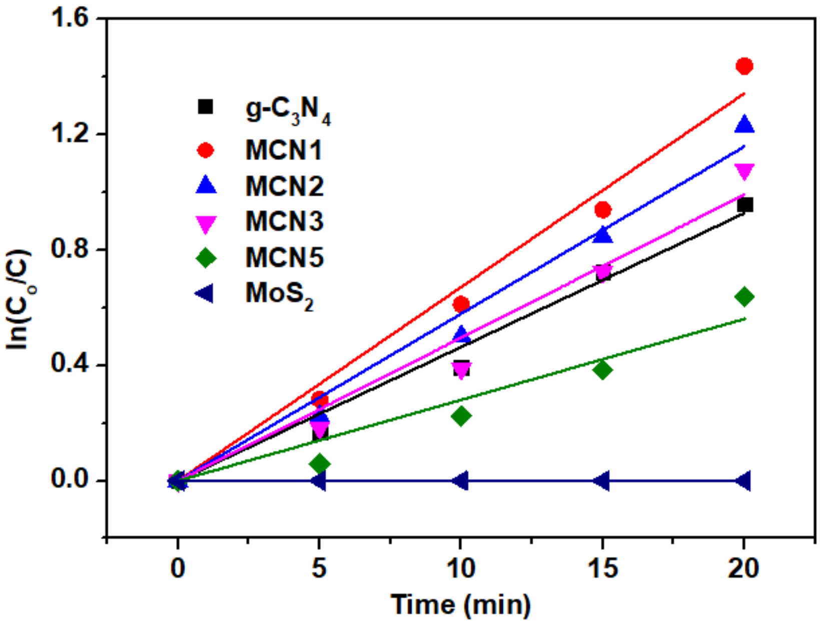

Figure 3.23. First-order kinetic plots for the photodegradation of RhB over MCNx and g-C_3N_4 samples. Conditions of process: irradiated volume: 25 mL, initial RhB concentration: 5.0 mg.L^{-1}, pH 3.0, catalyst loading: 0.7 g.L^{-1}, 25°C, under blue light. Except for MoS_2: initial RhB concentration: 25.0 mg.L^{-1}.

The photocatalytic enhancement of the composites can be ascribed to the charge separation which leads to a decrease in recombination rate of photoinduced charge carriers, which is similar to the above observation for

WS_2/g-C_3N_4. This charge separation was supported by photoluminescence spectra (PL) of the two representatives of g-C_3N_4 and the composite MCN1 samples as seen in Figure 3.24.

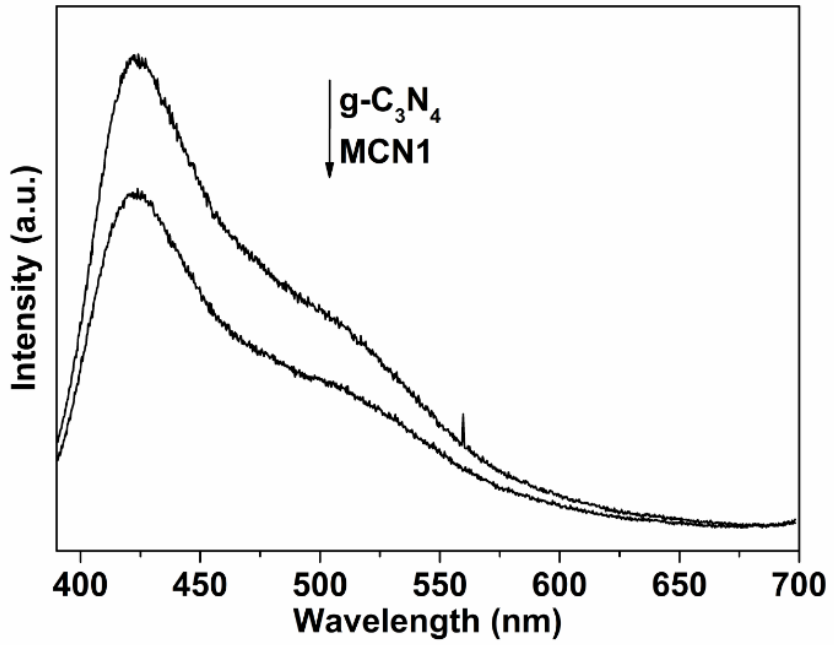

Figure 3.24. PL speactra of g-C_3N_4 and MCN1 sample.

However, when increasing the content of MoS_2, the photocatalytic performance of MCNx decreased, which might be explained by the light blocking effect [106]. This effect was observed most significantly when the content of MoS_2 large enough, as in MCN5 (8.0 wt.% MoS_2/g-C_3N_4) sample, its photocatalytic activity was even lower than that of g-C_3N_4.

3.2.3. Effect of catalyst loading

To find out the optimum catalyst dosage of MoS_2/g-C_3N_4, the photodegradation of RhB with various MCN1 loadings were carried out, as shown in Figure 3.25a. When the catalyst loading increased from 0.3 g.L^{-1} to 0.7 g.L^{-1}, the RhB degradation rate increased due to an increase in the photogenerated electron-hole pairs. However, there is not a significant change in the degradation rate when the catalyst loading is increased from

0.7 to 0.9 g.L^{-1}. Further increase in MCN1 loading results in a slight decrease in the RhB removal. This trend can be attributed to the negative effects of shielding by the suspended catalyst when the loading increased [81], [141].

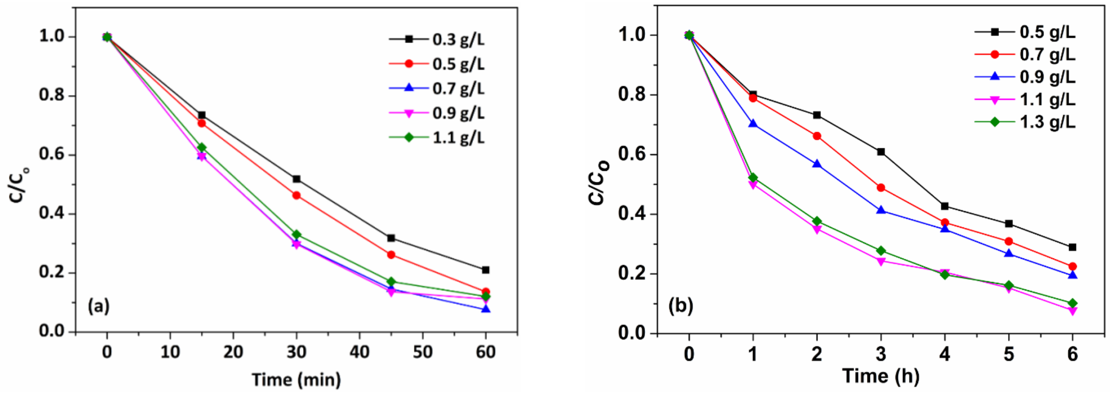

Figure 3.25. Effect of catalyst loading on (a) RhB degradation over MCN1 catalyst in the conditions: irradiated volume: 25 mL, initial RhB concentration: 5.0 ppm, pH: 3.0, 25°C, under blue light, and (b) MB degradation over 7WCN catalyst in the conditions: irradiated volume: 90 mL, initial MB concentration: 30.0 mg.L^{-1}, pH 6.4, 25°C, under 100 W incandescent lamp.

This is proven in Figure 3.26, as the increase of catalyst loading results in the decrease of transmitted light irradiance from the solution. Owing to this effect, the rate of photodegradation is reduced after a threshold MCN1 catalyst loading. Furthermore, Figure 3.26 shows that added catalyst creates a dark zone in the reactor after 13 mm depth. From this result, from now on, the optimum catalyst loading of 0.7 g.L^{-1} of MCN1 sample was employed for other investigations. The effect of this factor was also conducted for 7WCN sample on photodegradation of MB under specific conditions as shown in Figure 3.25b. The trend was similar to that of MCN1 on RhB degradation with the optimum loading of 1.1 g.L^{-1} and this catalyst concentration was applied for further photocatalytic exploration of the catalyst.

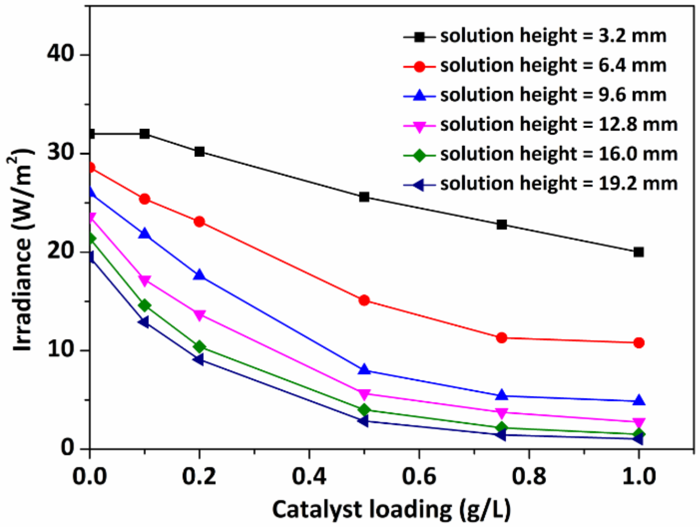

Figure 3.26. Irradiance of transmitted blue light of different RhB solution heights with varying loadings of MCN1 from the solution.

3.2.4. Adsorption and photocatalysis

3.2.4.1. Point of zero charge and existed forms of dye molecules

The experimental values of point of zero charge (pH$_{pzc}$) of MCN1 and 7WCN samples as shown in Figure 3.27 were 3.6 and 2.1, respectively. The pH of the solution affects not only the surface charge of the particles, but also the forms of pollutant molecule in aqueous solution and consequently the adsorption ability of the molecule on the surface.

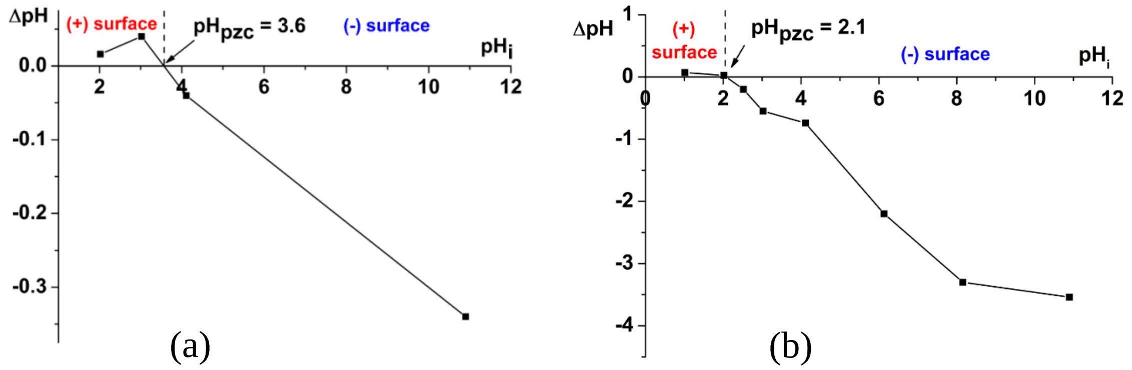

(a) (b)

Figure 3.27. Points of zero charge of (a) MCN1 and (b) 7WCN samples.

The point of zero charge of the material implies that the surface charge of the material will be negative if that point is less than the pH of the solution containing it. Conversely, if the pH of that point is greater than the pH solution the surface becomes positively charged. This specific surface charge for each catalyst is also illustrated in Figure 3.28. The pK_a of RhB in the aqueous solution is 3.22 [183] indicating that it is in the zwitterionic or neutral form in solutions with pH > pK_a, but in the cationic form with pH < pK_a, as seen in Figure 3.28.

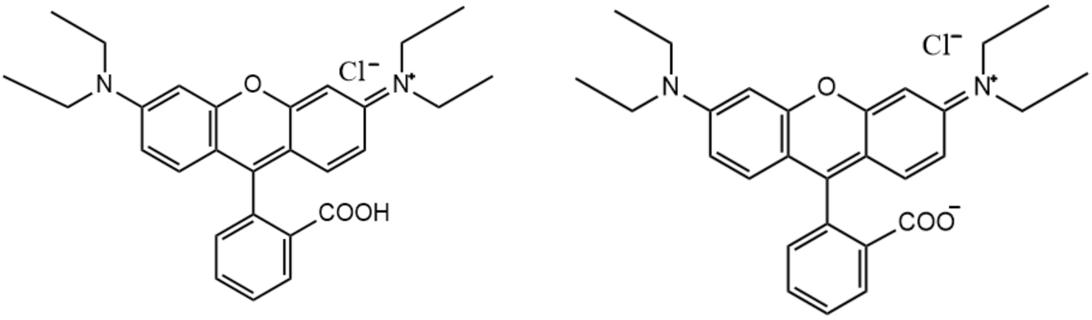

(a) (b)

Figure 3.28. RhB molecule exists as (a) cationic form and (b) zwitterionic form.

Meanwhile, MB differs from RhB molecule in this aspect because it does not contain any functional group as carboxylic group –COOH that can be ionized depending on pH solution as shown in Figure 3.29.

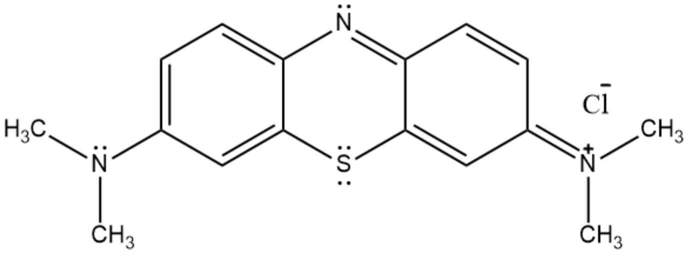

Figure 3.29. The solely existed cationic form of MB

The molecule bears solely positive charge, no matter, the solution is basic or acidic. Another important point is that MB molecule is not bulky as RhB, this facilitates for the adsorption of the former dye onto the surface of investigated material due to the less steric effect compared to RhB molecule.

3.2.4.2. Effect of pH solution, important role of adsorption step

The effect of pH on photodegradation of both RhB and MB over the two catalysts of MCN1 and 7WCN was investigated with wide range values, which were adjusted before irradiation. The first dye we are going to explore the effect over the catalysts is RhB. As shown in Figure 3.30 for MCN1 sample, without adjusting medium (pH = 6.4), very low removal of RhB was observed. Increasing this value to 12.0, the degradation kinetics further slowed down. Surprisingly, a reduction of solution pH to 3.0 led to a dramatic increase of the RhB photodegradation, however, a further pH decrease to 1.5 resulted in a negative effect.

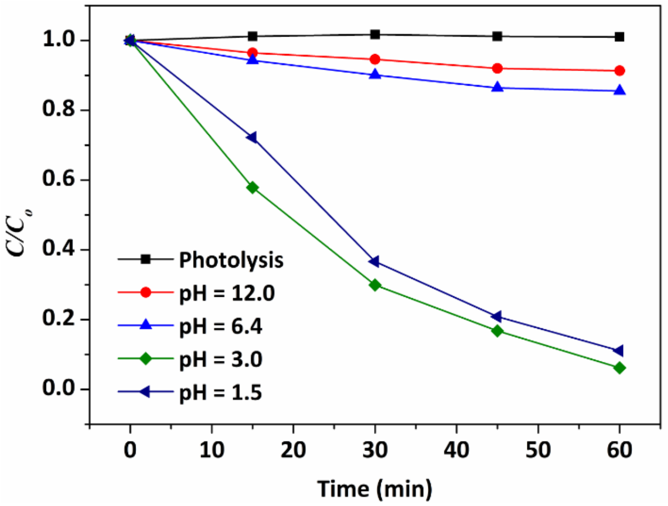

Figure 3.30. Effect of initial pH on RhB degradation over MCN1 photocatalyst. Process conditions: initial concentration, 5.0 ppm; catalyst loading: 0.7 g.L^{-1}; 25^{o}C; under blue light.

A pH-effect experiment on RhB degradation also was carried out over 7WCN catalyst as indicated in Figure 3.31. The trend is similar to that of RhB over MCN1, that means a low pH solution was favourable for the photodegradation reaction, however, this positive effect was interrupted if the solution was too acidic, at pH 1.5 as an example.

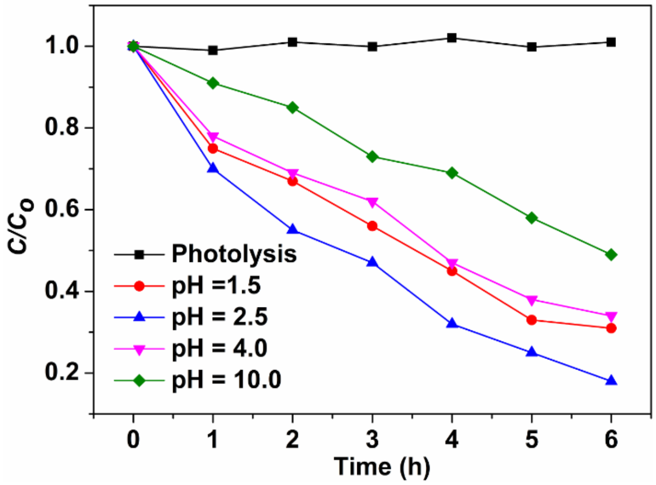

Figure 3.31. Effect of initial pH on RhB degradation over 7WCN photocatalyst. Process conditions: initial concentration, 30.0 ppm; catalyst loading: 1.1 g.L^{-1}; 25^{o}C; under 100 W incandescent lamp.

The common feature of the RhB photodegradation over MCN1 and 7WCN catalysts at different pH solutions is that the reaction rate reaches highest value at the pH smaller than RhB's pK_a of 3.22 and close to the point of zero charge. At pH value less than the pK_a, the carboxylic group existed as protonated form (see Figure 3.28a), therefore, the strong hydrogen bonds between carboxylic acid groups and remaining lone pairs of electron on nitrogen atoms on the material's surface resulting in the increase of substrate adsorption [123]. However, at pH 1.5, the surface of both the catalysts becomes more positive resulting in a higher repulsive force, which affected the reaction rate negatively. In the cases of pH from value of 4, the dye molecule exists as neutral form (see Figure 3.28b) which tends to create a stable dimer due to the electrostatic attraction between the carboxyl and xanthene groups of the individual molecules [68], resulting in the sharp fall of the adsorbed dyes on the surface of the photocatalysts, therefore a dramatic decrease in the photodegradation rate. The specific amount of RhB adsorbed onto the catalysts was shown in Figure 3.32. This data strongly supported for the argument as said above.

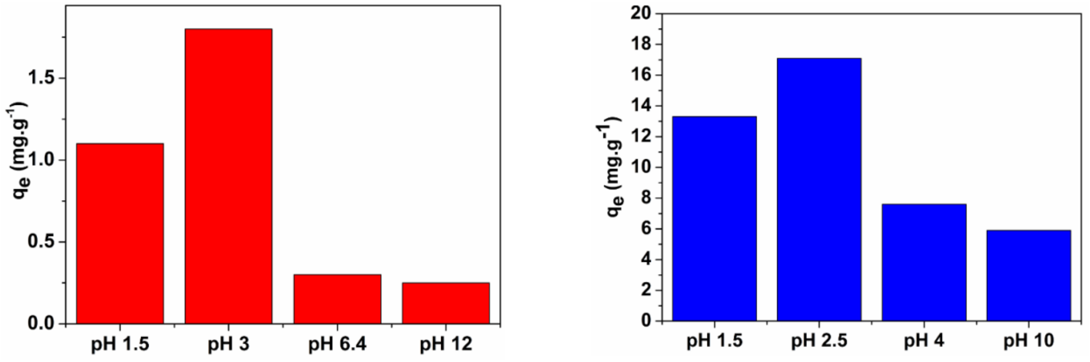

(a) (b)

Figure 3.32. Adsorption capacity of MCN1 (a) and 7WCN (b) materials toward RhB at different solution pHs

This interesting result confirmed that the crucial role of the adsorption of the target molecule onto the surface of the photocatalyst in the photocatalytic process. The importance of the adsorption can be explained due to the fact that the oxidation-reduction reactions during the photocatalytic process mainly happen on the surface of the catalyst but not in the bulk of the solution [195].

The next dye was chosen to investigate the pH effect is MB, existing in solution as an only cationic form which does not depend on the solution pHs. In other words, the pH change of the solution which containing this dye does not make any difference in its existed form. In contrast, this change in pH will result in the surface of the used photocatalyst becoming negatively or positively charged, therefore having an effect on the adsorption capacity of the materials towards the dye. The photodegradation of MB in solution with different pHs over the MCN1 and 7WCN was shown in Figure 3.33.

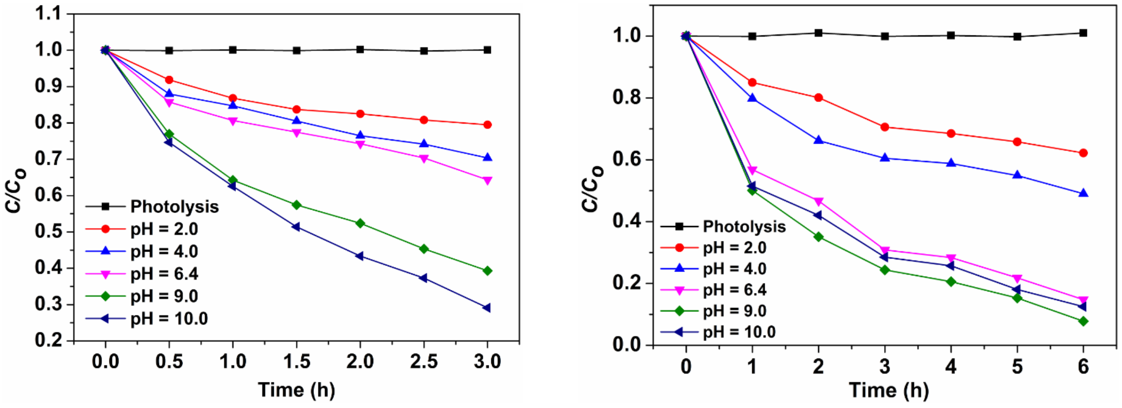

(a) (b)

Figure 3.33. (a) Effect of initial pH on MB degradation over MCN1 photocatalyst. Process conditions: initial concentration, 10.0 ppm; catalyst loading: 0.7 g.L^{-1}; 25°C; under blue light, and (b) Effect of initial pH on MB degradation over 7WCN photocatalyst. Process conditions: initial

concentration, 30.0 ppm; catalyst loading: 1.1 g.L^{-1}; 25°C; under 100 W incandescent lamp.

It is obvious that the favourable medium for the decomposition of MB over the both photocatalysts is alkaline, which completely differs from the RhB case as mentioned above. This observation, again, can be ascribed to the amount of the dye that adsorbed onto the catalysts as indicated in the Figure 3.34 [139].

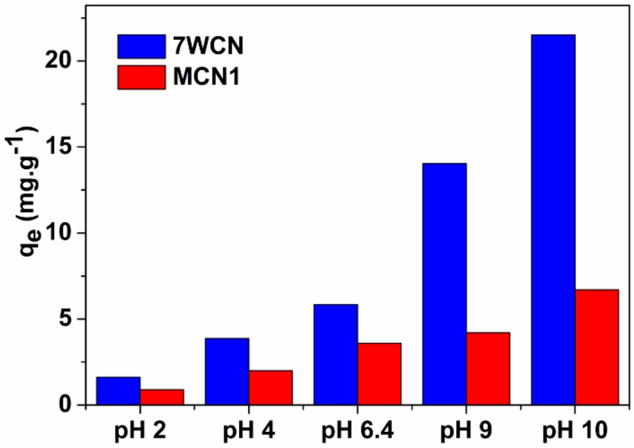

Figure 3.34. Adsorption capacity of 7WCN and MCN1 materials towards MB at different solution pHs.

As increasing the solution pH the amount of adsorbed dye onto the catalyst rises due to the more negative of the surface, especially with the values of pH greater than the pH$_{pzc}$ (3.6 for MCN1 and 2.1 for 7WCN) of the materials. As discussed above MB molecule always has positive charge, this means that the attractive force between the target dye and the surface increases, therefore an increase in the amount of adsorbed molecule and then the photodegradation rate also improved as expected. However, the trend was not identical for the two catalysts, for 7WCN an increase in pH from 9 to 10 did not lead to an increase in MB photodegradation rate as observed for MCN1. This is due to the negative effect of adsorption on the photocatalytic process, the adsorption of the target molecule on the catalyst’s surface is extremely necessary, however, too much adsorbed dye molecule could result in some side effects that slow down the photocatalytic reaction rate. The side effects mentioned above include the shielding of illuminated light, the low adsorbed oxygen molecule and the breakage of hydroxyl groups on the catalyst surface [92].

From the interestingly observed result about the effect of solution pH, thus the level of adsorbed target molecule onto the photocatalyst, on the photodecomposition rate we can come to conclusion that the adhere of the target to the surface of the catalyst during the photocatalytic process plays a vital role along with the different aspects such as the ability of that catalyst itself. No adsorption that means it is unlikely for the decomposition of the target due to the photocatalytic process to be happened, however, a too high adsorption capacity of the material towards the molecule might also cause possibly harmful effect to the photodegradation rate of that target.

3.2.5. A new benchmark for efficiency evaluation of reaction reactor – Photochemical space time yield

3.2.5.1. Calculate reaction rate constant under optimal condition

Under optimal conditions as investigated in the previous section, the reaction rate constants for degrading RhB over 7WCN and MB over both MCN1 and 7WCN materials were calculated using linear fit model as shown in Figure 3.35. The rate constant for reaction of RhB over MCN1 was evaluated with the same method having the value of 0.070 min^{-1} (Figure 3.23).

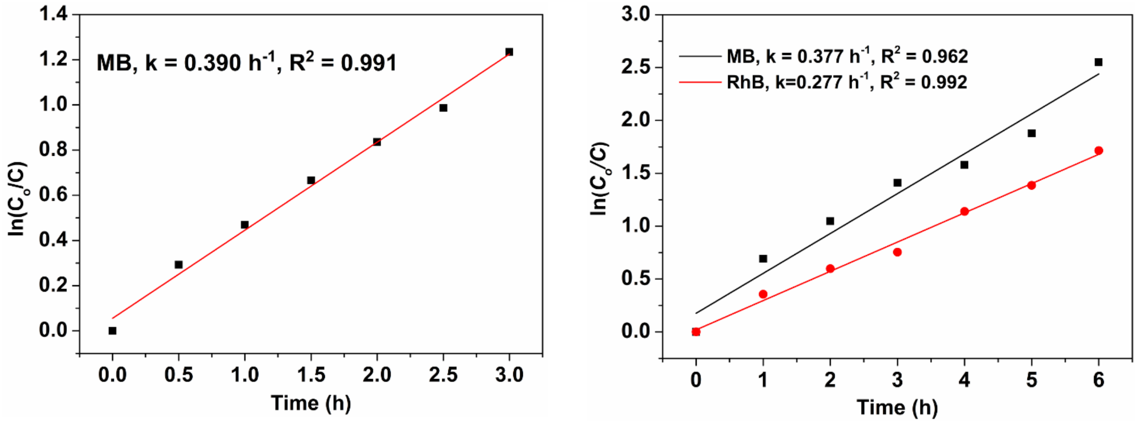

(a) (b)

Figure 3.35. First-order kinetic plots for the photodegradation of: (a) MB over MCN1 material. Conditions of process: irradiated volume: 25 mL, initial MB concentration: 10.0 mg.L^{-1}, pH 10.0, catalyst loading: 0.7 g.L^{-1}, 25^{o}C, under blue light, and (b) MB and RhB over 7WCN material. Conditions of process: irradiated volume: 90 mL, initial dye concentration: 30.0 mg.L^{-1}, pH 2.5 for RhB and 9 for MB , catalyst loading: 0.7 g.L^{-1}, 25^{o}C, under 100 W incandescent lamp.

These rate constants will be used to calculate the photochemical space-time yield (PSTY) of the relevant systems in the following sub-sections.

3.2.5.2. PSTY calculations for the chosen reaction systems

The two reactors that applied for the investigation of photodegradation of RhB and MB dyes over the two catalysts are different from each other in terms of solution volume and the power of light sources, which were blue LED and incandescent lamp. These differences were taken into account in the calculation of the benchmark, PSTY. As evaluated in the previous section, the rate constants for the photodegradation of the dyes were determined. This parameter along with the used volume, the lamp power, and the corresponding PSTY for each system were summarized in Table 3.2. In order to compare the PSTY values of this work and the PSTY for reactors of the mentioned reports, these values also shown in the Table 3.2 as well. The calculated PSTY values as shown in Table 3.2 for the two reaction systems that using the prepared catalysts MoS_2/g-C_3N_4 and WS_2/g-C_3N_4 indicates that each of dyes RhB and MB which was photodegraded over MoS_2/g-C_3N_4 has a much larger PSTY value than that of the corresponding one over WS_2/g-C_3N_4. Specifically, the PSTY values for degradation of RhB and MB over MoS_2/g-C_3N_4 are 3 and 2 order of magnitude larger than those of RhB and MB over WS_2/g-C_3N_4, respectively. The key reasons for this might come from not only the photocatalytic activity of the catalysts themselves, in which the adsorption capacities of the materials towards the dyes play a crucial role in the whole photocatalytic process as discussed in the previous section, but also come from how effective the used lamp converting electric energy into light form is and the spectrum of light produced from that lamp. The significant difference in lamp power of blue LEDs of 0.3 W for the reactor using MoS_2/g-C_3N_4 compared to 100 W incandescent lamp for the other using WS_2/g-C_3N_4 catalyst mainly results in that big difference in PSTY values due to the fact that the LEDs use electricity more efficiently than incandescent bulb, that means it converts much of the electric energy into light form, whereas the latter one wastes much of the energy as heat. Table 3.2 also shows that the reaction rate constant of RhB photodegradation reaction over MoS_2/g-C_3N_4 of this work is higher than one but smaller than the other reference with the same catalyst and the initial concentration of target molecule. However, the benchmark PSTY of this study is 2 orders of magnitude higher than those of the all references. This was particularly interesting since the power of the used light source was significantly lower, namely, 0.3 W vs. 300 W [107]. The result indicates that not only is the synthesized catalyst equally or more efficient in light utilization compared to the literature, but also are the LEDs more effective than the light sources used by the earlier studies.

Table 3.2. *PSTY data for the chosen reaction systems*

Catalyst	Target molecule	k (min^{-1})	STY (day^{-1})	P (kW)	V (m^3)	LP (kW)	PSTY ($day^{-1}.kW^{-1}$)
MoS_2/g-C_3N_4 (this work)	RhB	0.070	0.10	$3x10^{-4}$	$2.5x10^{-5}$	12	**$8.3x10^{-3}$**
	MB	0.0063	$9.1x10^{-3}$				**$7.6x10^{-4}$**
WS_2/g-C_3N_4 (this work)	RhB	0.0046	$6.7x10^{-3}$	0.1	$9.0x10^{-5}$	$1.1x10^{3}$	**$6.1x10^{-6}$**
	MB	0.0063	$9.1x10^{-3}$				**$8.3x10^{-6}$**
Ref. [107]	RhB	0.301	0.432	0.3	$5.0x10^{-5}$	$6.0x10^{3}$	**$7.2x10^{-5}$**
Ref. [150]	RhB	0.036	$5.2x10^{-2}$	0.3	$1.0x10^{-4}$	$3.0x10^{3}$	**$1.7x10^{-5}$**

Both of these factors had significant contributions to the RhB photodegradation under experimentally studied conditions. The efficiency of the LED can be due to its monochromatic behaviour. This way, all of the emitted photons fall within the excitation band of the catalyst. Meanwhile, when using Xe lamp as a light source [107], [150], the number of photons that have enough energy for the excitation only account for a small part of the total emitted photons [137]. This may justify the dramatically lower PSTY values of the state of the art.

Because of the high PSTY value of MoS_2/g-C_3N_4 system, specifically MCN1 sample, compared to WS_2/g-C_3N_4 as discussed above, all the rest sections just used this kind of system for further investigations.

3.2.6. Mechanism investigation

3.2.6.1. Effect of oxidant concentration

In order to prevent the electron-hole recombination, and to improve the photocatalytic activity of a photocatalyst, a suitable electron acceptor can be added to the system. Some inorganic oxidants could be used for this purpose, such as H_2O_2 and peroxodisulphate [141]. The former was chosen for this study over the selected MCN1 catalyst. In the photocatalytic reactions, hydrogen peroxide does not only act as an electron acceptor which promoting charge separation, but also produces hydroxyl radical through the reaction with superoxide radical anion [81] according to the following equations:

$$H_2O_2 + e^-_{CB} \rightarrow OH^{\cdot} + OH^- \qquad (3.1)$$

$$H_2O_2 + O_2^{\cdot -} \rightarrow OH^{\cdot} + OH^- + O_2 \qquad (3.2)$$

As a result, the degradation of RhB after 10 minutes of irradiation increased from 37.1% in the absence of H_2O_2 to 41.5% and 49.9% when the H_2O_2-RhB molar ratio was 50 and 100, respectively, as shown in Figure 3.36.

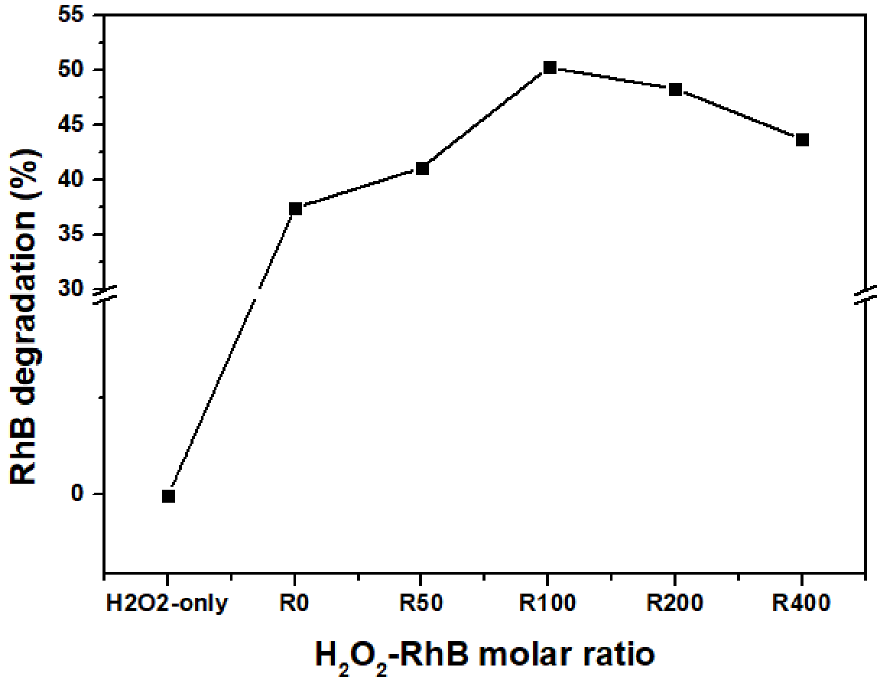

Figure 3.36. Effect of H_2O_2-RhB molar ratio, abbreviated as Rnumber. Process conditions: catalyst loading: 0.7 $g.L^{-1}$, initial RhB concentration: 5.0 ppm, pH: 3.0, 25°C, under blue light.

However, the degradation decreased again when the ratio was greater than 200. This negative effect was due to hole and $OH^{\cdot}$ scavenger function of H_2O_2 at high concentrations. This can be expressed as follows [154]:

$$H_2O_2 + 2h^+_{VB} \rightarrow O_2 + 2H^+ \quad (3.3)$$

$$H_2O_2 + OH^{\cdot} \rightarrow H_2O + HO_2^{\cdot} \quad (3.4)$$

$$HO_2^{\cdot} + OH^{\cdot} \rightarrow H_2O + O_2 \quad (3.5)$$

Therefore, at too high concentration of H_2O_2, the degradation reaction was inhibited. The effect of H_2O_2 itself on the degradation of RhB was also conducted for comparison. It is clear that in the same conditions except the absence of the catalyst RhB still unchanged, this is consistent with previous study [41].

This result shows that how important the presence of an acceptor electron or an oxidant is to the photocatalytic process. Therefore, in the case of without adding oxidizing reagent, the dissolved oxygen in the aqueous solution becomes vital for the photocatalytic reactions. This observation supported the concluded point that we have discussed so far about the adsorption competition of target molecules against the disscoled oxygen molecule onto the surface of the photocatalyst leading to a decrease in the photodegradation rate.

3.2.6.2. Reactive species trapping experiments and proposed photocatalytic mechanism

Generally, the reactive species which participate in the surface reaction during the photocatalytic process, including hole, superoxide radical anion, hydroxyl radical, and electron. To explore which of them having the most contribution to the photocatalytic process, the corresponding reactive species scavengers were employed in the reaction system that use $MoS_2/g\text{-}C_3N_4$ as a photocatalyst to degrade RhB as shown in Figure 3.37.

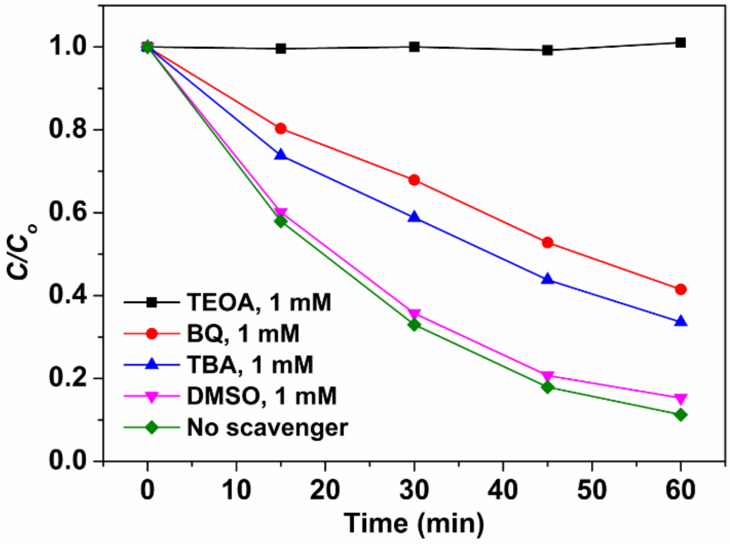

Figure 3.37. Photodegradation of RhB over MCN1 catalyst in the presence of different trapping agents TEOA, BQ, TBA, and DMSO as hole, superoxide radical anion, hydroxyl radical, electron scavengers, respectively.

The changes in RhB photodegradation rate indicated that all the used scavengers had negative effects on the photocatalytic activity of the catalyst to different extents in order of TEOA > BQ > TBA > DMSO. The result also indicated that TEOA scavenger exhibited much stronger inhibition showing that hole was the dominant reactive species in the photodegradation process of RhB over MCN1 catalyst under studied conditions.This important role of hole was supported by the more positive valence band edge of g-C_3N_4 compared to redox potential of RhB (+1.57 V vs. +1.43 V) [197]. The hole of MoS_2 also was able to oxidize RhB directly due to its more positive potential +2 V [133]. Meanwhile, the quite strong adverse-effect caused by BQ and TBA scavengers revealed that the oxygen reactive species, namely, the superoxide radical anion and hydroxyl radical also play their important part in the overall photocatalysis. The formation of these species could be attributed to the more negative potential of electron which generated from g-C_3N_4 conduction band edge -1.13 V compared to the reduction potential of the redox pair $O_2/O_2^{\cdot-}$ of -0.28 V [193]. Furthermore, the $OH^{\cdot}$ radical was just produced from $O_2^{\cdot-}$ as discussed detailedly later, this resulted in decreasing its role in the whole process. Meanwhile, the direct formation of this type of reactive species from H_2O and hole was unfavorable energetically due to the too much positive potential of the pair $OH^{\cdot}/H_2O$. However, the role of electron in the process was insignificant as seen in the Figure 3.38, when there was a presence of DMSO, an electron scavenger, just a minor effect observed on the photodegradation rate of RhB over the catalyst.

From the exploration of the role of reactive species as discussed above and the separation of charge in the composite as seen in PL spectra in Figure

3.24 could help us to propose a photocatalytic mechanism as illustrated in Figure 3.38a.

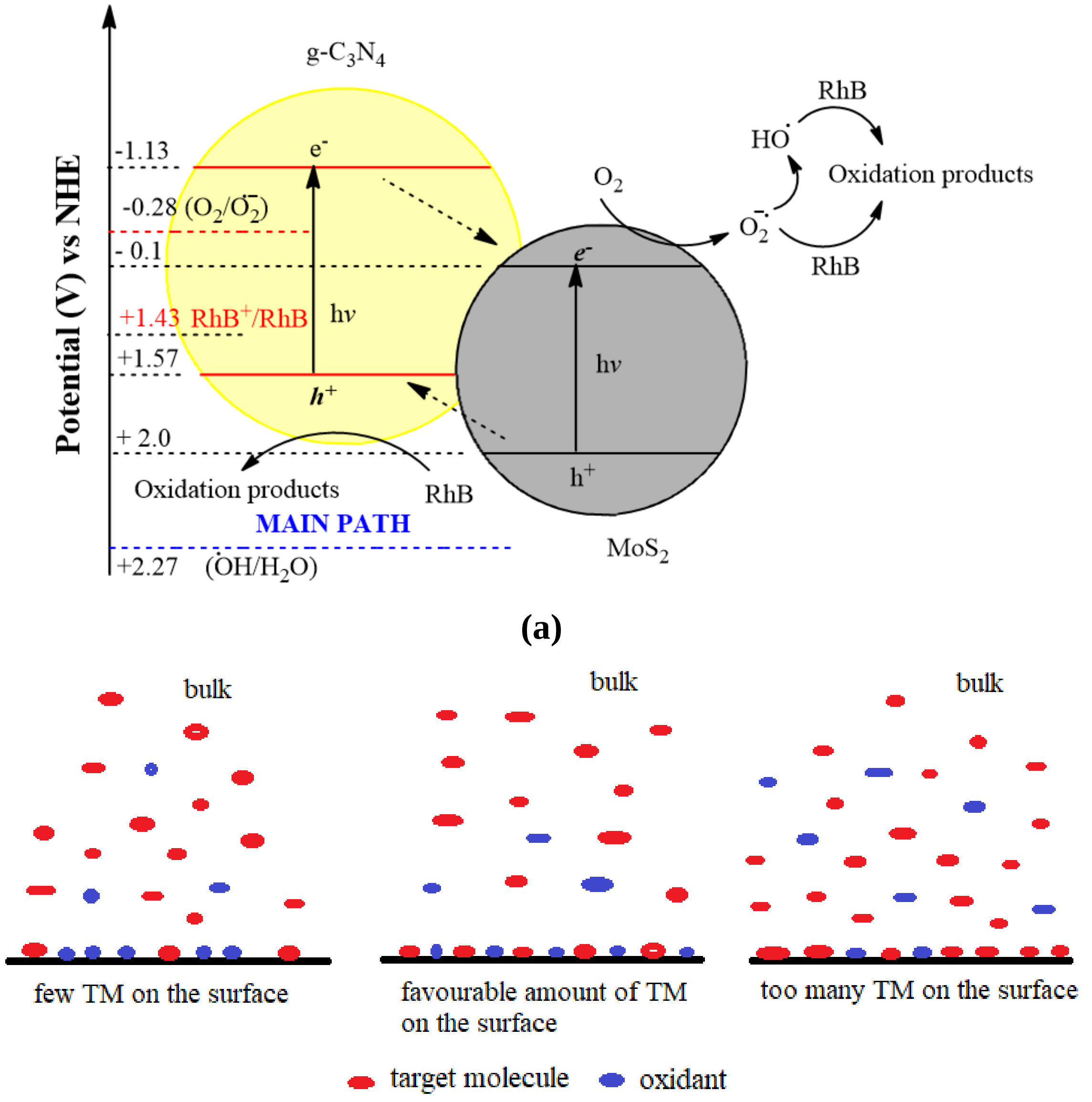

(a)

(b)

Figure 3.38. a) Proposed photocatalytic mechanism over MoS_2/g-C_3N_4 under visible light and b) proposed model for relationship between adsorption and photocatalysis.

The charge separation could be attributed to the lower conduction band position of MoS_2 in the composite leading to its ability to receive photoexcited electron from g-C_3N_4 [150], which favours the separation of electron-hole pairs. The separated electrons on the surface of MoS_2 reduces present oxidants in the solution. In the case of dissolved oxygen this reduction step, which also occurs on the surface, can be given as,

$$O_2 + e^- \rightarrow O_2^{\cdot -} \quad (3.6)$$

The formed superoxide radical anion continuously undergoes three more steps to release hydroxyl radical $OH^{\cdot}$ which are described as follows [22]:

$$O_2^{\cdot -} + H^+ \rightarrow HOO^{\cdot} \quad (3.7)$$

$$HOO^{\cdot} + H^+ + e^- \rightarrow H_2O_2 \quad (3.8)$$

$$H_2O_2 + e^- \rightarrow HO^{\cdot} + OH^- \quad (3.9)$$

Hydroxyl radical is a strong oxidizing species would degrade the organic pollutants in the solution. Meanwhile, the accumulated holes on the surface of g-C_3N_4 could directly oxidize the adsorbed dye molecule on the surface,

$$h^+ + \text{dye} \rightarrow \text{intermediates} \rightarrow CO_2 + H_2O + \text{other simple molecules} \quad (3.10)$$

This reaction (3.10) of oxidizing the target molecule mainly contributed to the overall process as supported in the carrier trapping experiments.

The Equations from 3.6 to 3.9 relating to oxygen and the role of H_2O_2 as discussed in the previous subsection indicate that how important the presence of oxidant on the surface is, any factor that introduces a decrease in amount of that molecule on the catalyst surface would lead to a negative effect on the overal rate of photodegradation of pollutant. This could be explained using the model as shown in Figure 3.38b, in the case of just few target molecules adsorbing on the catalyst surface, the reaction rate for this would be low due to the low adsorbed-molecule number. When that number increases, so does the rate because the oxidizing reagent molecules still are enough for the photocatalytic process, however, if the adsorbed molecules continue to increase, this would reduce the space for oxidant molecules to be adsorbed, then might result in a decrease in overall rate. This model seems to satisfy with the result has been observed so far.

The significant role of hole in the photodegradation of the dye was clarified by a proposed mechanism of transformation of RhB to intermediates. The UV-Vis spectra of RhB solution after 120 min of illumination the optimal conditions as indicated above was shown in Figure 3.39.

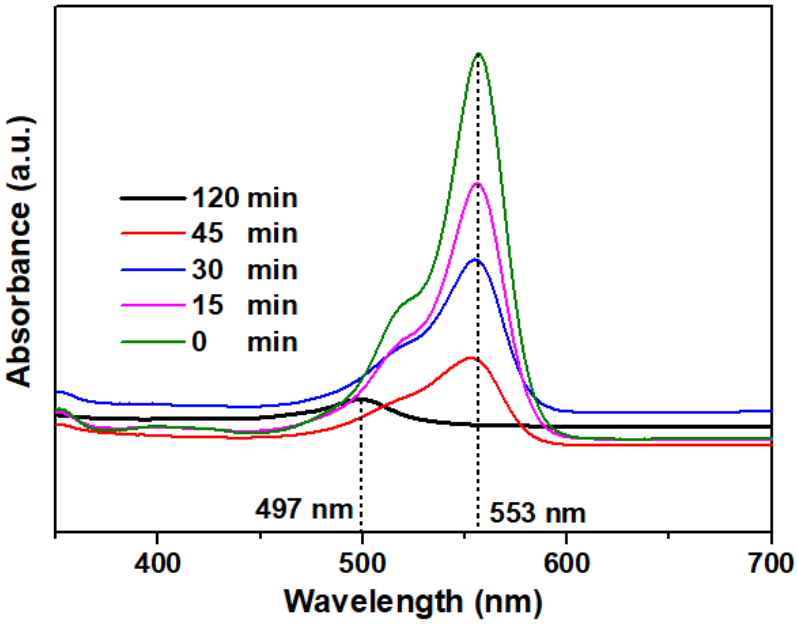

Figure 3.39. Time-dependent adsorption spectra of RhB solution. Conditions of process: irradiated volume: 25 mL, initial RhB concentration: 5.0 mg.L^{-1}, pH 3.0, MCN1 catalyst loading: 0.7 g.L^{-1}, 25°C, under blue light.

It is obvious that after 120 min of illumination the maximum wavelength was shifted from 553 nm to 497 nm corresponding to the transformation of RhB to RhB 110 [123] with the structures shown in Figure 3.40.

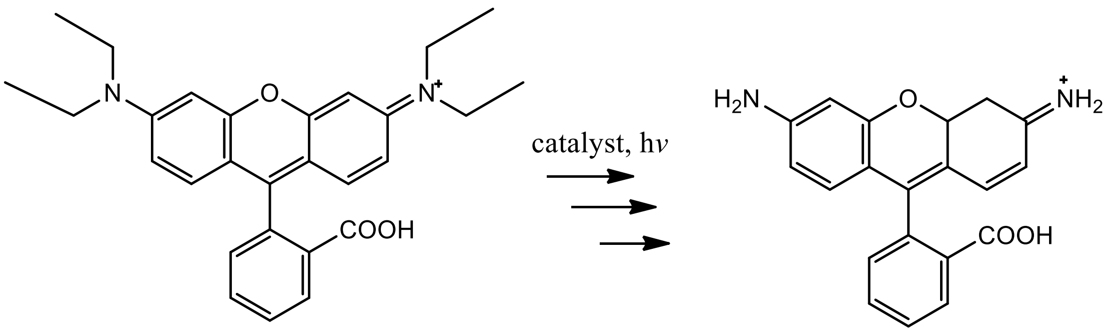

Rhodamine B, λ_{max} = 553 nm

Rhodamine 110, λ_{max} = 497 nm

Figure 3.40. An intermediate of rhodamine B transformation, rhodamine 110.

3.2.7. Applications

3.2.7.1. Photodegradation of a selected antibiotic, enrofloxacin

Enrofloxacin (ENR) is a colorless antibiotic substance which contains both amino and carboxylic groups. This aspect is similar to that of RhB molecule, which could guide us to guess the acidic aqueous solution will be suitable for the photodegradation of this antibiotic over $MoS_2/g\text{-}C_3N_4$ under visible light. Figure 3.41 shows that the pH 4 was favourable for the photodegradation of ENR, an acidic medium, as expected.

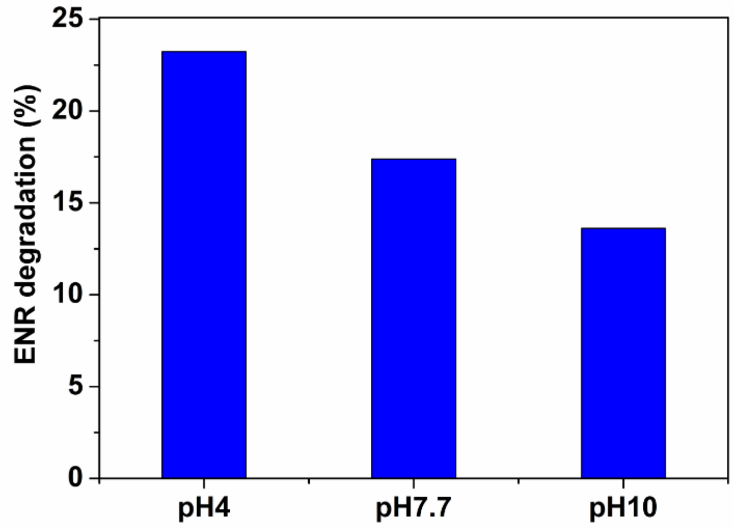

Figure 3.41. Photodegradation of 20 mL ENR of 5 ppm, catalyst loading: $0.5 g.L^{-1}$, under blue light (0.2 A, 3.0 V) for 2h, 25°C at different pHs.

The optimal catalyst loading was also obtained from Figure 3.42 with the value of 1 g/L. Here, the similar trend also observed as those of RhB and MB.

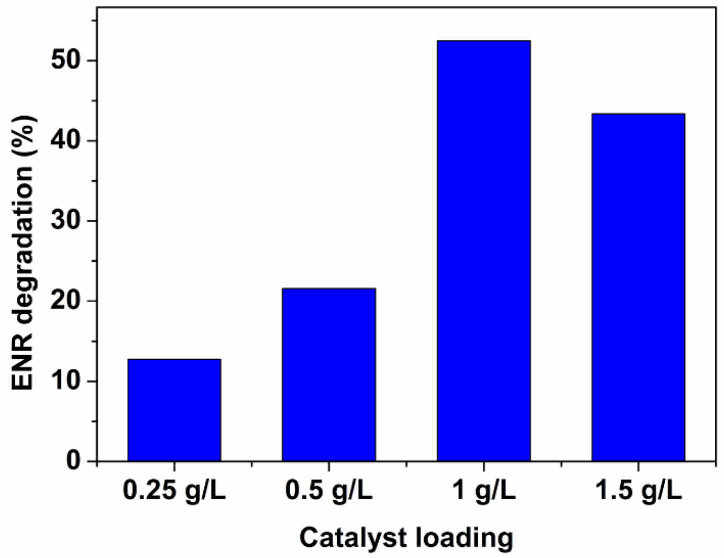

Figure 3.42. Effect of catalyst loadings on photodegradation of 20 mL ENR of 5 ppm, under LED blue light (0.2 A, 3.0 V) for 2h, 25^{o}C at pH 4.

Under the optimal conditions of solution pH and catalyst loading, the reaction rate of the photodegradation of ENR with other specific conditions was determined as shown in Figure 3.43 with the value of 0.007 min^{-1}. This rate constant was 10 times lower than that in the case of RhB photodegradation over the same catalyst and initial concentration, even under the used lamp power twice larger. This could be attributed to the nature itself of the colourless antibiotic along with the very limited adsorption onto the surface of the photocatalyst.

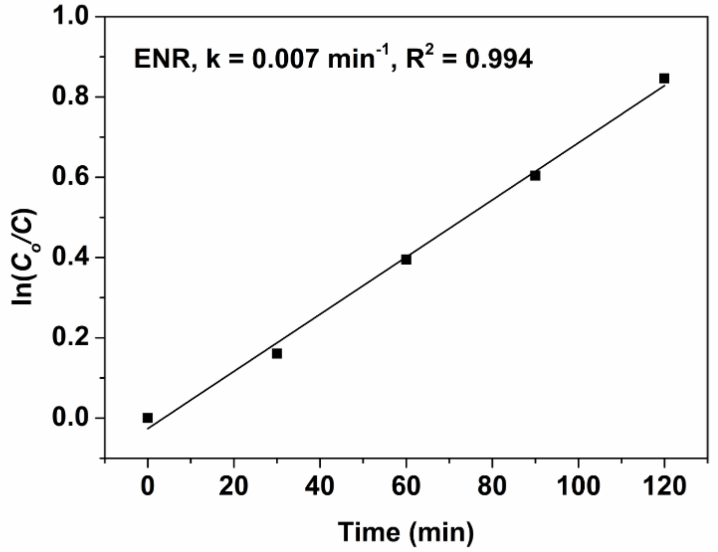

Figure 3.43. Kinetic curve of ENR degradation under LED blue light (0.2 A, 3.0 V) at pH 4, 25ºC, initial EFA concentration 5 ppm, catalyst loading 1 g.L^{-1} and solution volume of 20 mL.

The aim of the next part of this section is to evaluate the extent in which the ENR antibiotic being mineralized by MoS_2/g-C_3N_4 under blue LEDs. As shown in Figure 3.44 the changes of COD and concentration of the ENR solution after 4 hours of illumination are completely different. A reduction in COD of the solution for 8 hours of irradiation was also presented to explore more about the mineralization degree.

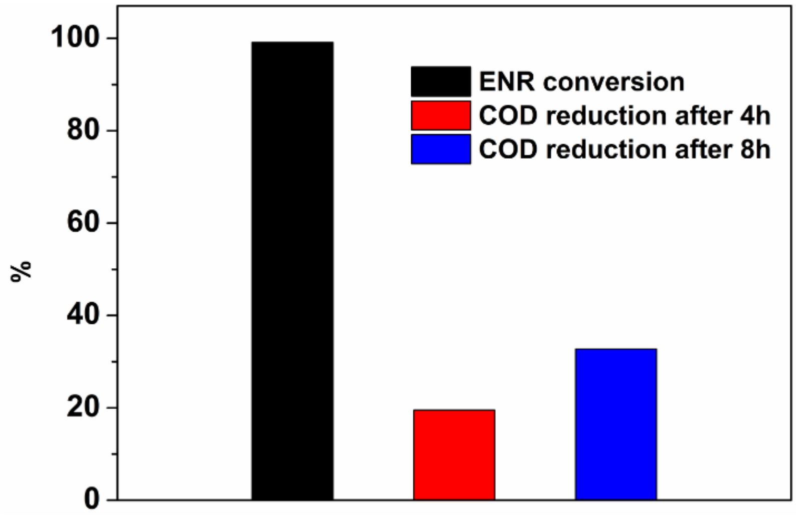

Figure 3.44. ENR conversion and COD reduction after 4 h of irradiation under LED blue light (0.2 A, 3.0 V), pH 4, initial concentration 5 ppm and volume of 20 mL, catalyst loading: 1 g.L^{-1}.

More specifically, while ENR in the solution was entirely degraded, its COD reduced only around 20% for the first 4 hours. This significant difference indicated that ENR itself could easily be totally degraded but not direct to simple molecules, instead it was partially oxidized to intermediates during the photocatalytic process. This point was also supported by the HPLC chromatogram of the ENR solution as shown in Figure 3.45. The peak at the retention time of 10.24 min which belongs to ENR completely disappeared after a 4-hour period of illumination under LED blue light, this is consistent with the above observation from UV-Vis measurement. All the formed intermediates with high relative abundance have higher molecular masses compared to that of ENR, which was confirmed by the corresponding mass spectra (see Appendix 2), implying that the ENR molecule under the given conditions was partially decomposed. This result also explained the low reduction of COD in comparison with ENR conversion as discussed previously.

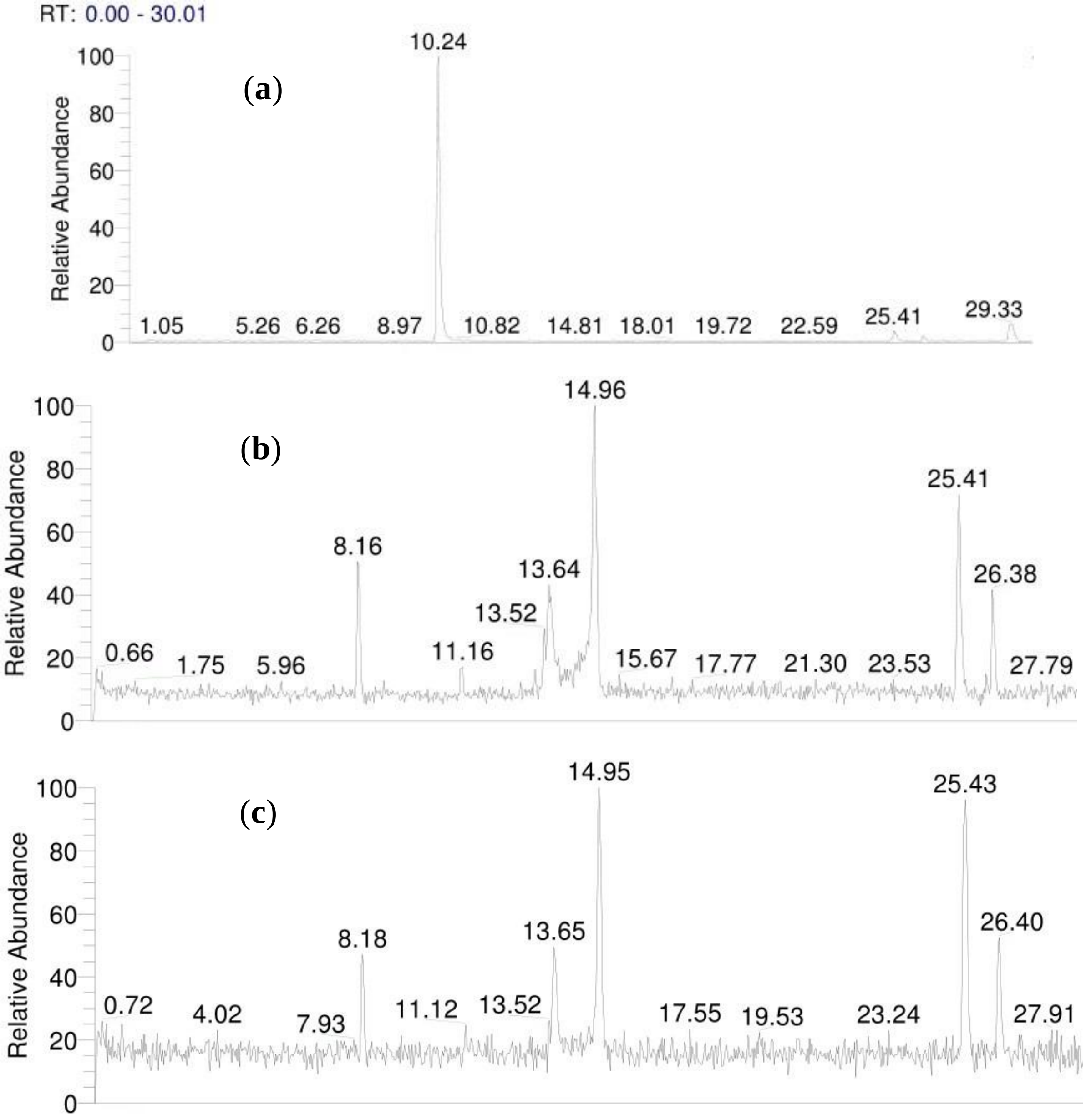

Figure 3.45. HPLC chromatogram of ENR solution after (a) 0h, (b) 4h and (c) 8h under LED blue light.

This was also brought up a new question, whether the formed intermediates become more toxic than the ENR itself to the environment or human health. To answer this tough but necessary question a toxicity test should be conducted [177], however, this test belongs to the biochemistry area, nevertheless that is still needed to investigate in the future research.

3.2.7.2. Designed-pilot evaluation

The recovery of the used catalyst for recycling is very important when employing a pilot in practical application. The methods that have been widely applied such as catalyst sedimentation [53], immobilization [145], using membrane [124], *etc*. The pilot in this work was designed to use the first one due to its simplicity. In order to apply this method efficiently, an increase in sedimentation rate plays an important role. To achieve this high rate, two widely used procedures, namely, adjusting pH of the suspension to the point of zero charge of the catalyst and electrolyte addition [53]. The first option was chosen with the result shown in Figure 3.46. It is obvious that at pH 3.5 the catalyst exhibited the fastest rate of settlement due to that value of pH closest to the pH_{pzc} (3.6) of the catalyst MCN1, resulting in a quick aggregation of uncharged particles, therefore the increase in the sedimentation rate.

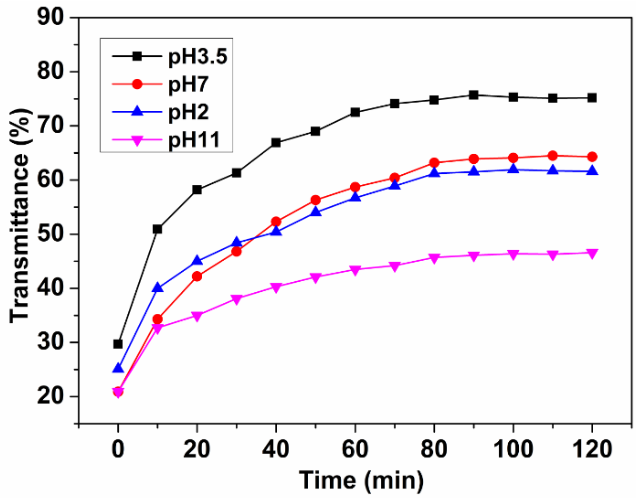

Figure 3.46. Transmittance of 800-nm electromagnetic wave through $MoS_2/g\text{-}C_3N_4$ suspension (0.7 $g.L^{-1}$) during the sedimentation process.

As shown in the above figure, the sedimentation occurred fast within the first 80 minutes of the process, then kept unchanged for the next 40 minutes. Based on this observation the recovery of catalyst when using the pilot after 1, 2 and

3 hours of sedimentation of the suspension at pH 3.5 was carried out, with result shown in Figure 3.47.

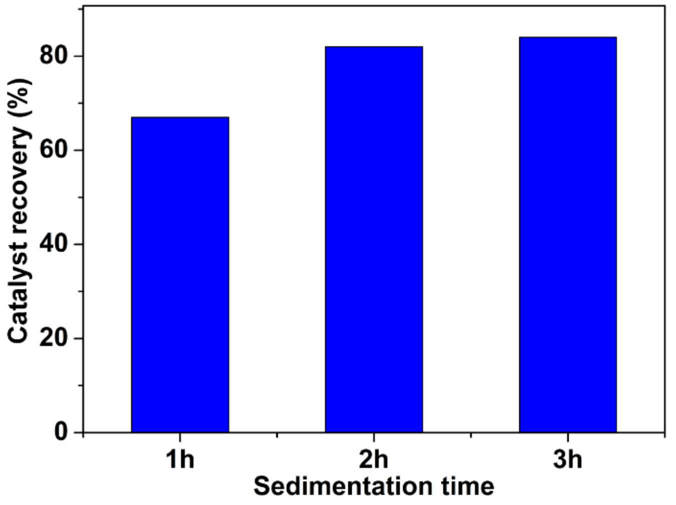

Figure 3.47. Percentage of catalyst recovery after different time of sedimentation of MoS_2/g-C_3N_4 catalyst (0.7 g.L^{-1}) suspension at pH 3.5.

The recovery reached nearly 80% after 2 hours of catalyst settlement, and almost remained unchanged for 1 hour more. Although the loss of catalyst was still high, however, this drawback could be acceptable due to the simple and low-cost process.

The photocatalytic activity of the recycled material was evaluated in the same conditions as for the first-use sample, the result was shown in Figure 3.48.

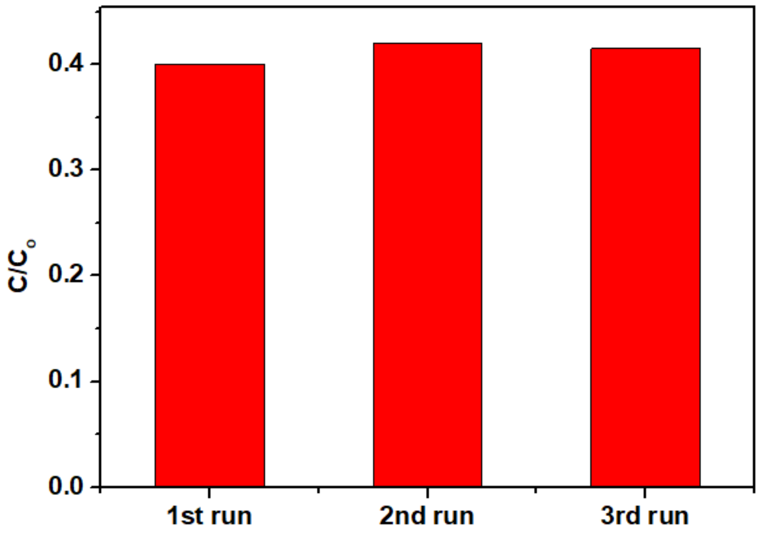

Figure 3.48. Recycling test for photocatalytic degradation of RhB over MCN1 sample. Conditions of process: irradiated volume: 25 mL, initial RhB concentration: 5.0 mg.L^{-1}, pH 3.0, catalyst loading: 0.7 g.L^{-1}, 25^{o}C, under blue light.

From the recycling test, it could be concluded that the material after the first use can perform its photocatalytic activity for the next uses with insignificant decrease.

To evaluate the throughput of the pilot RhB solution was used as simulated wastewater with the following conditions: 30 L of 5 ppm RhB solution at pH 3.5, MCN1 catalyst loading 0.7 g.L^{-1}, illuminated area 0.24 m^2 of 2 sets of blue LEDs (15 V, 5A), flow rate 8 L.min^{-1}. These conditions along with the distribution of wastewater as a thin layer which was previously proven good for the excitement of the catalyst also taken into account in the pilot design. Under these conditions, it took 120 h for that wastewater being completely treated, therefore the calculated pilot throughput was 1.0 L.h^{-1}.m^{-2}. It is obvious that this value is proportional to the illuminated area, the more the area of the solution being illuminated, the larger the volume of the solution can be treated per hour. That means the application of pilot can be feasible if the illuminated area is large enough to meet a particular requirement. Actually, the pilot itself is unlikely to apply directly to a specific situation. Nevertheless, it becomes useful when putting it in a complete system in which the pilot used as the last part before the treated water being discharged. Thus, the pilot is most suitable for the case of wastewater containing substances with low concentration that are not biodegradable. Instead of using electricity for the illumination, the sunlight can be applied effectively if the collector tilts a appropriate angle depending on the position where the pilot being placed.

CONCLUSIONS

This thesis has achieved some accomplishments are as follows:

1. The heterojunction WS_2/g-C_3N_4 composites was successfully constructed via a facile calcination directly from the precursors of tungstic acid and thiourea in the solid state. Weight ratio of WS_2 to g-C_3N_4 in the composites affects their photocatalytic activities. Among the composites, 7WCN (synthesized from H_2WO_4 and thiourea with the mass ratio 1:7) is the best material which could photodegrade 85.3% MB in 6 hours under visible light. A synergistic effect of components in heterojunction of the composites for enhancing photocatalytic performance was proposed. In addition, the MoS_2/g-C_3N_4 composites were also synthesized by a simple method from sodium molybdate and thiourea in solid state, without the need for hydrothermal-condition and ultrasound process steps. The synthesized composites were proven to be efficient and active in photocatalysis, especially the MCN1 (synthesized from heating the mixture of 0.06 gram MoS_2 and 24.0 grams of thiourea under N_2 gas) sample with the optimum MoS_2 content in which the interfacial charge transfer increased and thus reduced electron-hole recombination, improving the photocatalytic activity.

2. The adsorption step plays a crucial role in the whole photocatalytic process, the more the target molecules adsorb on the photocatalyst's surface the faster they would be photodegraded. However, too many the adsorbed molecules on the surface could lead to a negative effect on the overall photodegradation rate due to the lack of oxidizer on that surface such as oxygen. Furthermore, the mechanism of the transformation of target molecule such as rhodamine B to the intermediates such as rhodamine 110

was also proposed to provide a deep insight into the site of the molecule which was more likely to happen.

3. The reaction system used $MoS_2/g\text{-}C_3N_4$ photocatalyst and light-emitting diode (LED) was proven to have a value of new benchmark photochemical space-time yield (PSTY) of $8.3x10^{-3}$ $day^{-1}.kW^{-1}$, which was 100 times higher than that of the previous system also employed the same photocatalyst $MoS_2/g\text{-}C_3N_4$ over the same target molecule rhodamine B.

4. The designed photocatalytic pilot can operate automatically and use the prepared catalyst along with the application of natural sedimentation for recycling photocatalyst opens a new door to transfer the lab-scale into various practical applications including wastewater treatment under visible light.

LIST OF PUBLICATIONS

1. Huu Ha Tran, **Duy Huong Truong**, Thanh Tam Truong, Thi Xuan Dieu Nguyen, Ying-Shi Jin, Sung Jin Kim, and Vien Vo, "A Facile Synthesis of WS_2/g-C_3N_4 Composites with Improved Photocatalytic Activity," *Bull. Korean Chem. Soc.*, vol. 39, no. 8, pp. 965–971, 2018.
2. **D. H. Truong**, V. Vo, T. Van Gerven, and M. E. Leblebici, " A Facile Method for the Synthesis of a MoS_2 /g-C_3N_4 Photocatalyst ," *Chem. Eng. Technol.*, pp. 1–15, 2019.
3. Nguyễn Thị Thanh Bích, Nguyễn Đức Nhân, Huỳnh Hữu Điền, Nguyễn Tống Yến Như, Phạm Thị Yến Nhi, Nguyễn Văn Phúc, **Trương Duy Hướng**, Võ Viễn, "Effect of pH on Adsorption – Photocatalysis of Tunsten Disulfide", *Science Journal of Quy Nhon University*, 2020.
4. Trần Hữu Hà, Trần Doãn An, Nguyễn Văn Phúc, Nguyễn Thị Việt Nga, **Trương Duy Hướng**, Nguyễn Phi Hùng, Võ Viễn (2017), Tổng hợp và biến tính g-C_3N_4 bởi MS_2 (M = Mo, W) ứng dụng làm chất xúc tác quang, *Tạp chí Khoa học Trường Đại học Quy Nhơn*, tập 11, số 5/2017, tr 23-32.

REFERENCES

Tiếng Việt

1. Nguyễn Thị Việt Nga, Trần Hữu Hà, Võ Viễn (2017), "Nghiên cứu tổng hợp và hoạt tính xúc tác quang của vật liệu composit MoS_2/g-C_3N_4", *Tạp chí Xúc tác và Hấp phụ Việt Nam* 6(2), tr.115-119.
2. Quảng Thùy Trang, Trương Thị Mỹ Trúc, Sái Công Danh, Võ Viễn (2016), "Tổng hợp và tính chất xúc tác quang của vật liệu composit WS_2/g-C_3N_4", *Tạp chí Khoa học ĐHQGHN: Khoa học Tự nhiên và Công nghệ*, 32(4), tr.90-96.

Tiếng Anh

3. Akbal F. (2005), "Photocatalytic degradation of organic dyes in the presence of titanium dioxide under UV and solar light: effect of operational parameters", *Environmental Progress*, 24(3), pp. 317-322.
4. Akple M. S., Low J., Wageh S., Al-Ghamdi A. A., Yu J., Zhang J. (2015), "Enhanced visible light photocatalytic H_2-production of g-C_3N_4/WS_2 composite heterostructures", *Applied Surface Science*, 358, pp. 196-203.
5. Al-Ahmad A., Daschner F., Kümmerer K. (1999), "Biodegradability of cefotiam, ciprofloxacin, meropenem, penicillin G, and sulfamethoxazole and inhibition of waste water bacteria", *Archives of environmental contamination and toxicology*, 37(2), pp. 158-163.
6. Alshehri M., Al-Marzouki F., Alshehrie A., Hafez M. (2018), "Synthesis, characterization and band alignment characteristics of NiO/SnO_2 bulk heterojunction nanoarchitecture for promising photocatalysis applications", *Journal of Alloys and Compounds*, 757, pp. 161-168.
7. An G., Liu Y., Chai Y., Shang H., Liu C. (2006), "Synthesis, characterization and thermal decomposition mechanism of

cetyltrimethyl ammonium tetrathiotungstate", *Journal of Natural Gas Chemistry*, 15(2), pp. 127-133.

8. Anderson C., Bard A. J. (1997), "Improved photocatalytic activity and characterization of mixed TiO_2/SiO_2 and TiO_2/Al_2O_3 materials", *The Journal of Physical Chemistry B*, 101(14), pp. 2611-2616.
9. Asbury J. B., Hao E., Wang Y., Ghosh H. N., Lian T. (2001), Ultrafast electron transfer dynamics from molecular adsorbates to semiconductor nanocrystalline thin films, Editors, ACS Publications.
10. Ataca C., Topsakal M., Akturk E., Ciraci S. (2011), "A comparative study of lattice dynamics of three-and two-dimensional MoS_2", *The Journal of Physical Chemistry C*, 115(33), pp. 16354-16361.
11. Ayari A., Cobas E., Ogundadegbe O., Fuhrer M. S. (2007), "Realization and electrical characterization of ultrathin crystals of layered transition-metal dichalcogenides", *Journal of applied physics*, 101(1), p. 014507.
12. Benavente E., Santa Ana M., Mendizábal F., González G. (2002), "Intercalation chemistry of molybdenum disulfide", *Coordination chemistry reviews*, 224(1-2), pp. 87-109.
13. Berkdemir A., Gutiérrez H. R., Botello-Méndez A. R., Perea-López N., Elías A. L., Chia C.-I., Wang B., Crespi V. H., López-Urías F., Charlier J.-C. (2013), "Identification of individual and few layers of WS 2 using Raman Spectroscopy", *Scientific reports*, 3(1), pp. 1-8.
14. Bhandavat R., David L., Singh G. (2012), "Synthesis of surface-functionalized WS_2 nanosheets and performance as Li-ion battery anodes", *The journal of physical chemistry letters*, 3(11), pp. 1523-1530.
15. Bickley R., Slater M., Wang W.-J. (2005), "Engineering development of a photocatalytic reactor for waste water treatment", *Process Safety and Environmental Protection*, 83(3), pp. 205-216.

16. Bideau M., Claudel B., Dubien C., Faure L., Kazouan H. (1995), "On the “immobilization” of titanium dioxide in the photocatalytic oxidation of spent waters", *Journal of Photochemistry and Photobiology A: Chemistry*, 91(2), pp. 137-144.
17. Bora L. V., Mewada R. K. (2017), "Visible/solar light active photocatalysts for organic effluent treatment: Fundamentals, mechanisms and parametric review", *Renewable and Sustainable Energy Reviews*, 76, pp. 1393-1421.
18. Boyjoo Y., Ang M., Pareek V. (2014), "CFD simulation of a pilot scale slurry photocatalytic reactor and design of multiple-lamp reactors", *Chemical Engineering Science*, 111, pp. 266-277.
19. Brezova V., Jankovičová M., Soldan M., Blažková A., Rehakova M., Šurina I., Čeppan M., Havlinova B. (1994), "Photocatalytic degradation of p-toluenesulphonic acid in aqueous systems containing powdered and immobilized titanium dioxide", *Journal of Photochemistry and Photobiology A: Chemistry*, 83(1), pp. 69-75.
20. Byrne J., Eggins B., Brown N., Mckinney B., Rouse M. (1998), "Immobilisation of TiO_2 powder for the treatment of polluted water", *Applied Catalysis B: Environmental*, 17(1-2), pp. 25-36.
21. Cao S., Liu T., Hussain S., Zeng W., Peng X., Pan F. (2014), "Hydrothermal synthesis of variety low dimensional WS_2 nanostructures", *Materials Letters*, 129, pp. 205-208.
22. Cao Y., Li Q., Wang W. (2017), "Construction of a crossed-layer-structure MoS_2/g-C_3N_4 heterojunction with enhanced photocatalytic performance", *RSC advances*, 7(10), pp. 6131-6139.
23. Carp O., Huisman C. L., Reller A. (2004), "Photoinduced reactivity of titanium dioxide", *Progress in solid state chemistry*, 32(1-2), pp. 33-177.

24. Chatterjee D., Mahata A. (2002), "Visible light induced photodegradation of organic pollutants on dye adsorbed TiO_2 surface", *Journal of Photochemistry and Photobiology A: Chemistry*, 153(1-3), pp. 199-204.

25. Chen D., Ji G., Ding B., Ma Y., Qu B., Chen W., Lee J. Y. (2013), "In situ nitrogenated graphene–few-layer WS 2 composites for fast and reversible Li+ storage", *Nanoscale*, 5(17), pp. 7890-7896.

26. Chen D., Wang Z., Du Y., Yang G., Ren T., Ding H. (2015), "In situ ionic-liquid-assisted synthesis of plasmonic photocatalyst Ag/AgBr/g-C_3N_4 with enhanced visible-light photocatalytic activity", *Catalysis Today*, 258, pp. 41-48.

27. Chen D. H., Ye X., Li K. (2005), "Oxidation of PCE with a UV LED photocatalytic reactor", *Chemical Engineering & Technology: Industrial Chemistry-Plant Equipment-Process Engineering-Biotechnology*, 28(1), pp. 95-97.

28. Chen F., Li S., Chen Q., Zheng X., Liu P., Fang S. (2018), "3D graphene aerogels-supported Ag and Ag@ Ag_3PO_4 heterostructure for the efficient adsorption-photocatalysis capture of different dye pollutants in water", *Materials Research Bulletin*, 105, pp. 334-341.

29. Chen H.-W., Ku Y., Irawan A. (2007), "Photodecomposition of o-cresol by UV-LED/TiO_2 process with controlled periodic illumination", *Chemosphere*, 69(2), pp. 184-190.

30. Chen L., Toma F. M., Cooper J. K., Lyon A., Lin Y., Sharp I. D., Ager J. W. (2015), "Mo-doped $BiVO_4$ photoanodes synthesized by reactive sputtering", *ChemSusChem*, 8(6), pp. 1066-1071.

31. Chen M., Yao J., Huang Y., Gong H., Chu W. (2018), "Enhanced photocatalytic degradation of ciprofloxacin over $Bi_2O_3/(BiO)_2CO_3$

heterojunctions: efficiency, kinetics, pathways, mechanisms and toxicity evaluation", *Chemical Engineering Journal*, 334, pp. 453-461.

32. Chen X., Mao S. S. (2007), "Titanium dioxide nanomaterials: synthesis, properties, modifications, and applications", *Chemical reviews*, 107(7), pp. 2891-2959.

33. Cho I.-H., Zoh K.-D. (2007), "Photocatalytic degradation of azo dye (Reactive Red 120) in TiO_2/UV system: Optimization and modeling using a response surface methodology (RSM) based on the central composite design", *Dyes and Pigments*, 75(3), pp. 533-543.

34. Choi W., Choudhary N., Han G. H., Park J., Akinwande D., Lee Y. H. (2017), "Recent development of two-dimensional transition metal dichalcogenides and their applications", *Materials Today*, 20(3), pp. 116-130.

35. Chou S. S., Huang Y.-K., Kim J., Kaehr B., Foley B. M., Lu P., Dykstra C., Hopkins P. E., Brinker C. J., Huang J. (2015), "Controlling the metal to semiconductor transition of MoS_2 and WS_2 in solution", *Journal of the American Chemical Society*, 137(5), pp. 1742-1745.

36. Chung D. Y., Park S.-K., Chung Y.-H., Yu S.-H., Lim D.-H., Jung N., Ham H. C., Park H.-Y., Piao Y., Yoo S. J. (2014), "Edge-exposed MoS_2 nano-assembled structures as efficient electrocatalysts for hydrogen evolution reaction", *Nanoscale*, 6(4), pp. 2131-2136.

37. Coleman J. N., Lotya M., O'neill A., Bergin S. D., King P. J., Khan U., Young K., Gaucher A., De S., Smith R. J. (2011), "Two-dimensional nanosheets produced by liquid exfoliation of layered materials", *Science*, 331(6017), pp. 568-571.

38. Crowne F. J., Amani M., Birdwell A. G., Chin M. L., O'regan T. P., Najmaei S., Liu Z., Ajayan P. M., Lou J., Dubey M. (2013), "Blueshift

of the A-exciton peak in folded monolayer 1 H-MoS_2", *Physical Review B*, 88(23), p. 235302.

39. Czoska A., Livraghi S., Chiesa M., Giamello E., Agnoli S., Granozzi G., Finazzi E., Valentin C. D., Pacchioni G. (2008), "The nature of defects in fluorine-doped TiO_2", *The Journal of Physical Chemistry C*, 112(24), pp. 8951-8956.

40. Dai X.-J., Luo Y.-S., Zhang W.-D., Fu S.-Y. (2010), "Facile hydrothermal synthesis and photocatalytic activity of bismuth tungstate hierarchical hollow spheres with an ultrahigh surface area", *Dalton Transactions*, 39(14), pp. 3426-3432.

41. Daneshvar N., Behnajady M., Mohammadi M. K. A., Dorraji M. S. (2008), "UV/H_2O_2 treatment of Rhodamine B in aqueous solution: Influence of operational parameters and kinetic modeling", *Desalination*, 230(1-3), pp. 16-26.

42. Danion A., Disdier J., Guillard C., Païssé O., Jaffrezic-Renault N. (2006), "Photocatalytic degradation of imidazolinone fungicide in TiO_2-coated optical fiber reactor", *Applied Catalysis B: Environmental*, 62(3-4), pp. 274-281.

43. Di J., Xia J., Ge Y., Xu L., Xu H., Chen J., He M., Li H. (2014), "Facile fabrication and enhanced visible light photocatalytic activity of few-layer MoS_2 coupled BiOBr microspheres", *Dalton Transactions*, 43(41), pp. 15429-15438.

44. Di Paola A., Palmisano L., Venezia A., Augugliaro V. (1999), "Coupled semiconductor systems for photocatalysis. Preparation and characterization of polycrystalline mixed WO_3/WS_2 powders", *The Journal of Physical Chemistry B*, 103(39), pp. 8236-8244.

45. Ding J., Sun S., Bao J., Luo Z., Gao C. (2009), "Synthesis of $CaIn_2O_4$ rods and its photocatalytic performance under visible-light irradiation", *Catalysis letters*, 130(1-2), pp. 147-153.

46. Ding W., Hu L., Dai J., Tang X., Wei R., Sheng Z., Liang C., Shao D., Song W., Liu Q. (2019), "Highly ambient-stable 1T-MoS_2 and 1T-WS_2 by hydrothermal synthesis under high magnetic fields", *ACS nano*, 13(2), pp. 1694-1702.

47. Ding Y., Zhou Y., Nie W., Chen P. (2015), "MoS_2–GO nanocomposites synthesized via a hydrothermal hydrogel method for solar light photocatalytic degradation of methylene blue", *Applied Surface Science*, 357, pp. 1606-1612.

48. Dona J., Garriga C., Arana J., Pérez J., Colon G., Macías M., Navio J. (2007), "The effect of dosage on the photocatalytic degradation of organic pollutants", *Research on Chemical Intermediates*, 33(3-5), pp. 351-358.

49. Dong S., Feng J., Li Y., Hu L., Liu M., Wang Y., Pi Y., Sun J., Sun J. (2014), "Shape-controlled synthesis of $BiVO_4$ hierarchical structures with unique natural-sunlight-driven photocatalytic activity", *Applied Catalysis B: Environmental*, 152, pp. 413-424.

50. Doss N., Bernhardt P., Romero T., Masson R., Keller V., Keller N. (2014), "Photocatalytic degradation of butanone (methylethylketone) in a small-size TiO_2/β-SiC alveolar foam LED reactor", *Applied Catalysis B: Environmental*, 154, pp. 301-308.

51. Ebert I., Bachmann J., Kühnen U., Küster A., Kussatz C., Maletzki D., Schlüter C. (2011), "Toxicity of the fluoroquinolone antibiotics enrofloxacin and ciprofloxacin to photoautotrophic aquatic organisms", *Environmental Toxicology and Chemistry*, 30(12), pp. 2786-2792.

52. Emeline A. V., Kuznetsov V. N., Rybchuk V. K., Serpone N. (2008), "Visible-light-active titania photocatalysts: the case of N-doped s—properties and some fundamental issues", *International Journal of Photoenergy*, 2008.

53. Fernández-Ibánez P., Blanco J., Malato S., De Las Nieves F. (2003), "Application of the colloidal stability of TiO_2 particles for recovery and reuse in solar photocatalysis", *Water Research*, 37(13), pp. 3180-3188.

54. Fernandez A., Lassaletta G., Jimenez V., Justo A., Gonzalez-Elipe A., Herrmann J.-M., Tahiri H., Ait-Ichou Y. (1995), "Preparation and characterization of TiO_2 photocatalysts supported on various rigid supports (glass, quartz and stainless steel). Comparative studies of photocatalytic activity in water purification", *Applied Catalysis B: Environmental*, 7(1-2), pp. 49-63.

55. Frank S. N., Bard A. J. (1977), "Heterogeneous photocatalytic oxidation of cyanide and sulfite in aqueous solutions at semiconductor powders", *The journal of physical chemistry*, 81(15), pp. 1484-1488.

56. Fu J., Zhu B., Jiang C., Cheng B., You W., Yu J. (2017), "Hierarchical porous O-doped g-C3N4 with enhanced photocatalytic CO_2 reduction activity", *Small*, 13(15), p. 1603938.

57. Fu S., Liu X., Yan Y., Li L., Liu H., Zhao F., Zhou J. (2019), "Few-layer WS_2 modified BiOBr nanosheets with enhanced broad-spectrum photocatalytic activity towards various pollutants removal", *Science of The Total Environment*, 694, p. 133756.

58. Fu Y., Chang C., Chen P., Chu X., Zhu L. (2013), "Enhanced photocatalytic performance of boron doped Bi_2WO_6 nanosheets under simulated solar light irradiation", *Journal of hazardous materials*, 254, pp. 185-192.

59. Fujishima A., Honda K. (1972), "Electrochemical photolysis of water at a semiconductor electrode", *nature*, 238(5358), pp. 37-38.

60. Gaya U. I., Abdullah A. H. (2008), "Heterogeneous photocatalytic degradation of organic contaminants over titanium dioxide: a review of fundamentals, progress and problems", *Journal of photochemistry and photobiology C: Photochemistry reviews*, 9(1), pp. 1-12.

61. Ge L., Han C., Xiao X., Guo L. (2013), "Synthesis and characterization of composite visible light active photocatalysts MoS_2–g-C_3N_4 with enhanced hydrogen evolution activity", *International journal of hydrogen energy*, 38(17), pp. 6960-6969.

62. Gelover S., Mondragón P., Jiménez A. (2004), "Titanium dioxide sol–gel deposited over glass and its application as a photocatalyst for water decontamination", *Journal of Photochemistry and Photobiology A: Chemistry*, 165(1-3), pp. 241-246.

63. Ghosh J. P., Langford C. H., Achari G. (2008), "Characterization of an LED based photoreactor to degrade 4-chlorophenol in an aqueous medium using coumarin (C-343) sensitized TiO_2", *The Journal of Physical Chemistry A*, 112(41), pp. 10310-10314.

64. Gnanamoorthy G., Yadav V. K., Latha D., Karthikeyan V., Narayanan V. (2020), "Enhanced photocatalytic performance of $ZnSnO_3$/rGO nanocomposite", *Chemical Physics Letters*, 739, p. 137050.

65. Guardia L., Paredes J. I., Munuera J. M., Villar-Rodil S., AyáN-Varela M., Martínez-Alonso A., TascóN J. M. (2014), "Chemically exfoliated MoS_2 nanosheets as an efficient catalyst for reduction reactions in the aqueous phase", *ACS applied materials & interfaces*, 6(23), pp. 21702-21710.

66. Guo F., Shi W., Lin X., Yan X., Guo Y., Che G. (2015), "Novel $BiVO_4/InVO_4$ heterojunctions: facile synthesis and efficient visible-light photocatalytic performance for the degradation of rhodamine B", *Separation and Purification Technology*, 141, pp. 246-255.
67. Guo X., Cao G.-L., Ding F., Li X., Zhen S., Xue Y.-F., Yan Y.-M., Liu T., Sun K.-N. (2015), "A bulky and flexible electrocatalyst for efficient hydrogen evolution based on the growth of MoS_2 nanoparticles on carbon nanofiber foam", *Journal of Materials Chemistry A*, 3(9), pp. 5041-5046.
68. Guo Y., Zhao J., Zhang H., Yang S., Qi J., Wang Z., Xu H. (2005), "Use of rice husk-based porous carbon for adsorption of Rhodamine B from aqueous solutions", *Dyes and Pigments*, 66(2), pp. 123-128.
69. Gupta A., Arunachalam V., Vasudevan S. (2016), "Liquid-phase exfoliation of MoS_2 nanosheets: the critical role of trace water", *The journal of physical chemistry letters*, 7(23), pp. 4884-4890.
70. Hang N. T., Zhang S., Yang W. (2017), "Efficient exfoliation of g-C_3N_4 and NO_2 sensing behavior of graphene/g-C_3N_4 nanocomposite", *Sensors and Actuators B: Chemical*, 248, pp. 940-948.
71. Hasegawa K., Ito T., Maeda M., Kagaya S. (2001), "A TiO_2-suspended continuous flow photoreactor system combined with the separation of TiO_2 particles by coagulation for the photocatalytic degradation of dibutyl phthalate", *Chemistry letters*, 30(9), pp. 890-891.
72. Hassanpour M., Safardoust-Hojaghan H., Salavati-Niasari M. (2017), "Degradation of methylene blue and Rhodamine B as water pollutants via green synthesized Co_3O_4/ZnO nanocomposite", *Journal of Molecular Liquids*, 229, pp. 293-299.

73. He Y., Zhang L., Teng B., Fan M. (2015), "New application of Z-scheme Ag_3PO_4/g-C_3N_4 composite in converting CO_2 to fuel", *Environmental science & technology*, 49(1), pp. 649-656.

74. He Z., Que W. (2016), "Molybdenum disulfide nanomaterials: Structures, properties, synthesis and recent progress on hydrogen evolution reaction", *Applied Materials Today*, 3, pp. 23-56.

75. Ho W., Yu J. C., Lin J., Yu J., Li P. (2004), "Preparation and photocatalytic behavior of MoS_2 and WS_2 nanocluster sensitized TiO_2", *Langmuir*, 20(14), pp. 5865-5869.

76. Homem V., Santos L. (2011), "Degradation and removal methods of antibiotics from aqueous matrices–a review", *Journal of environmental management*, 92(10), pp. 2304-2347.

77. Hong J., Chen C., Bedoya F. E., Kelsall G. H., O'hare D., Petit C. (2016), "Carbon nitride nanosheet/metal–organic framework nanocomposites with synergistic photocatalytic activities", *Catalysis Science & Technology*, 6(13), pp. 5042-5051.

78. Hou Y., Zhu Y., Xu Y., Wang X. (2014), "Photocatalytic hydrogen production over carbon nitride loaded with WS_2 as cocatalyst under visible light", *Applied Catalysis B: Environmental*, 156, pp. 122-127.

79. Hu K., Meng M. (2013), "Degradation of malachite green on MoS_2/TiO_2 nanocomposite", *Asian Journal of Chemistry*, 25(10), pp. 5827-5829.

80. Huang H., Feng Y., Zhou J., Li G., Dai K. (2013), "Visible light photocatalytic reduction of Cr (VI) on Ag_3PO_4 nanoparticles", *Desalination and water treatment*, 51(37-39), pp. 7236-7240.

81. Jamali A., Vanraes R., Hanselaer P., Van Gerven T. (2013), "A batch LED reactor for the photocatalytic degradation of phenol", *Chemical Engineering and Processing: Process Intensification*, 71, pp. 43-50.

82. Jiang J., Ou-Yang L., Zhu L., Zheng A., Zou J., Yi X., Tang H. (2014), "Dependence of electronic structure of g-C_3N_4 on the layer number of its nanosheets: a study by Raman spectroscopy coupled with first-principles calculations", *Carbon*, 80, pp. 213-221.

83. Jo W.-K., Lee J. Y., Selvam N. C. S. (2016), "Synthesis of MoS_2 nanosheets loaded ZnO–g-C_3N_4 nanocomposites for enhanced photocatalytic applications", *Chemical Engineering Journal*, 289, pp. 306-318.

84. Jo W.-K., Tayade R. J. (2014), "New generation energy-efficient light source for photocatalysis: LEDs for environmental applications", *Industrial & Engineering Chemistry Research*, 53(6), pp. 2073-2084.

85. Johnson B. (2003), "High-power, short-wave LED purifies air", Editors, *Laurin publ co inc berkshire common po box 1146, pittsfield, MA 01202 USA.*

86. Junqi L., Zhanyun G., Yu W., Zhenfeng Z. (2014), "Three-dimensional TiO_2/Bi_2WO_6 hierarchical heterostructure with enhanced visible photocatalytic activity", *Micro & Nano Letters*, 9(2), pp. 65-68.

87. Kagaya S., Shimizu K., Arai R., Hasegawa K. (1999), "Separation of titanium dioxide photocatalyst in its aqueous suspensions by coagulation with basic aluminium chloride", *Water Research*, 33(7), pp. 1753-1755.

88. Kaur K., Badru R., Singh P. P., Kaushal S. (2020), "Photodegradation of organic pollutants using heterojunctions: A review", *Journal of Environmental Chemical Engineering*, 8(2), p. 103666.

89. Kaur M., Umar A., Mehta S. K., Singh S., Kansal S. K., Fouad H., Alothman O. Y. (2018), "Rapid solar-light driven superior photocatalytic degradation of methylene blue using MoS_2-ZnO heterostructure nanorods photocatalyst", *Materials*, 11(11), p. 2254.

90. Kočí K., Reli M., Troppová I., Šihor M., Kupková J., Kustrowski P., Praus P. (2017), "Photocatalytic decomposition of N_2O over TiO_2/g-C_3N_4 photocatalysts heterojunction", *Applied Surface Science*, 396, pp. 1685-1695.

91. Komatsu T. (2001), "The first synthesis and characterization of cyameluric high polymers", *Macromolecular Chemistry and Physics*, 202(1), pp. 19-25.

92. Kong J.-Z., Li A.-D., Li X.-Y., Zhai H.-F., Zhang W.-Q., Gong Y.-P., Li H., Wu D. (2010), "Photo-degradation of methylene blue using Ta-doped ZnO nanoparticle", *Journal of solid state chemistry*, 183(6), pp. 1359-1364.

93. Kuc A., Zibouche N., Heine T. (2011), "Influence of quantum confinement on the electronic structure of the transition metal sulfide TS_2", *Physical Review B*, 83(24), p. 245213.

94. Kumar A., Pandey G. (2017), "A review on the factors affecting the photocatalytic degradation of hazardous materials", *Mater. Sci. Eng. Int. J*, 1(3), pp. 1-10.

95. Kumar S., Sharma V., Bhattacharyya K., Krishnan V. (2016), "Synergetic effect of MoS_2–RGO doping to enhance the photocatalytic performance of ZnO nanoparticles", *New Journal of Chemistry*, 40(6), pp. 5185-5197.

96. Leblebici M. E. (2017), "Design, Modelling and Benchmarking of Photoreactors and Separation Processes for Waste Treatment and Purification".

97. Leblebici M. E., Rongé J., Martens J. A., Stefanidis G. D., Van Gerven T. (2015), "Computational modelling of a photocatalytic UV-LED

reactor with internal mass and photon transfer consideration", *Chemical Engineering Journal*, 264, pp. 962-970.

98. Leblebici M. E., Stefanidis G. D., Van Gerven T. (2015), "Comparison of photocatalytic space-time yields of 12 reactor designs for wastewater treatment", *Chemical Engineering and Processing: Process Intensification*, 97, pp. 106-111.
99. Lee K. M., Lai C. W., Ngai K. S., Juan J. C. (2016), "Recent developments of zinc oxide based photocatalyst in water treatment technology: a review", *Water research*, 88, pp. 428-448.
100. Lee M., Yong K. (2012), "Highly efficient visible light photocatalysis of novel CuS/ZnO heterostructure nanowire arrays", *Nanotechnology*, 23(19), p. 194014.
101. Li H., Wu J., Yin Z., Zhang H. (2014), "Preparation and applications of mechanically exfoliated single-layer and multilayer MoS_2 and WSe_2 nanosheets", *Accounts of chemical research*, 47(4), pp. 1067-1075.
102. Li H., Yin Z., He Q., Li H., Huang X., Lu G., Fam D. W. H., Tok A. I. Y., Zhang Q., Zhang H. (2012), "Fabrication of single-and multilayer MoS_2 film-based field-effect transistors for sensing NO at room temperature", *small*, 8(1), pp. 63-67.
103. Li J., Liu E., Ma Y., Hu X., Wan J., Sun L., Fan J. (2016), "Synthesis of MoS_2/g-C_3N_4 nanosheets as 2D heterojunction photocatalysts with enhanced visible light activity", *Applied Surface Science*, 364, pp. 694-702.
104. Li J., Liu X., Pan L., Qin W., Chen T., Sun Z. (2014), "MoS_2–reduced graphene oxide composites synthesized via a microwave-assisted method for visible-light photocatalytic degradation of methylene blue", *Rsc Advances*, 4(19), pp. 9647-9651.

105. Li Puma G., Yue P. L. (2001), "A novel fountain photocatalytic reactor for water treatment and purification: modeling and design", *Industrial & engineering chemistry research*, 40(23), pp. 5162-5169.

106. Li Q., Bian J., Zhang L., Zhang R., Wang G., Ng D. H. (2014), "Synthesis of Carbon Materials–TiO_2 Hybrid Nanostructures and Their Visible-Light Photo-catalytic Activity", *ChemPlusChem*, 79(3), pp. 454-461.

107. Li Q., Zhang N., Yang Y., Wang G., Ng D. H. (2014), "High efficiency photocatalysis for pollutant degradation with MoS_2/C_3N_4 heterostructures", *Langmuir*, 30(29), pp. 8965-8972.

108. Li X., Cheng Y., Kang S., Mu J. (2010), "Preparation and enhanced visible light-driven catalytic activity of ZnO microrods sensitized by porphyrin heteroaggregate", *Applied surface science*, 256(22), pp. 6705-6709.

109. Li X., Zhao Y. (1999), "Advanced treatment of dyeing wastewater for reuse", *Water Science and Technology*, 39(10-11), pp. 249-255.

110. Li Z., Fang Y., Zhan X., Xu S. (2013), "Facile preparation of squarylium dye sensitized TiO_2 nanoparticles and their enhanced visible-light photocatalytic activity", *Journal of alloys and compounds*, 564, pp. 138-142.

111. Li Z., Meng X., Zhang Z. (2018), "Recent development on MoS_2-based photocatalysis: A review", *Journal of Photochemistry and Photobiology C: Photochemistry Reviews*, 35, pp. 39-55.

112. Liang D., Jing T., Ma Y., Hao J., Sun G., Deng M. (2016), "Photocatalytic properties of $g\text{-}C_6N_6/g\text{-}C_3N_4$ heterostructure: a theoretical study", *The Journal of Physical Chemistry C*, 120(42), pp. 24023-24029.

113. Lin H., Wang J., Luo Q., Peng H., Luo C., Qi R., Huang R., Travas-Sejdic J., Duan C.-G. (2017), "Rapid and highly efficient chemical exfoliation of layered MoS_2 and WS_2", *Journal of Alloys and Compounds*, 699, pp. 222-229.

114. Liu H., Liang J., Du J., Gao Q., Fu S., Li L., Hu M., Zhao F., Zhou J. (2020), "Promoting charge separation in dual defect mediated Z-scheme MoS_2/g-C_3N_4 photocatalysts for enhanced photocatalytic degradation activity: synergistic effect insight", *Colloids and Surfaces A: Physicochemical and Engineering Aspects*, p. 124668.

115. Liu N., Kim P., Kim J. H., Ye J. H., Kim S., Lee C. J. (2014), "Large-area atomically thin MoS2 nanosheets prepared using electrochemical exfoliation", *ACS nano*, 8(7), pp. 6902-6910.

116. Lu H., Xu L., Wei B., Zhang M., Gao H., Sun W. (2014), "Enhanced photosensitization process induced by the p–n junction of $Bi_2O_2CO_3$/BiOCl heterojunctions on the degradation of rhodamine B", *Applied surface science*, 303, pp. 360-366.

117. Luo Y., Wei X., Gao B., Zou W., Zheng Y., Yang Y., Zhang Y., Tong Q., Dong L. (2019), "Synergistic adsorption-photocatalysis processes of graphitic carbon nitrate (g-C_3N_4) for contaminant removal: Kinetics, models, and mechanisms", *Chemical Engineering Journal*, 375, p. 122019.

118. Lyu J., Hu Z., Li Z., Ge M. (2019), "Removal of tetracycline by BiOBr microspheres with oxygen vacancies: Combination of adsorption and photocatalysis", *Journal of Physics and Chemistry of Solids*, 129, pp. 61-70.

119. Mahler B., Hoepfner V., Liao K., Ozin G. A. (2014), "Colloidal synthesis of 1T-WS_2 and 2H-WS_2 nanosheets: applications for photocatalytic

hydrogen evolution", *Journal of the American Chemical Society*, 136(40), pp. 14121-14127.

120. Mak K. F., Lee C., Hone J., Shan J., Heinz T. F. (2010), "Atomically thin MoS 2: a new direct-gap semiconductor", *Physical review letters*, 105(13), p. 136805.
121. Makama A., Salmiaton A., Saion E., Choong T., Abdullah N. (2015), "Microwave-assisted synthesis of porous ZnO/SnS_2 heterojunction and its enhanced photoactivity for water purification", *Journal of Nanomaterials*, 2015.
122. Matos J., Laine J., Herrmann J.-M., Uzcategui D., Brito J. (2007), "Influence of activated carbon upon titania on aqueous photocatalytic consecutive runs of phenol photodegradation", *Applied Catalysis B: Environmental*, 70(1-4), pp. 461-469.
123. Merka O., Yarovyi V., Bahnemann D. W., Wark M. (2011), "pH-control of the photocatalytic degradation mechanism of rhodamine B over $Pb_3Nb_4O_{13}$", *The Journal of Physical Chemistry C*, 115(16), pp. 8014-8023.
124. Molinari R., Mungari M., Drioli E., Di Paola A., Loddo V., Palmisano L., Schiavello M. (2000), "Study on a photocatalytic membrane reactor for water purification", *Catalysis Today*, 55(1-2), pp. 71-78.
125. Monga D., Ilager D., Shetti N. P., Basu S., Aminabhavi T. M. (2020), "2D/2D heterojunction of MoS_2/g-C_3N_4 nanoflowers for enhanced visible-light-driven photocatalytic and electrochemical degradation of organic pollutants", *Journal of Environmental Management*, 274, p. 111208.
126. Mu C., Zhang Y., Cui W., Liang Y., Zhu Y. (2017), "Removal of bisphenol A over a separation free 3D Ag_3PO_4-graphene hydrogel via an

adsorption-photocatalysis synergy", *Applied Catalysis B: Environmental*, 212, pp. 41-49.

127. Nagaveni K., Hegde M., Ravishankar N., Subbanna G., Madras G. (2004), "Synthesis and structure of nanocrystalline TiO_2 with lower band gap showing high photocatalytic activity", *Langmuir*, 20(7), pp. 2900-2907.

128. Nahar M. S., Hasegawa K., Kagaya S. (2006), "Photocatalytic degradation of phenol by visible light-responsive iron-doped TiO2 and spontaneous sedimentation of the TiO_2 particles", *Chemosphere*, 65(11), pp. 1976-1982.

129. Nakano K., Obuchi E., Takagi S., Yamamoto R., Tanizaki T., Taketomi M., Eguchi M., Ichida K., Suzuki M., Hashimoto A. (2004), "Photocatalytic treatment of water containing dinitrophenol and city water over TiO_2/SiO_2", *Separation and purification technology*, 34(1-3), pp. 67-72.

130. Natarajan T. S., Thomas M., Natarajan K., Bajaj H. C., Tayade R. J. (2011), "Study on UV-LED/TiO_2 process for degradation of Rhodamine B dye", *Chemical Engineering Journal*, 169(1-3), pp. 126-134.

131. Paradisanos I., Germanis S., Pelekanos N., Fotakis C., Kymakis E., Kioseoglou G., Stratakis E. (2017), "Room temperature observation of biexcitons in exfoliated WS_2 monolayers", *Applied Physics Letters*, 110(19), p. 193102.

132. Pelaez M., Nolan N. T., Pillai S. C., Seery M. K., Falaras P., Kontos A. G., Dunlop P. S., Hamilton J. W., Byrne J. A., O'shea K. (2012), "A review on the visible light active titanium dioxide photocatalysts for environmental applications", *Applied Catalysis B: Environmental*, 125, pp. 331-349.

133. Peng W.-C., Li X.-Y. (2014), "Synthesis of MoS_2/g-C_3N_4 as a solar light-responsive photocatalyst for organic degradation", *Catalysis Communications*, 49, pp. 63-67.

134. Pirhashemi M., Habibi-Yangjeh A. (2016), "Novel ZnO/Ag_2CrO_4 nanocomposites with n–n heterojunctions as excellent photocatalysts for degradation of different pollutants under visible light", *Journal of Materials Science: Materials in Electronics*, 27(4), pp. 4098-4108.

135. Plechinger G., Nagler P., Kraus J., Paradiso N., Strunk C., Schüller C., Korn T. (2015), "Identification of excitons, trions and biexcitons in single-layer WS_2", *physica status solidi (RRL)–Rapid Research Letters*, 9(8), pp. 457-461.

136. Pouretedal H., Kadkhodaie A. (2010), "Synthetic CeO_2 nanoparticle catalysis of methylene blue photodegradation: kinetics and mechanism", *Chin. J. Catal*, 31(11-12), pp. 1328-1334.

137. Presciutti A., Asdrubali F., Marrocchi A., Broggi A., Pizzoli G., Damiani A. (2014), "Sun simulators: Development of an innovative low cost film filter", *Sustainability*, 6(10), pp. 6830-6846.

138. Radisavljevic B., Radenovic A., Brivio J., Giacometti V., Kis A. (2011), "Single-layer MoS_2 transistors", *Nature nanotechnology*, 6(3), pp. 147-150.

139. Ranjit K., Willner I., Bossmann S., Braun A. (2001), "Lanthanide oxide-doped titanium dioxide photocatalysts: novel photocatalysts for the enhanced degradation of p-chlorophenoxyacetic acid", *Environmental science & technology*, 35(7), pp. 1544-1549.

140. Ray A. K. (1999), "Design, modelling and experimentation of a new large-scale photocatalytic reactor for water treatment", *Chemical Engineering Science*, 54(15-16), pp. 3113-3125.

141. Royaee S. J., Sohrabi M., Soleymani F. (2011), "Performance of a photo-impinging streams reactor for the phenol degradation process", *Journal of Chemical Technology & Biotechnology*, 86(2), pp. 205-212.

142. Sang Y., Zhao Z., Zhao M., Hao P., Leng Y., Liu H. (2015), "From UV to near-infrared, WS_2 nanosheet: a novel photocatalyst for full solar light spectrum photodegradation", *Advanced Materials*, 27(2), pp. 363-369.

143. Seifrtov á M., Pena A., Lino C., Solich P. (2008), "Determination of fluoroquinolone antibiotics in hospital and municipal wastewaters in Coimbra by liquid chromatography with a monolithic column and fluorescence detection", *Analytical and bioanalytical chemistry*, 391(3), pp. 799-805.

144. Senthilkumaar S., Porkodi K., Gomathi R., Manonmani N. (2006), "Sol–gel derived silver doped nanocrystalline titania catalysed photodegradation of methylene blue from aqueous solution", *Dyes and Pigments*, 69(1-2), pp. 22-30.

145. Shan A. Y., Ghazi T. I. M., Rashid S. A. (2010), "Immobilisation of titanium dioxide onto supporting materials in heterogeneous photocatalysis: a review", *Applied Catalysis A: General*, 389(1-2), pp. 1-8.

146. Shang J., Hao W., Lv X., Wang T., Wang X., Du Y., Dou S., Xie T., Wang D., Wang J. (2014), "Bismuth oxybromide with reasonable photocatalytic reduction activity under visible light", *ACS Catalysis*, 4(3), pp. 954-961.

147. Sharma P., Sasson Y. (2017), "A photoactive catalyst Ru–gC_3N_4 for hydrogen transfer reaction of aldehydes and ketones", *Green Chemistry*, 19(3), pp. 844-852.

148. Shen Y.-H. (1998), "Colloidal titanium dioxide separation from water by foam flotation".

149. Sheng Y., Wei Z., Miao H., Yao W., Li H., Zhu Y. (2019), "Enhanced organic pollutant photodegradation via adsorption/photocatalysis synergy using a 3D g-C_3N_4/TiO_2 free-separation photocatalyst", *Chemical Engineering Journal*, 370, pp. 287-294.

150. Shi L., Liang L., Wang F., Liu M., Sun J. (2015), "Enhanced Photocatalytic Activity of Degrading Rhodamine B Over MoS_2/g-C_3N_4 Photocatalyst Under Visible Light", *Energy and Environment Focus*, 4(2), pp. 74-81.

151. Shi Z., Zhang Y., Duoerkun G., Cao W., Liu T., Zhang L., Liu J., Li M., Chen Z. (2020), "Fabrication of MoS_2/BiOBr heterojunctions on carbon fibers as a weaveable photocatalyst for tetracycline hydrochloride degradation and Cr(VI) reduction under visible light", *Environmental Science: Nano*.

152. Shironita S., Mori K., Shimizu T., Ohmichi T., Mimura N., Yamashita H. (2008), "Preparation of nano-sized platinum metal catalyst using photo-assisted deposition method on mesoporous silica including single-site photocatalyst", *Applied surface science*, 254(23), pp. 7604-7607.

153. Sivakumar S., Selvaraj A., Ramasamy A. K., Balasubramanian V. (2013), "Enhanced photocatalytic degradation of reactive dyes over $FeTiO_3/TiO_2$ heterojunction in the presence of H_2O_2", *Water, Air, & Soil Pollution*, 224(5), p. 1529.

154. So C., Cheng M. Y., Yu J., Wong P. (2002), "Degradation of azo dye Procion Red MX-5B by photocatalytic oxidation", *Chemosphere*, 46(6), pp. 905-912.

155. Soltani T., Tayyebi A., Lee B.-K. (2018), "Efficient promotion of charge separation with reduced graphene oxide (rGO) in $BiVO_4$/rGO photoanode for greatly enhanced photoelectrochemical water splitting", *Solar Energy Materials and Solar Cells*, 185, pp. 325-332.

156. Song B., Wang Q., Wang L., Lin J., Wei X., Murugadoss V., Wu S., Guo Z., Ding T., Wei S. (2020), "Carbon nitride nanoplatelet photocatalysts heterostructured with B-doped carbon nanodots for enhanced photodegradation of organic Pollutants", *Journal of colloid and interface science*, 559, pp. 124-133.

157. Subramanian M., Kannan A. (2010), "Photocatalytic degradation of phenol in a rotating annular reactor", *Chemical engineering science*, 65(9), pp. 2727-2740.

158. Sun S., Wu Y., Zhang X., Zhang Z., Yan Y., Guan W. (2014), "Enhanced visible-light-driven photocatalytic degradation performance of cip on $BiVO_4$–Bi_2WO_6 nano-heterojunction photocatalysts", *Nano*, 9(02), p. 1450015.

159. Sun Y., Wang W., Zhang L., Sun S. (2013), "The photocatalysis of Bi_2MoO_6 under the irradiation of blue LED", *Materials Research Bulletin*, 48(10), pp. 4357-4361.

160. Surolia P. K., Tayade R. J., Jasra R. V. (2007), "Effect of anions on the photocatalytic activity of Fe(III) salts impregnated TiO_2", *Industrial & engineering chemistry research*, 46(19), pp. 6196-6203.

161. Suzuki Y., Maezawa A., Uchida S. (2000), "Liquid-solid separation of photo-catalyst suspension induced by ultrasound", *Chemistry Letters*, 29(2), pp. 130-131.

162. Tacchini I., Terrado E., Anson A., Martinez M. (2011), "Preparation of a TiO_2–MoS_2 nanoparticle-based composite by solvothermal method

with enhanced photoactivity for the degradation of organic molecules in water under UV light", *Micro & Nano Letters*, 6(11), pp. 932-936.

163. Tayade R. J., Kulkarni R. G., Jasra R. V. (2006), "Transition metal ion impregnated mesoporous TiO_2 for photocatalytic degradation of organic contaminants in water", *Industrial & engineering chemistry research*, 45(15), pp. 5231-5238.
164. Tayade R. J., Natarajan T. S., Bajaj H. C. (2009), "Photocatalytic degradation of methylene blue dye using ultraviolet light emitting diodes", *Industrial & Engineering Chemistry Research*, 48(23), pp. 10262-10267.
165. Tayade R. J., Surolia P. K., Kulkarni R. G., Jasra R. V. (2007), "Photocatalytic degradation of dyes and organic contaminants in water using nanocrystalline anatase and rutile TiO_2", *Science and Technology of Advanced Materials*, 8(6), p. 455.
166. Thripuranthaka M., Kashid R. V., Sekhar Rout C., Late D. J. (2014), "Temperature dependent Raman spectroscopy of chemically derived few layer MoS_2 and WS_2 nanosheets", *Applied Physics Letters*, 104(8), p. 081911.
167. Tian Y., Ge L., Wang K., Chai Y. (2014), "Synthesis of novel MoS_2/g-C_3N_4 heterojunction photocatalysts with enhanced hydrogen evolution activity", *Materials characterization*, 87, pp. 70-73.
168. Tongay S., Fan W., Kang J., Park J., Koldemir U., Suh J., Narang D. S., Liu K., Ji J., Li J. (2014), "Tuning interlayer coupling in large-area heterostructures with CVD-grown MoS_2 and WS_2 monolayers", *Nano letters*, 14(6), pp. 3185-3190.

169. Umebayashi T., Yamaki T., Itoh H., Asai K. (2002), "Band gap narrowing of titanium dioxide by sulfur doping", *Applied Physics Letters*, 81(3), pp. 454-456.

170. Vattikuti S., Byon C. (2015), "Synthesis and characterization of molybdenum disulfide nanoflowers and nanosheets: nanotribology", *Journal of Nanomaterials*, 2015.

171. Vattikuti S. P., Ngo I.-L., Byon C. (2016), "Physicochemcial characteristic of CdS-anchored porous WS_2 hybrid in the photocatalytic degradation of crystal violet under UV and visible light irradiation", *Solid State Sciences*, 61, pp. 121-130.

172. Velmurugan R., Krishnakumar B., Swaminathan M. (2014), "Synthesis of Pd co-doped nano-TiO_2–SO_4^{2-} and its synergetic effect on the solar photodegradation of Reactive Red 120 dye", *Materials science in semiconductor processing*, 25, pp. 163-172.

173. Velmurugan R., Sreedhar B., Swaminathan M. (2011), "Nanostructured AgBr loaded TiO_2: an efficient sunlight active photocatalyst for degradation of reactive Red 120", *Chemistry Central Journal*, 5(1), p. 46.

174. Vezzoli M., Martens W. N., Bell J. M. (2011), "Investigation of phenol degradation: True reaction kinetics on fixed film titanium dioxide photocatalyst", *Applied Catalysis A: General*, 404(1-2), pp. 155-163.

175. Vinodgopal K., Kamat P. V. (1994), "Photochemistry of textile azo dyes. Spectral characterization of excited state, reduced and oxidized forms of acid orange 7", *Journal of Photochemistry and Photobiology A: Chemistry*, 83(2), pp. 141-146.

176. Visan A., Rafieian D., Ogieglo W., Lammertink R. G. (2014), "Modeling intrinsic kinetics in immobilized photocatalytic microreactors", *Applied catalysis B: environmental*, 150, pp. 93-100.

177. Wang C., Yin L., Xu Z., Niu J., Hou L.-A. (2017), "Electrochemical degradation of enrofloxacin by lead dioxide anode: Kinetics, mechanism and toxicity evaluation", *Chemical Engineering Journal*, 326, pp. 911-920.

178. Wang J., Guan Z., Huang J., Li Q., Yang J. (2014), "Enhanced photocatalytic mechanism for the hybrid g-C_3N_4/MoS_2 nanocomposite", *Journal of Materials Chemistry A*, 2(21), pp. 7960-7966.

179. Wang X., Lim T.-T. (2010), "Solvothermal synthesis of C–N codoped TiO_2 and photocatalytic evaluation for bisphenol A degradation using a visible-light irradiated LED photoreactor", *Applied Catalysis B: Environmental*, 100(1-2), pp. 355-364.

180. Wang X., Lim T.-T. (2011), "Effect of hexamethylenetetramine on the visible-light photocatalytic activity of C–N codoped TiO_2 for bisphenol A degradation: evaluation of photocatalytic mechanism and solution toxicity", *Applied Catalysis A: General*, 399(1-2), pp. 233-241.

181. Wang Y., Wang Q., Zhan X., Wang F., Safdar M., He J. (2013), "Visible light driven type II heterostructures and their enhanced photocatalysis properties: a review", *Nanoscale*, 5(18), pp. 8326-8339.

182. Wang Z.-P., Xu J., Cai W.-M., Zhou B.-X., He Z.-G., Cai C.-G., Hong X.-T. (2005), "Visible light induced photodegradation of organic pollutants on nitrogen and fluorine co-doped TiO_2 photocatalyst", *Journal of Environmental Sciences*, 17(1), pp. 76-80.

183. Watarai H., Funaki F. (1996), "Total internal reflection fluorescence measurements of protonation equilibria of rhodamine B and octadecylrhodamine B at a toluene/water interface", *Langmuir*, 12(26), pp. 6717-6720.

184. Wei L., Chen Y., Lin Y., Wu H., Yuan R., Li Z. (2014), "MoS_2 as non-noble-metal co-catalyst for photocatalytic hydrogen evolution over hexagonal $ZnIn_2S_4$ under visible light irradiations", *Applied Catalysis B: Environmental*, 144, pp. 521-527.

185. Wei Z., Li Y., Luo S., Liu C., Meng D., Ding M., Zeng G. (2014), "Hierarchical heterostructure of CdS nanoparticles sensitized electrospun TiO_2 nanofibers with enhanced photocatalytic activity", *Separation and Purification Technology*, 122, pp. 60-66.

186. Weimin X., Geissen S.-U. (2001), "Separation of titanium dioxide from photocatalytically treated water by cross-flow microfiltration", *Water Research*, 35(5), pp. 1256-1262.

187. Wen J., Xie J., Chen X., Li X. (2017), "A review on g-C_3N_4-based photocatalysts", *Applied surface science*, 391, pp. 72-123.

188. Wen X.-J., Niu C.-G., Zhang L., Liang C., Zeng G.-M. (2018), "A novel Ag_2O/CeO_2 heterojunction photocatalysts for photocatalytic degradation of enrofloxacin: possible degradation pathways, mineralization activity and an in depth mechanism insight", *Applied Catalysis B: Environmental*, 221, pp. 701-714.

189. Wu M.-H., Li L., Liu N., Wang D.-J., Xue Y.-C., Tang L. (2018), "Molybdenum disulfide (MoS_2) as a co-catalyst for photocatalytic degradation of organic contaminants: A review", *Process Safety and Environmental Protection*, 118, pp. 40-58.

190. Wu Y., Liu Z., Li Y., Chen J., Zhu X., Na P. (2019), "WS_2 nanodots-modified TiO_2 nanotubes to enhance visible-light photocatalytic activity", *Materials Letters*, 240, pp. 47-50.

191. Wu Y., Xu F., Guo D., Gao Z., Wu D., Jiang K. (2013), "Synthesis of ZnO/CdSe hierarchical heterostructure with improved visible photocatalytic efficiency", *Applied surface science*, 274, pp. 39-44.

192. Xia J., Ge Y., Zhao D., Di J., Ji M., Yin S., Li H., Chen R. (2015), "Microwave-assisted synthesis of few-layered MoS_2/BiOBr hollow microspheres with superior visible-light-response photocatalytic activity for ciprofloxacin removal", *CrystEngComm*, 17(19), pp. 3645-3651.

193. Xu D., Cheng B., Cao S., Yu J. (2015), "Enhanced photocatalytic activity and stability of Z-scheme Ag_2CrO_4-GO composite photocatalysts for organic pollutant degradation", *Applied Catalysis B: Environmental*, 164, pp. 380-388.

194. Xu F., Almeida T. P., Chang H., Xia Y., Wears M. L., Zhu Y. (2013), "Multi-walled carbon/IF-WS_2 nanoparticles with improved thermal properties", *Nanoscale*, 5(21), pp. 10504-10510.

195. Xu H.-Y., Wu L.-C., Zhao H., Jin L.-G., Qi S.-Y. (2015), "Synergic effect between adsorption and photocatalysis of metal-free g-C_3N_4 derived from different precursors", *PLoS One*, 10(11), p. e0142616.

196. Yan S., Li Z., Zou Z. (2009), "Photodegradation performance of g-C_3N_4 fabricated by directly heating melamine", *Langmuir*, 25(17), pp. 10397-10401.

197. Yan S., Li Z., Zou Z. (2010), "Photodegradation of rhodamine B and methyl orange over boron-doped g-C_3N_4 under visible light irradiation", *Langmuir*, 26(6), pp. 3894-3901.

198. Yang D., Sandoval S. J., Divigalpitiya W., Irwin J., Frindt R. (1991), "Structure of single-molecular-layer MoS_2", *Physical Review B*, 43(14), p. 12053.

199. Yang G. C., Chan S.-W. (2009), "Photocatalytic reduction of chromium (VI) in aqueous solution using dye-sensitized nanoscale ZnO under visible light irradiation", *Journal of Nanoparticle Research*, 11(1), p. 221.
200. Yang W., Shang J., Wang J., Shen X., Cao B., Peimyoo N., Zou C., Chen Y., Wang Y., Cong C. (2016), "Electrically tunable valley-light emitting diode (vLED) based on CVD-grown monolayer WS_2", *Nano letters*, 16(3), pp. 1560-1567.
201. Yatmaz H., Wallis C., Howarth C. (2001), "The spinning disc reactor–studies on a novel TiO_2 photocatalytic reactor", *Chemosphere*, 42(4), pp. 397-403.
202. Yavuz Y., Skogås J. G., Güllüoglu M. G., Langø T., Mårvik R. (2006), "Are cold light sources really cold?", *Surgical Laparoscopy Endoscopy & Percutaneous Techniques*, 16(5), pp. 370-376.
203. Yu J., Wang S., Low J., Xiao W. (2013), "Enhanced photocatalytic performance of direct Z-scheme g-C_3N_4/TiO_2 photocatalysts for the decomposition of formaldehyde in air", *Physical Chemistry Chemical Physics*, 15(39), pp. 16883-16890.
204. Yu W., Xu D., Peng T. (2015), "Enhanced photocatalytic activity of g-C_3N_4 for selective CO_2 reduction to CH_3OH via facile coupling of ZnO: a direct Z-scheme mechanism", *Journal of Materials Chemistry A*, 3(39), pp. 19936-19947.
205. Yu Y., Yan L., Cheng J., Jing C. (2017), "Mechanistic insights into TiO_2 thickness in Fe_3O_4@TiO_2-GO composites for enrofloxacin photodegradation", *Chemical Engineering Journal*, 325, pp. 647-654.
206. Zeng H., Liu G.-B., Dai J., Yan Y., Zhu B., He R., Xie L., Xu S., Chen X., Yao W. (2013), "Optical signature of symmetry variations and spin-

valley coupling in atomically thin tungsten dichalcogenides", *Scientific reports*, 3, p. 1608.

207. Zhang G., Huang C., Wang X. (2015), "Dispersing molecular cobalt in graphitic carbon nitride frameworks for photocatalytic water oxidation", *Small*, 11(9-10), pp. 1215-1221.

208. Zhang L., Zhang F., Yang X., Long G., Wu Y., Zhang T., Leng K., Huang Y., Ma Y., Yu A. (2013), "Porous 3D graphene-based bulk materials with exceptional high surface area and excellent conductivity for supercapacitors", *Scientific reports*, 3, p. 1408.

209. Zhang S., Zhang S., Song L. (2014), "Super-high activity of Bi^{3+} doped Ag_3PO_4 and enhanced photocatalytic mechanism", *Applied Catalysis B: Environmental*, 152, pp. 129-139.

210. Zhang W., Xiao X., Zheng L., Wan C. (2015), "Fabrication of TiO_2/MoS_2 composite photocatalyst and its photocatalytic mechanism for degradation of methyl orange under visible light", *The Canadian Journal of Chemical Engineering*, 93(9), pp. 1594-1602.

211. Zhang X., Lai Z., Tan C., Zhang H. (2016), "Solution-processed two-dimensional MoS_2 nanosheets: preparation, hybridization, and applications", *Angewandte Chemie International Edition*, 55(31), pp. 8816-8838.

212. Zhang Y., Pan Q., Chai G., Liang M., Dong G., Zhang Q., Qiu J. (2013), "Synthesis and luminescence mechanism of multicolor-emitting g-C_3N_4 nanopowders by low temperature thermal condensation of melamine", *Scientific reports*, 3, p. 1943.

213. Zhao W., Li J., Bo Wei Z., Wang S., He H., Sun C., Yang S. (2015), "Fabrication of a ternary plasmonic photocatalyst of $Ag/AgVO_3/RGO$

and its excellent visible-light photocatalytic activity", *Applied Catalysis B: Environmental*, 179, pp. 9-20.

214. Zhao X., Ma X., Sun J., Li D., Yang X. (2016), "Enhanced catalytic activities of surfactant-assisted exfoliated WS_2 nanodots for hydrogen evolution", *ACS nano*, 10(2), pp. 2159-2166.

215. Zhao Y., Zhang X., Wang C., Zhao Y., Zhou H., Li J., Jin H. (2017), "The synthesis of hierarchical nanostructured MoS_2/Graphene composites with enhanced visible-light photo-degradation property", *Applied Surface Science*, 412, pp. 207-213.

216. Zheng L.-L., Xiao X.-Y., Li Y., Zhang W.-P. (2017), "Enhanced photocatalytic activity of TiO_2 nanoparticles using WS_2/g-C_3N_4 hybrid as co-catalyst", *Transactions of Nonferrous Metals Society of China*, 27(5), pp. 1117-1126.

217. Zhou B., Zhao X., Liu H., Qu J., Huang C. (2010), "Visible-light sensitive cobalt-doped $BiVO_4$ (Co-$BiVO_4$) photocatalytic composites for the degradation of methylene blue dye in dilute aqueous solutions", *Applied Catalysis B: Environmental*, 99(1-2), pp. 214-221.

218. Zhou W., Yin Z., Du Y., Huang X., Zeng Z., Fan Z., Liu H., Wang J., Zhang H. (2013), "Synthesis of few-layer MoS_2 nanosheet-coated TiO_2 nanobelt heterostructures for enhanced photocatalytic activities", *small*, 9(1), pp. 140-147.

219. Zhu B., Xia P., Ho W., Yu J. (2015), "Isoelectric point and adsorption activity of porous g-C_3N_4", *Applied Surface Science*, 344, pp. 188-195.

220. Zou X., Zhang J., Zhao X., Zhang Z. (2020), "MoS_2/rGO composites for photocatalytic degradation of ranitidine and elimination of NDMA formation potential under visible light", *Chemical Engineering Journal*, 383, p. 123084.

APPENDIXES

Appendix 1: Prepared-material images

a) g-C_3N_4, WS_2, 5WCN, 7WCN, 10WCN

g-C_3N_4

WS_2

5WCN

7WCN

10WCN

b) g-C_3N_4, MoS_2, MCN1, MCN2, MCN3, MCN5

g-C_3N_4

MoS_2

MCN1

MCN2

MCN3

MCN5

Appendix 2: LC-MS of ENR solution after 0h, 4h and 8h of illumination

a) 0 h

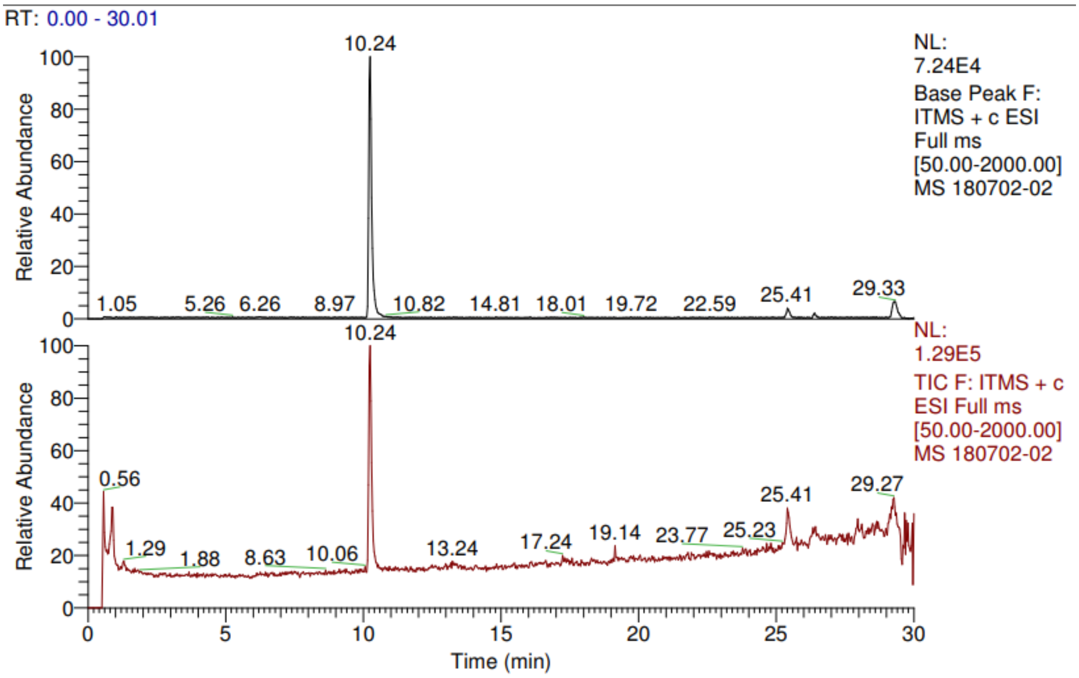

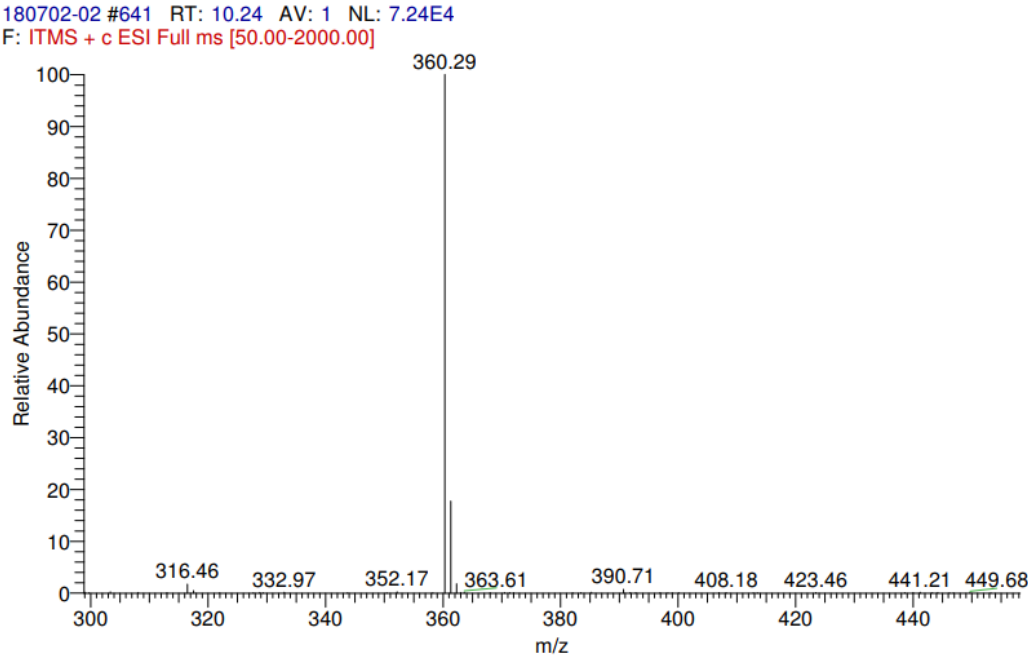

b) 4 h

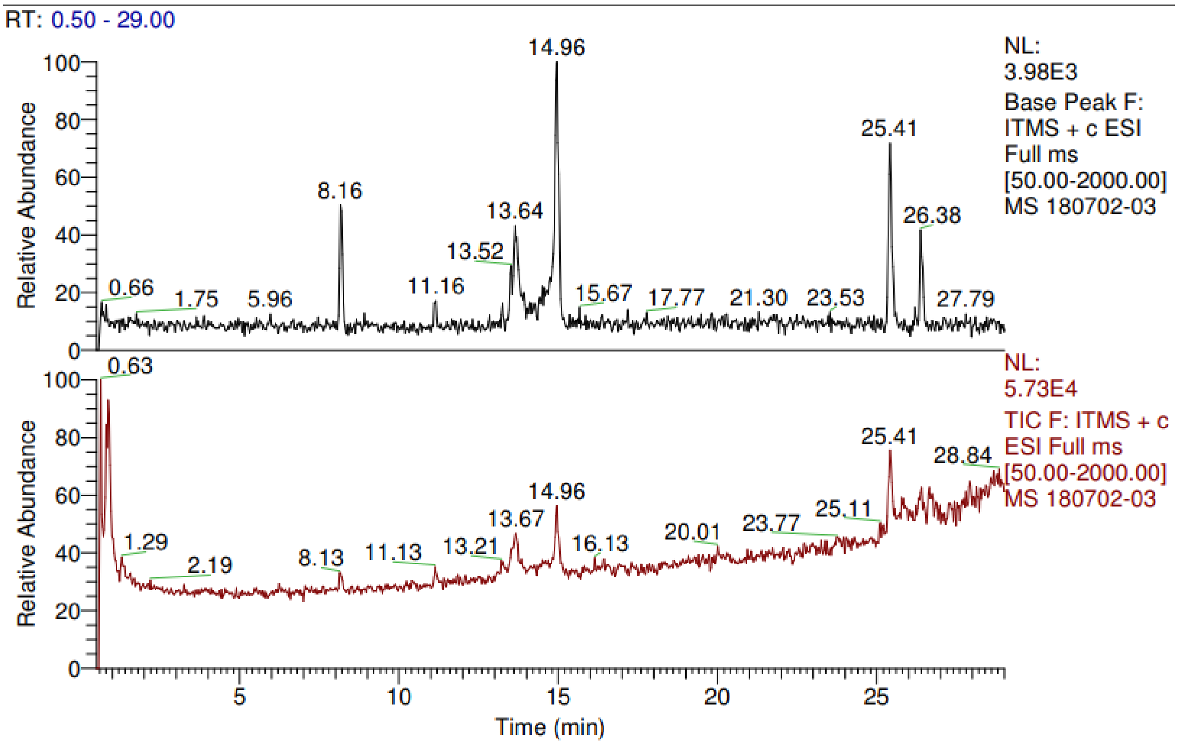
RT: 0.50 - 29.00
Relative Abundance
100
80
60
40
20
0
14.96
8.16
13.64
13.52
0.66
1.75
5.96
11.16
15.67
17.77
21.30
23.53
25.41
26.38
27.79
NL:
3.98E3
Base Peak F:
ITMS + c ESI
Full ms
[50.00-2000.00]
MS 180702-03
0.63
1.29
2.19
8.13
11.13
13.21
13.67
14.96
16.13
20.01
23.77
25.11
25.41
28.84
NL:
5.73E4
TIC F: ITMS + c
ESI Full ms
[50.00-2000.00]
MS 180702-03
5
10
15
20
25
Time (min)

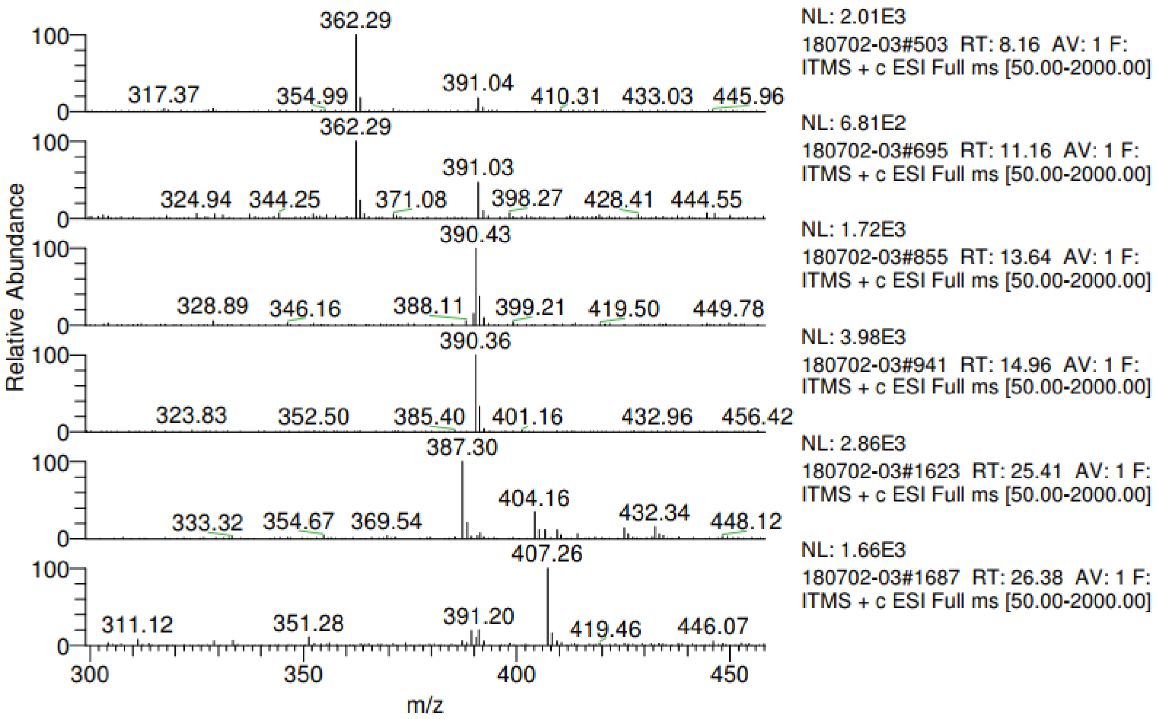
Relative Abundance
100
0
362.29
317.37
354.99
391.04
410.31
433.03
445.96
NL: 2.01E3
180702-03#503 RT: 8.16 AV: 1 F:
ITMS + c ESI Full ms [50.00-2000.00]
362.29
324.94
344.25
371.08
391.03
398.27
428.41
444.55
NL: 6.81E2
180702-03#695 RT: 11.16 AV: 1 F:
ITMS + c ESI Full ms [50.00-2000.00]
390.43
328.89
346.16
388.11
399.21
419.50
449.78
NL: 1.72E3
180702-03#855 RT: 13.64 AV: 1 F:
ITMS + c ESI Full ms [50.00-2000.00]
390.36
323.83
352.50
385.40
401.16
432.96
456.42
NL: 3.98E3
180702-03#941 RT: 14.96 AV: 1 F:
ITMS + c ESI Full ms [50.00-2000.00]
387.30
333.32
354.67
369.54
404.16
432.34
448.12
NL: 2.86E3
180702-03#1623 RT: 25.41 AV: 1 F:
ITMS + c ESI Full ms [50.00-2000.00]
407.26
311.12
351.28
391.20
419.46
446.07
NL: 1.66E3
180702-03#1687 RT: 26.38 AV: 1 F:
ITMS + c ESI Full ms [50.00-2000.00]
300
350
400
450
m/z

c) 8 h

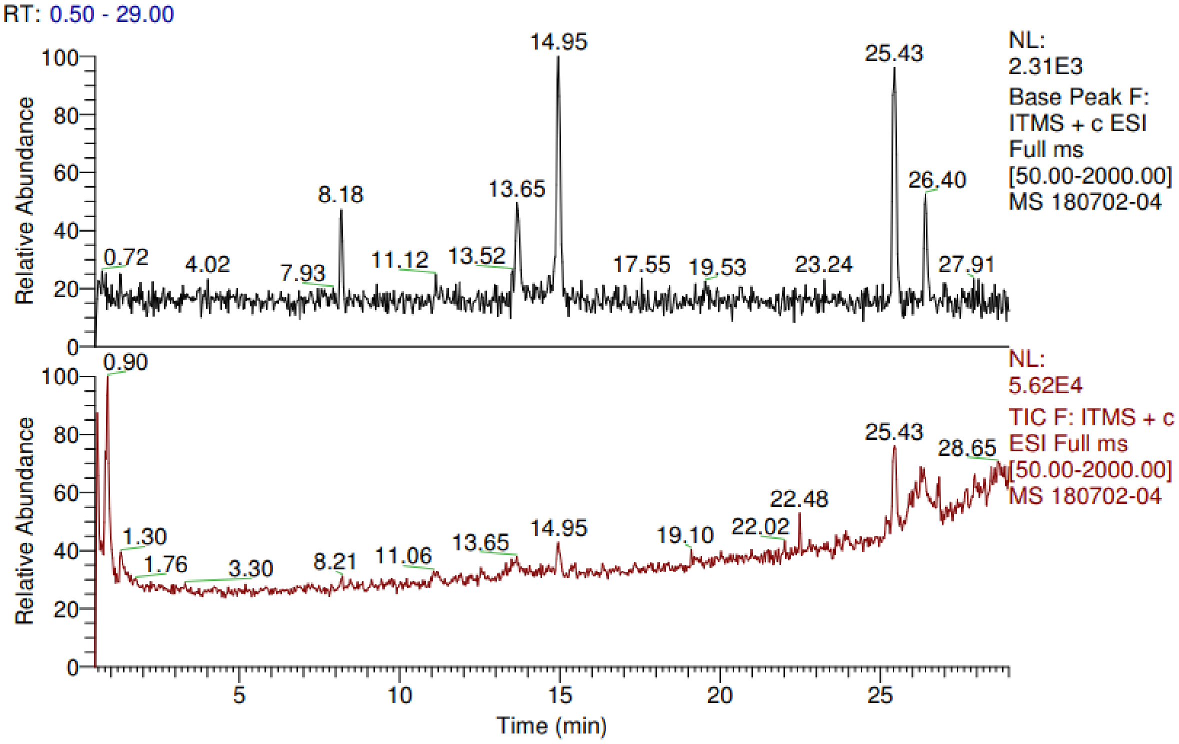
RT: 0.50 - 29.00
Relative Abundance
100
80
60
40
20
0
14.95
25.43
8.18
13.65
26.40
0.72
4.02
7.93
11.12
13.52
17.55
19.53
23.24
27.91
NL:
2.31E3
Base Peak F:
ITMS + c ESI
Full ms
[50.00-2000.00]
MS 180702-04
0.90
1.30
1.76
3.30
8.21
11.06
13.65
14.95
19.10
22.02
22.48
25.43
28.65
NL:
5.62E4
TIC F: ITMS + c
ESI Full ms
[50.00-2000.00]
MS 180702-04
5
10
15
20
25
Time (min)

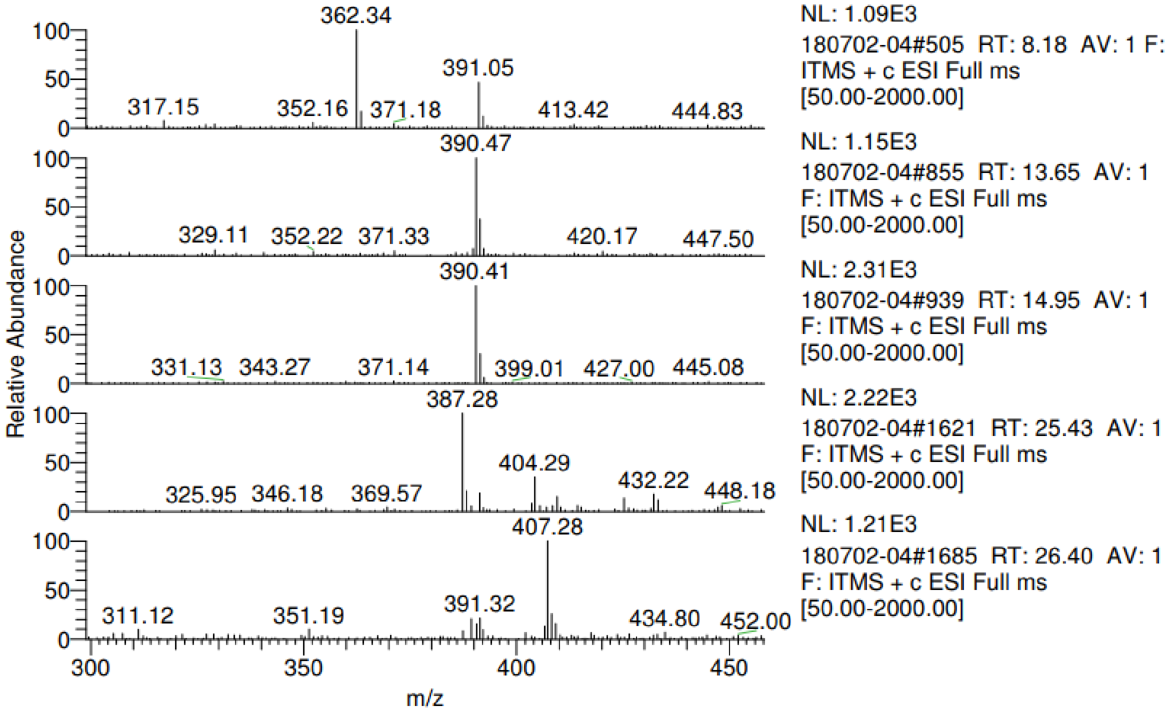
Relative Abundance
100
50
0
362.34
391.05
317.15
352.16
371.18
413.42
444.83
NL: 1.09E3
180702-04#505 RT: 8.18 AV: 1 F: ITMS + c ESI Full ms [50.00-2000.00]
390.47
329.11
352.22
371.33
420.17
447.50
NL: 1.15E3
180702-04#855 RT: 13.65 AV: 1 F: ITMS + c ESI Full ms [50.00-2000.00]
390.41
331.13
343.27
371.14
399.01
427.00
445.08
NL: 2.31E3
180702-04#939 RT: 14.95 AV: 1 F: ITMS + c ESI Full ms [50.00-2000.00]
387.28
404.29
325.95
346.18
369.57
432.22
448.18
NL: 2.22E3
180702-04#1621 RT: 25.43 AV: 1 F: ITMS + c ESI Full ms [50.00-2000.00]
407.28
311.12
351.19
391.32
434.80
452.00
NL: 1.21E3
180702-04#1685 RT: 26.40 AV: 1 F: ITMS + c ESI Full ms [50.00-2000.00]
300
350
400
450
m/z